

POLITECNICO DI TORINO

Master's Degree in Biomedical Engineering



Master's Degree Thesis

**Algorithmic Optimization and Validation
of a Multi-Sensor Wearable System for
Exploring Gait Under Extreme Terrain
Conditions**

Supervisors

Prof. Andrea CEREATTI

Dott. Diego TORRICELLI

Dott.ssa Francesca SALIS

Dott.ssa Adriana TORRES

Candidate

Geronimo Federico RATTO

Academic Year 2022/2023

Summary

Through the examination of human gait in challenging environments, valuable knowledge can be acquired regarding the biomechanics of walking on unstable surfaces. This understanding is crucial for advancing the development of resilient and steady robotic systems. Human gait serves as a benchmark for performance and a significant source of inspiration for legged machines, improving the stability and functionality of robotic technology.

Wearable systems offer distinct advantages over traditional laboratory-based setups when studying human gait in challenging conditions. They enable data collection in real-world environments that closely resemble the conditions encountered by legged robots. This study aims to validate the use of the INDIP system, a wearable multi-sensor system comprising inertial modules, pressure insoles, and distance sensors, for accurately characterizing gait in diverse and unstructured terrains. In this work, a comprehensive study was conducted to extract spatio-temporal parameters and events from human gait on irregular surfaces. The INDIP algorithm was improved to ensure its robustness across various types of terrains. The obtained results were validated using a stereophotogrammetry system called Vicon, known for its accuracy in gait analysis. The validation of the INDIP system in regular terrains for both healthy and pathological subjects has already been established. However, this research takes a significant step forward by validating its effectiveness in analyzing human gait within challenging terrains.

Through the optimization of the algorithm, remarkable improvements have been achieved. The maximum time difference in event identification between the INDIP system and a Stereophotogrammetry system has been reduced to less than 0.1 seconds for different terrains. Additionally, the maximum mean error for stride length achieved is approximately 4%, for stride time it is around 1%, for cadence it is 1.3%, and for walking speed it is 3%. These advancements highlight the enhanced accuracy and reliability of the INDIP system in capturing and analyzing gait parameters in demanding terrains. The findings can aid in improving the stability and performance of legged robotic systems by incorporating insights gained from the biomechanics of human gait.

Acknowledgements

I would like to express my heartfelt gratitude to the individuals and institutions who have played a pivotal role in my journey. First and foremost, I am deeply grateful to Politecnico di Torino and Universidad Nacional de Córdoba for providing me with the academic platform and resources to pursue my studies and research.

I am deeply grateful to express my heartfelt appreciation to Andrea Cereatti and his group, specially Francesca and Stefano, for their immeasurable patience and invaluable feedback. Without their unwavering support, I would not have been able to undertake this transformative journey. I am also indebted to Diego Torricelli, whose generosity provided me with a nurturing environment where I could comfortably pursue my studies and acquire invaluable knowledge. Furthermore, I extend my sincere thanks to the remarkable Neuro Rehabilitation Group, whose generous support made this endeavor possible. In particular, I would like to acknowledge Adriana, Marina, and Pietro for their patience and imparted wisdom.

I am sincerely grateful for the unwavering support and assistance of my classmates from Argentina and Italy. I would like to extend a special mention to my dear friends from "mensa chica" who accompanied me throughout this experience. Additionally, I express my gratitude to my friends Alice, Chiara, and Beatrice, who made me feel as home in Italy. I cannot overlook the unwavering support of my friends from Argentina, Camila, Emilia, and Agustina, who consistently cheered me on and encouraged me to embark on this journey.

Finally, I would be remiss if I didn't acknowledge my family, especially my parents, Silvana and Federico. Their unwavering belief in me has served as a constant source of motivation and kept my spirits high throughout this entire process.

Table of Contents

List of Tables	VI
List of Figures	VII
Acronyms	XI
1 Introduction	1
1.1 Relevance	1
1.2 Project Outline	3
2 State of the Art	5
2.1 Human gait as a gold standard for robotic locomotion	5
2.2 Gait Analysis on uneven terrain	6
3 Theoretical Framework	8
3.1 Introduction to Gait Analysis	8
3.1.1 Anatomic Considerations	8
3.1.2 Gait Phases and Events	9
3.2 Gait global Characterization	11
3.2.1 Temporal Parameters	12
3.2.2 Spatial Parameters	12
3.2.3 Velocity Parameters	12
3.3 Gait Analysis Instrumentation Systems	13
3.3.1 Optoelectronic stereophotogrammetry	13
3.3.2 Multi-sensor wearable systems	14
3.3.3 Magneto-Inertial Measurement Units	16
3.3.4 Pressure Insoles	21
3.3.5 Distance Sensors	22
4 Materials	24
4.1 VICON System	24

4.1.1	Hardware Components	24
4.1.2	Camera Calibration Process	26
4.1.3	Software	27
4.2	INDIP System	27
4.3	Data Collection	28
4.4	Subject Selection	28
4.5	Experimental Protocol	29
4.5.1	Systems Calibration	32
4.6	Instrumentation	35
4.7	Experimental Set Up	37
4.8	Data Preprocessing	38
4.8.1	Vicon Data Preprocessing and Organization.	38
4.8.2	INDIP Data Preprocessing and Organization	39
5	Methods	41
5.1	Vicon Data Processing	41
5.2	INDIP Data Processing and Algorithm Optimization	42
5.2.1	Automatization of Personalization Phase	45
5.2.2	PI signal quality enhancement for improving event identifica- tion.	47
5.2.3	Rising and Falling edge new criteria	53
5.2.4	IC and FC selection refinement	56
5.3	Equally weighted PI and IMU event identification contribution . . .	60
5.4	Data analysis	63
5.4.1	Event Identification Analysis	63
5.4.2	Spatio-temporal Parameters Analysis	63
6	Results	67
6.1	Event identification analysis	67
6.1.1	Original vs Modified Algorithm comparison	67
6.2	Spatio-temporal Parameters Analysis	74
7	Discussion	87
7.1	Event Identification Analysis	88
7.1.1	Plane Terrain at 0°	88
7.1.2	Plane Terrain at 15°	89
7.1.3	Mat Terrain at 0°	89
7.1.4	Mat Terrain at 15°	89
7.1.5	Unstructured Terrain at 0°	89
7.1.6	Unstructured Terrain at 15°	90
7.1.7	Upward Sawtooth at 0°	90

7.1.8	Upward Sawtooth at 15°	91
7.1.9	Downward Sawtooth at 0°	91
7.1.10	Downward Sawtooth at 15°	91
7.2	Spatio-temporal Parameters Analysis	92
8	Conclusions	96
	Bibliography	98

List of Tables

4.1	Summary of participants for trials acquisitions.	28
4.2	Terrain conditions name and numbers.	31
4.3	Experiments description sheet.	33
6.1	Time differences for Plane Terrain at 0° between the original and modified code.	69
6.2	Time differences for the overground terrain at 15° between the original and modified code.	71
6.3	Time differences for the Mat terrain at 0° between the original and modified code.	73
6.4	Time differences for the Mat at 15° between the original and modified code.	75
6.5	Time differences for the unstructured terrain at 0° between the original and modified code.	76
6.6	Time differences for the unstructured terrain at 15° between the original and modified code.	77
6.7	Time differences for the Upward sawtooth terrain at 0° between the original and modified code.	78
6.8	Time differences for the Upward sawtooth terrain at 15° between the original and modified code.	79
6.9	Time differences for the Downward sawtooth terrain at 0° between the original and modified code.	81
6.10	Time differences for the Downward Sawtooth terrain at 15° between the original and modified code.	82
6.11	Spatio-temporal parameters values obtained with the final algorithm modification.	84

List of Figures

1.1	Robotic applications in uneven terrains.	2
3.1	Illustration of the Stance Phase.	10
3.2	Schematic diagram of the spatial sequence of the gait cycle [27]. . .	11
3.3	Spatial parameters representation.	12
3.4	Optical motion capture procersss flowchart.	15
3.5	Model of an Accelerometer [35].	18
3.6	Model of a rotating disk for gyroscope explanation [36].	19
3.7	Simple depiction of a proof mass vibrating system [36].	19
3.8	Schematic architecture of a single proof mass vibrating gyroscope [36].	20
3.9	Pressure insoles from INDIP System.	22
4.1	Active Wand.	25
4.2	Truss System for Vicon Cameras.	25
4.3	Vicon Cameras Positioning in Nexus Software.	26
4.4	Vicon Passive Markers.	26
4.5	INDIP System with PI, IMUs and DS.	27
4.6	Base platform for experiments.	30
4.7	Graphical representation of each terrain condition.	31
4.8	I) Mat terrain, II) Downward Sawtooth Terrain, III) Unstructured Terrain, VI) Upward Sawtooth Terrain, V) Plane Terrain.	32
4.9	Signals for the Standing acquisition for the right foot of subject 3. A) Accelerometer readings; B) Gyroscope readings; C) Magnetometer readings.	35
4.10	Signals for the Personalization acquisition for the right foot of subject 3. A) Accelerometer readings; B) Gyroscope readings; C) Magne- tometer readings.	36
4.11	Representation of the subject instrumentation, vicon markers are red painted.	37
4.12	Experimental subject instrumentation.	37
4.13	Experimental setup.	38

4.14	Data organization.	38
4.15	A) Input data organization for the INDIP algorithm, B) Output data organization from the INDIP algorithm.	39
5.1	Vicon Processing Pipeline.	42
5.2	Flow Chart related to the manually event identification in Vicon.	43
5.3	Marker trajectory in Nexus Software.	43
5.4	Nexus visualization of the reconstructed pose and terrain.	44
5.5	Left and Right Foot Antero-Posterior Trajectory from Vicon with IC identified.	45
5.6	Stance, Fly and Personalisation problem identification.	46
5.7	Problem of using a constant treshold for defining Stance Phase.	47
5.8	PI signal in normal walking condition.	48
5.9	PI signal in extreme terrain walking condition.	49
5.10	Correlation Heatmap between sensors.	51
5.11	False positive sensors and true positive sensors classification.	52
5.12	Mean FPAS Signal.	53
5.13	False positive active sensors after mean multiplication.	53
5.14	Applied sigmoid function with $\phi = 0.05$	54
5.15	PI signals after sigmoid application.	54
5.16	FC Candidates with the Original algorithm.	56
5.17	FC Candidates with the new criteria.	57
5.18	IC and FC found by each pressure sensor.	58
5.19	IC and FC candidates found with the original algorithm.	59
5.20	IC and FC candidates after applying the high density criteria.	60
5.21	Original Algorithm Flowchart for merging PI and IMUs event information.	61
5.22	Modified Algorithm Flowchart for merging PI and IMUs event information.	61
5.23	Heatmap showcasing the MAE between events detected using the INDIP's PI and events identified through the SP system.	62
5.24	Heatmap showcasing the MAE between events detected using the INDIP's IMUs and events identified through the SP system.	62
6.1	Bland Altman event differences for Plane Terrain at 0° with the A) Original Code and B) Modified Code.	68
6.2	Bland Altman IC differences for Plane Terrain at 0° with the A) Original Code and B) Modified Code.	68
6.3	Bland Altman FC differences for Plane Terrain at 0° with the A) Original Code and B) Modified Code.	69

6.4	Bland Altman event differences for Plane Terrain at 15° with the A) Original Code and B) Modified Code.	70
6.5	Bland Altman IC differences for Plane Terrain at 15° with the A) Original Code and B) Modified Code.	70
6.6	Bland Altman FC differences for Plane Terrain at 15° with the A) Original Code and B) Modified Code.	71
6.7	Bland Altman event differences for Mat Terrain at 0° with the A) Original Code and B) Modified Code.	72
6.8	Bland Altman IC differences for Mat Terrain at 0° with the A) Original Code and B) Modified Code.	72
6.9	Bland Altman FC differences for Mat Terrain at 0° with the A) Original Code and B) Modified Code.	73
6.10	Bland Altman event differences for Mat Terrain at 15° with the A) Original Code and B) Modified Code.	74
6.11	Bland Altman IC differences for Mat Terrain at 15° with the A) Original Code and B) Modified Code.	74
6.12	Bland Altman FC differences for Mat Terrain at 15° with the A) Original Code and B) Modified Code.	75
6.13	Bland Altman event differences for Unstructured Terrain at 0° with the A) Original Code and B) Modified Code.	75
6.14	Bland Altman IC differences for Unstructured Terrain at 0° with the A) Original Code and B) Modified Code.	76
6.15	Bland Altman FC differences for Unstructured Terrain at 0° with the A) Original Code and B) Modified Code.	76
6.16	Bland Altman event differences for Unstructured Terrain at 15° with the A) Original Code and B) Modified Code.	77
6.17	Bland Altman IC differences for Unstructured Terrain at 15° with the A) Original Code and B) Modified Code.	77
6.18	Bland Altman FC differences for Unstructured Terrain at 15° with the A) Original Code and B) Modified Code.	78
6.19	Bland Altman event differences for Upward Sawtooth Terrain at 0° with the A) Original Code and B) Modified Code.	78
6.20	Bland Altman IC differences for Upward Sawtooth Terrain at 0° with the A) Original Code and B) Modified Code.	79
6.21	Bland Altman FC differences for Upward Sawtooth Terrain at 0° with the A) Original Code and B) Modified Code.	79
6.22	Bland Altman event differences for Upward Sawtooth Terrain at 15° with the A) Original Code and B) Modified Code.	80
6.23	Bland Altman IC differences for Upward Sawtooth Terrain at 15° with the A) Original Code and B) Modified Code.	80

6.24	Bland Altman FC differences for Upward Sawtooth Terrain at 15° with the A) Original Code and B) Modified Code.	80
6.25	Bland Altman event differences for Downward Sawtooth Terrain at 0° with the A) Original Code and B) Modified Code.	81
6.26	Bland Altman IC differences for Downward Sawtooth Terrain at 0° with the A) Original Code and B) Modified Code.	81
6.27	Bland Altman FC differences for Downward Sawtooth Terrain at 0° with the A) Original Code and B) Modified Code.	82
6.28	Bland Altman event differences for Downward Sawtooth Terrain at 15° with the A) Original Code and B) Modified Code.	82
6.29	Bland Altman IC differences for Downward Sawtooth Terrain at 15° with the A) Original Code and B) Modified Code.	83
6.30	Bland Altman FC differences for Downward Sawtooth Terrain at 15° with the A) Original Code and B) Modified Code.	83
6.31	Barplot for comparing mean and standard deviation values for SL obtained with both systems.	85
6.32	Barplot for comparing mean and standard deviation values for ST obtained with both systems.	85
6.33	Barplot for comparing mean and standard deviation values for WS obtained with both systems.	86
6.34	Barplot for comparing mean and standard deviation values for Cadence obtained with both systems.	86

Acronyms

SP

Stereophotogrammetry System

IR

Inferred

MEMS

Microelectromechanical Systems

MIMU

Magneto-Inertial Measurement Unit

PD

Parkinson's' Disease

INDIP

Inertial module with Distance sensors and Pressure insoles

IC

Initial Contact

FC

Final Contact

HS

Heel Strike

FO

Foot Off

MOCAP

Motion Capture

ME

Mean Error

MAE

Mean Absolute Error

RMSE

Root Mean Squared Error

ICC

Intraclass Correlation

DoP

Direction of Progression

ECS

Earth Coordinate System

LCS

Local Coordinate System

GCS

Global Coordinate System

DRI

Direct Reverse Integration

STPs

Gait spatiotemporal parameters

Chapter 1

Introduction

1.1 Relevance

Over the years, significant progress has been made within the robotics community to augment the potential of robots, catering to the ever-expanding demands of emerging application domains. This relentless pursuit has culminated in the seamless integration of robots into shared spaces alongside human counterparts, breaking down the barriers that once confined their presence to controlled environments. Previously inaccessible environments, including bustling public areas, collaborative industrial settings, and residential spaces, are now accessible to robots.

To ensure optimal performance in these dynamic contexts, the latest generation of collaborative robots must showcase their remarkable interaction capabilities with both humans and the surrounding environment. Achieving high levels of reliability, safety, and adaptability in such conditions has intensified the need for comprehensive performance evaluation across multiple sectors of the robotics field.

Ultimately, the domain of locomotion has witnessed groundbreaking developments, marked by the advent of highly sophisticated legged robots boasting exceptional biomimetic abilities. Drawing inspiration from nature's own mechanisms, these robots have demonstrated remarkable proficiency in navigating through unstructured and challenging natural environments. Their agile and versatile nature opens up new horizons for applications such as search and rescue missions, exploration of hazardous terrains, and diverse industrial tasks.

Legged robotic movement in uneven and extreme terrains is a field of research and development that focuses on designing and developing robots capable of traversing challenging landscapes. Unlike wheeled or tracked robots, legged robots possess the ability to adapt to various terrains by mimicking the locomotion of humans. This adaptability enables them to navigate through environments where conventional vehicles or machines face significant limitations. Figure 1.1 illustrates various

instances of robotic applications in demanding environments, where robots play different roles, either assisting human locomotion or replacing it entirely.



Figure 1.1: Robotic applications in uneven terrains.

The primary motivation behind legged robotic systems is to extend the capabilities of robots beyond structured and predictable environments [1], such as smooth floors or flat surfaces. By employing legs, these robots can negotiate uneven terrain, including rocky surfaces, steep inclines, stairs, and even hazardous or disaster-stricken areas. The goal is to create robots that can efficiently and effectively navigate natural and human-made environments [2], mimicking the agility and versatility of living organisms.

Researchers and engineers in the field of legged robotics face numerous challenges. One of the key challenges is developing robust and dynamic control algorithms that enable stable locomotion on unpredictable and irregular terrain [3]. These algorithms must account for variations in ground height, slope, and surface conditions to ensure the robot maintains balance and stability during movement.

Sensors play a vital role in legged robotic systems as they provide real-time feedback for balance, navigation, and terrain analysis [4]. These sensors can include cameras, depth sensors, accelerometers, gyroscopes, and force sensors. By fusing data from these sensors, the robot can perceive its surroundings, adapt to changing terrain, and adjust its movements accordingly.

The applications of legged robotic systems in uneven and extreme terrains are diverse. They have potential uses in search and rescue operations, exploration of hazardous environments, military operations, agricultural tasks, and even assistance for people with mobility impairments [5]. By overcoming the limitations of traditional wheeled or tracked robots, legged robotic systems offer the potential to revolutionize how we interact with challenging terrains.

In summary, legged robotic movement in uneven and extreme terrains is a multidisciplinary field that combines robotics, control theory, mechanical design, and

sensor technology. Through the development of advanced algorithms, mechanical structures, and sensor integration, researchers strive to create legged robots capable of traversing complex and unpredictable landscapes, opening up new possibilities for a range of applications.

1.2 Project Outline

The primary objective of this project is to enhance and strengthen the durability of a multi-sensor wearable system called "INDIP" (INertial module with DIstance sensors and Pressure insoles) for characterizing gait under extreme terrain conditions. By analyzing and measuring human gait on uneven terrains, the project seeks to establish reliable gait characteristics that will serve for robotic purposes. The INDIP system, which incorporates inertial modules, distance sensors, and pressure insoles, has already been validated in previous studies [6] involving both healthy individuals and those with pathological conditions during various tasks. This system aims to automatically identify events in gait and extract spatiotemporal parameters accurately. Through further development and validation, the project aims to refine the INDIP system, making it a robust tool for assessing gait in extreme conditions.

The project involves comparing the spatio-temporal parameters, events, and their variability obtained using the original algorithm of the system with those obtained using a modified and more robust version. Various experiments were conducted to collect the necessary data for processing. The results of the updated algorithm are validated by comparing them with measurements obtained using the stereophotogrammetry system (SP), which is an optoelectronic motion capture system based on markers and IR cameras that allow to obtain subject movement and trajectories being used as a Gold Standard for gait parameters calculation.

In the current state of the art, the estimation of spatio-temporal parameters is not only performed in the human motion analysis laboratory by means of SP and force plates [7], but also there is plenty of investigations developing and validating tools and algorithms that facilitate gait analysis in uneven terrains [8]. Inertial measurement units (IMUs) are well-suited for quantifying gait due to their affordability and lightweight nature, allowing for prolonged data collection [9]. However, it is important to note that IMUs have their own set of limitations, which can impact their effectiveness in characterizing gait [10]. These limitations, will be further elaborated and discussed in detail in the relevant chapter of the project. Numerous studies [11] have demonstrated that multi-sensor wearable systems, such as the INDIP system, offer a reliable approach to characterizing gait, effectively addressing the limitations associated with standalone IMUs. These wearable systems combine multiple sensors, including IMUs, to enhance the accuracy

and robustness of gait analysis. By integrating data from various sensors, these systems mitigate the inherent issues of IMUs and provide a more comprehensive understanding of human gait dynamics. The INDIP system, in particular, has shown promising results in accurately assessing gait parameters, making it a valuable tool for advancing gait analysis research and applications [6].

As detailed in the state of the art of Chapter 2, there is a noticeable gap in the existing literature when it comes to studies utilizing multi-sensor systems (that includes IMUs), for automatically identifying gait events under extreme conditions. This research gap highlights the significance of the current thesis, which aims to fill this void and address this specific objective. By leveraging the capabilities of multi-sensor systems, the thesis seeks to develop a novel approach to automatically detect and identify gait events during extreme conditions. This contribution will not only advance the understanding of gait in challenging environments but also offer valuable insights for the development of robust and adaptable robotic systems.

The proposed thesis was conducted through three resumed steps to accomplish its objective:

1. Laboratory acquisitions were performed following an experimental protocol that incorporated various types of terrains. This step aimed to compare the outcomes of the INDIP system with those obtained from the SP system.
2. The performance of the original algorithm, which had been previously validated [6], was evaluated in comparison to the SP system.
3. An algorithm optimization process was undertaken to enhance its performance specifically in uneven terrain conditions. The optimized algorithm was then validated against the SP system.

Chapter 2

State of the Art

2.1 Human gait as a gold standard for robotic locomotion

Understanding and incorporating principles of human gait into robot motion is of utmost importance for efficient and stable locomotion in diverse terrains. By studying the biomechanics and motor control behind human walking, robots can achieve energy efficiency, balance, adaptability, and enhanced human-robot interaction. Replicating the stability and balance exhibited in human gait helps robots maintain equilibrium and adapt to uneven or challenging terrains, enhancing overall performance and preventing falls [12]. Furthermore, the adaptability of human gait allows robots to navigate various terrains with ease, enabling them to adjust foot placement and motion based on the characteristics of the terrain. Incorporating human-like walking patterns also improves human-robot interaction, as it enhances acceptance and facilitates intuitive communication between humans and robots. Lastly, human gait serves as an inspiration for biomimetic robot design, allowing engineers to develop robots with similar functionalities and capabilities [13]. Overall, understanding and incorporating human gait principles into robot motion is essential for creating efficient, stable, adaptable, and interactive robots capable of navigating complex terrains and performing a wide range of tasks effectively.

Human gait is characterized by periods of loading and unloading of the limbs to move around providing independence. It allows many of the activities of daily living, sports, facilitates many social activities, and it is required in many occupations. Gait analysis is supported by technologies and instrumentation for not only measuring body mechanics and movements but also muscle activity, allowing to study better the locomotion pattern. [14]. New technologies have provided tools and devices to obtain accurate and reliable measurements of the gait profile.

Humans are expected to move above different kind of outdoor environments during their whole life, they can walk on various environments with adapting to each situation. By studying these adaptive strategies, researchers can develop control algorithms and leg mechanisms that enable robots to adjust their movements and foot placement based on the characteristics of the terrain. This adaptability enhances the robot's ability to navigate complex environments and improves its overall performance [12].

For quantifying and characterizing gait, key metrics such as spatiotemporal parameters are well used. Gait parameters play a crucial role in improving robotic motion. These parameters, which encompass measurements of both space and time during the gait cycle, provide quantitative insights into the timing and spatial characteristics of human walking or running. By analyzing parameters such as step length, stride length, cadence, and stance duration, researchers can identify areas for improvement and optimize the robotic gait pattern [15]. This information helps in developing control algorithms and mechanical designs that enhance the efficiency, stability, and adaptability of legged robots, ultimately enabling them to navigate complex terrains with greater effectiveness.

2.2 Gait Analysis on uneven terrain

Human gait analysis in uneven terrains is a critical area of study that aims to understand how individuals adapt their walking patterns and maintain stability when traversing challenging and unpredictable surfaces. Researchers employ sophisticated motion capture systems, force plates, and wearable sensors to capture data on foot placement, step length, joint angles, and ground reaction forces during locomotion on uneven surfaces [16]. By analyzing this data, researchers gain valuable insights into the strategies employed by the human body to navigate such terrains, including changes in stride length, alterations in muscle activation patterns, and adjustments in center of mass trajectory.

Spatio-temporal parameters in gait are used for measurements and timing of various aspects of human walking or gait. These parameters are commonly used to characterize and analyze gait patterns. Evaluation of spatio-temporal parameters in gait encompasses various methods and technologies, including wearable and non-wearable systems. Wearable options consist of stereophotogrammetry systems, inertial-based systems, goniometers, and others. SP is considered the gold standard but has drawbacks, such as high cost, time-consuming patient preparation, and limited applicability in controlled laboratory conditions due to infrared sensitivity.

In recent years, microelectromechanical systems (MEMS) have emerged as significant and widely used tools, particularly IMUs. IMUs consist of miniaturized accelerometers and gyroscopes. They have gained popularity in gait analysis due

to their advantages, including low power consumption, affordability, lightweight design, lack of external power requirements, fast data management, portability, and self-contained data processing through embedded microprocessors. Sensorizing patients with IMUs is relatively straightforward, and they can be used both inside the laboratory and in external environments.

It is worth mentioning that IMUs alone do not offer direct data for a thorough analysis of gait, including spatio-temporal parameters and joint angles. Instead, IMUs provide an indirect measurement of temporal parameters and cannot be considered as a gold standard. Thus, it becomes necessary to utilize a multi-sensor system that can provide dependable and strong measurements, serving as a reliable reference even outside the controlled laboratory environment.

Within the existing literature on gait analysis in uneven terrains, a variety of systems have been employed to capture spatio-temporal parameters. These systems encompass treadmills [17, 18], commonly used stationary machines for gait studies, as well as stereophotogrammetry systems [19, 20, 21] and force plates [18]. In certain studies [22, 22], inertial-based wearable systems were combined with the aforementioned systems. As previously mentioned, the INDIP system was utilized in a study that validated the calculation of spatio-temporal parameters in overground terrains [6]. Additionally, a considerable number of automatic algorithms and methods in the literature have been proven and validated for characterizing gait in real-world scenarios, involving both healthy [23] and pathological subjects [24, 25]. However, there is a paucity of literature specifically focusing on the combined use of these systems within a comprehensive multi-sensor system to obtain spatio-temporal parameters in uneven and extreme terrains. Furthermore, no research has been found that addresses the presence of an automated algorithm ensuring high levels of accuracy, precision, and reliability in calculating these parameters across multiple terrain conditions.

In light of the aforementioned considerations, by combining data from inertial sensors, pressure insoles and distance sensors that the INDIP system use, exists the possibility to provide a comprehensive and reliable analysis of gait dynamics, enabling a more thorough understanding of human locomotion in uneven and extreme terrains for being applied to the field of robotics, specifically in the development of robotic systems capable of navigating challenging environments.

Chapter 3

Theoretical Framework

3.1 Introduction to Gait Analysis

The human ability of walking is achieved through the movement of the pelvic limbs in an alternating and rhythmic way allowing the movement of the body in anteroposterior direction and is divided into different steps. The human locomotion is possible because of the activation of the lower limb muscles in conjunction with sensory information of the neuronal network to allow joint movement and muscle contraction control [26]. The gait cycle is the functional unit of gait analysis and can be defined from the foot contact with the ground to the subsequent same ground contact of the same foot.

3.1.1 Anatomic Considerations

HIP

Throughout the walking cycle, the hip joint undergoes movement in three directions: Flexion-extension happens around a side-to-side axis, adduction-abduction occurs around a front-to-back axis, and internal-external rotation takes place around a forward-backward axis [27].

KNEE

When it comes to the knee, three types of angular rotation are also possible during walking. The main movement involves knee flexion-extension around a side-to-side axis. Knee internal-external rotation around a forward-backward axis and adduction-abduction around a front-to-back axis may also happen, although they are less consistent and have smaller amplitudes among individuals without any health issues [27].

ANKLE AND FOOT

The movement of the ankle is limited by the structural constraints of the talocrural joint, allowing only for plantarflexion (pointing the foot downward) and dorsiflexion (raising the foot upward). The foot has a dual role, functioning as a partially rigid structure, acting as a spring during weight transfer, and as a lever arm during push-off. It also provides necessary stability to support the body's weight [27].

UPPER BODY

When considering the pelvis and thorax, their movements are primarily passive and are a consequence of the lower body's motion rather than being actively and purposefully initiated. Additionally, the reciprocal arm swing during walking also helps constrain the angular momentum of the trunk [27].

3.1.2 Gait Phases and Events

A full gait cycle is defined by the occurrence of two sequential phases, these are:

1. **Stance Phase:** The stance phase constitutes 60% of the stride and consists of two periods of double limb support (initial and terminal), when the contralateral foot is in contact with the ground, and an intermediate period of single limb support, when the contralateral limb is engaged in the swing phase. It begins with the initial contact of the foot on the ground and represents the period of adjacency on the ground where it supports all or part of the body weight [27]. The stance phase can be divided into six events and periods:
 - (a) **Initial Contact (IC) or Heel Strike (HS):** The initial contact or heel contact is defined as the instant the foot makes contact with the floor. In healthy subjects, this occurs through the use of the heel, and continues until the sole of the foot is completely in contact with the ground (Flat Foot). It represents the moment in which the center of mass is in its lowest position and at the joint level the knee is extended, the hip flexed, and the ankle dorsiflexed [27].
 - (b) **Loading Response (Foot Flat):** This interval occurs when the sole of the foot comes into contact with the floor and the weight of the body is accepted onto the supporting limb. The loading response period coincides with the end of initial double limb support at approximately 10% to 12% of the stride [27].
 - (c) **Midstance:** This period involves the rotation of the tibia over the stationary foot in the direction of locomotion. The swinging limb

exceeds the supporting foot, and the center of mass reaches its highest point. The knee and hip begin to extend, and the ankle is dorsiflexed. The beginning of midstance coincides with single limb support and lasts from approximately 10% to 30% of the stride [27].

- (d) **Terminal Stance:** This period is characterized by the transfer of body weight from the hind and mid-foot regions onto the forefoot. It occurs from 30% to 50% of the stride and coincides with the beginning of terminal double limb support. The calf muscles initiate plantar flexion of the ankle, the knee extends again and then flexes slightly, and the hip is more extended [27].
- (e) **Pre-swing:** Pre-swing occurs simultaneously with terminal double limb support and lasts from approximately 50% to 60% of the stride. During pre-swing, weight is transferred onto the contralateral limb in preparation for the swing phase. It involves greater knee flexion and plantar flexion of the ankle but also a loss of hip extension.
- (f) **Final Contact (FC) or Toe Off (TO):** This corresponds to the end of pre-swing, the moment when the foot breaks contact with the floor, thereby demarcating the beginning of the swing phase. It starts with the Flat Foot and continues until the opposite foot lifts. In this period, the knee flexion is due to the limb's cushioning response because the weight of the body is transferred to the forelimb. There is plantar flexion of the ankle and the hip is still flexed from the initial contact [27].

All these events can be seen in the Figure 3.1.

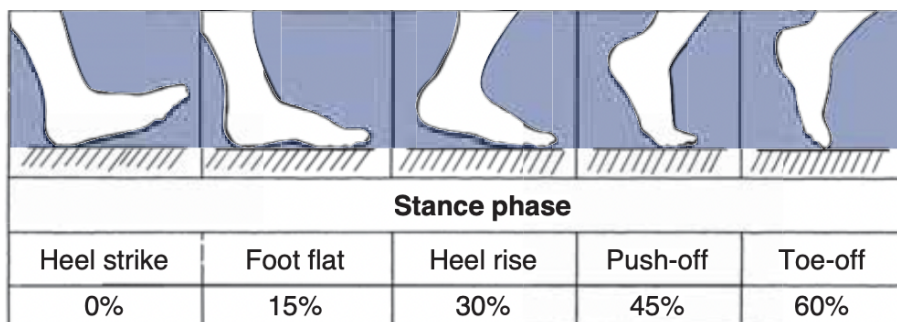


Figure 3.1: Illustration of the Stance Phase. [27]

- 2. **Swing Phase:** The swing phase occupies the remaining percentage of the gait cycle (38%) and corresponds to the period when the foot is not in contact with the ground, but rather in the air, as the leg extends toward

the next foot contact. It is associated with limb advancement. The swing phase can be further divided into three periods:

- (a) **Initial Swing:** This period is characterized by acceleration as the limb moves forward by lifting the foot through hip flexion and increased knee flexion. It lasts from approximately 60% to 73% of the stride (about one-third of the swing phase), starting from toe-off (TO) until the swinging foot aligns with the stance foot. The ankle is slightly dorsiflexed [27].
- (b) **Midswing:** This period extends from 73% to 87% of the stride and concludes when the swinging limb's tibia becomes vertically oriented. During midswing, there is further hip flexion, knee extension, and the ankle continues in dorsiflexion [27].
- (c) **Terminal Swing:** This is the final phase of the swing phase and also involves deceleration. It lasts from 87% to 100% of the stride, concluding at the moment of initial contact. The limb advancement is completed through knee flexion as the foot prepares to make contact with the ground. The hip is flexed, and the ankle is dorsiflexed in a neutral position [27].

In the Figure 3.2 both stance and swing phase are presented.

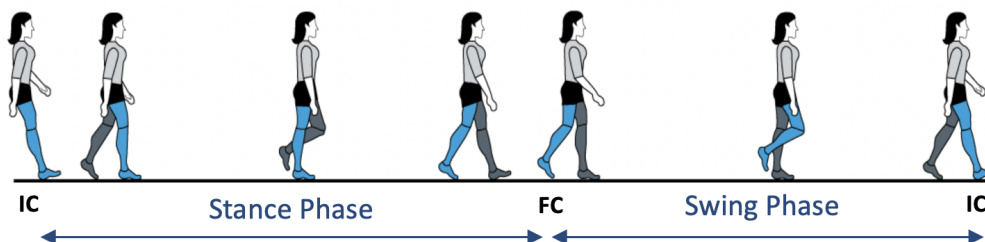


Figure 3.2: Schematic diagram of the spatial sequence of the gait cycle [27].

3.2 Gait global Characterization

As has been said, a stride could be defined as a sequence of the foot contact with the ground and the next contact of the same foot. Left and right strides are independent and a stride of one side overlaps with the preceding and subsequent strides of the opposite foot.[28] A step can also be defined as the sequence between a foot contact and the next contact of the opposite foot. Two steps, one for each side, constitute a stride. Gait parameters can be divided into temporal and spatial.

3.2.1 Temporal Parameters

Provides temporal references, these are the parameters that have to do with time, such as timing and duration [28]. This is where automation of gait research shows its true colors. These include:

- Cadence [step/min]: number of steps performed in a minute..
- Stride Time [sec]: stride duration.

3.2.2 Spatial Parameters

Looking at gait from a spatial perspective allows us to measure gait asymmetries related to distance between steps and stride lengths [28].

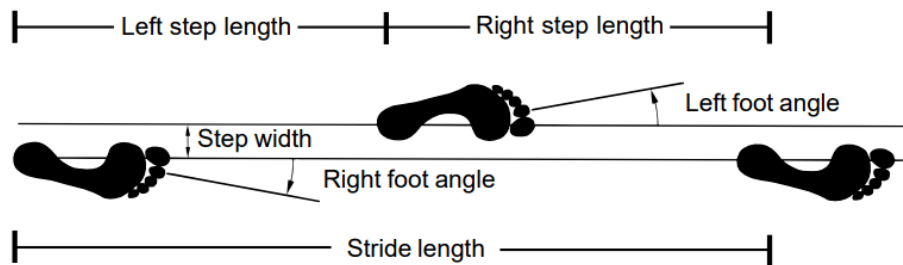


Figure 3.3: Spatial parameters representation.
[29]

The main spatial parameters studied in this project is:

- Stride Length [m]: distance between a point at the first contact of the foot with the ground and the point on the same foot at the next contact. The stride length determines the local gait direction of progression;

3.2.3 Velocity Parameters

The velocity parameters of gait refer to the specific measurements and characteristics related to the speed at which a person walks or runs [30]. In this thesis the velocity parameter studied is:

- Walking Speed [m/sec]: distance traveled in a given time, the average one is basically the product between the cadence and the length of the stride. The speed depends on the length which in turn depends above all on the duration of the oscillation phase on each side.

3.3 Gait Analysis Instrumentation Systems

The study of human motion biomechanics, particularly gait analysis, can be conducted using qualitative or quantitative methods. Qualitative analysis describes movements as models through expert observation, while quantitative analysis employs numerical terms and aims for objectivity and comparability using evaluation scales and acquisition tools.

Quantitative analysis methods include optical and non-optical motion capture systems. Optical systems use cameras and markers, while non-optical systems utilize various instruments based on inertial, electromagnetic, electromechanical, or acoustic principles. Wearable systems use body sensors, while non-wearable systems prioritize comfort and often employ RGB systems. The main technologies used in this project are the SP system and multi-sensor wearable system with IMUs, pressure insoles and distance sensors. Inertial electromechanical sensors, such as accelerometers, gyroscopes, and magnetometers, measure linear and angular accelerations, rotation angles, and magnetic fields. Pressure insoles capture the distribution of forces during gait, while distance sensors provide measurements related to stride length or step distance. Optical systems rely on cameras, markers, and specialized hardware and software. In this section, we provide a summary of the operational principles of the aforementioned systems.

3.3.1 Optoelectronic stereophotogrammetry

The optoelectronic stereophotogrammetry is usually considered as a Gold Standard system in laboratories, is one of the most popular motion capture systems. The SP system works by tracking the trajectories of spherical retroreflective markers positioned in the anatomical points of interest over the subject.

Optical Motion Capture Process

The SP system enables the capture of 2D grayscale images using infrared (IR) cameras, which need to be calibrated before use [31]. This calibration process allows for the extraction of labeled two-dimensional positions of markers from the pixel-based image planes through image processing techniques like linear thresholding. The next step involves transitioning from the 2D to 3D space, requiring the capture of a single marker by at least two cameras to reconstruct its position. Specifically, 3D correspondences are established between the two camera views and then triangulated, resulting in a reconstruction that places all the markers within a common coordinate frame [31].

During the calibration phase, a series of markers mounted on a predefined geometric structure (Active wand) are used. This structure is moved around the

laboratory while being recorded, allowing for the acquisition of an image of the markers with a known geometry [32]. By utilizing the known geometric information, the relationship between the x-y coordinates (which represent the projection of individual markers from the image planes onto the cameras) and the 3D coordinates of the markers can be understood. This relationship facilitates the reconstruction of the 3D position of a marker recorded by at least two cameras providing 2D information [32].

Using the acquired information during the data acquisition phase, an inverse relationship is applied to estimate the 3D coordinates from the 2D coordinates. To achieve this, the correspondence between each marker and its respective point in the point cloud needs to be determined. A naming convention is assigned to each marker, enabling the identification of specific points corresponding to markers placed at anatomical locations (using component labeling and 3D correspondence search) [31].

At this stage, for each frame of acquisition, a point cloud is obtained representing the 3D positions of individual markers. The next step involves reconstructing the local reference system that defines the orientation of each body segment. The marker retirement protocol used determines this orientation reconstruction. The simplest approach is to obtain the orientation of a segment by utilizing at least three markers: two markers defining the longitudinal axis of the segment, one marker for the medio-lateral axis, and one marker for the anteroposterior axis. Using the 3D coordinates of these individual markers, the orientation of the segments in space can be reconstructed for each sampling instant. This process is also known as rigid body search [31].

This entails searching for and assigning rigid marker targets within the 3D point cloud and recovering their poses. All the obtained information must be related to a human model. Consequently, the trajectories of the markers, representing specific parts of the body, become known outputs. Subsequently, various other quantities such as joint kinematics, spatio-temporal parameters, events, etc., can also be derived. In Figure 3.4 a flowchart of the whole process can be beheld.

3.3.2 Multi-sensor wearable systems

Multi-sensor wearable systems, like the INDIP system, have gained significant attention in recent research due to their potential to capture comprehensive and detailed information about human movement. These wearable devices integrate multiple sensors, such as accelerometers, gyroscopes, and magnetometers, to capture various aspects of human motion. Accelerometers measure linear acceleration, gyroscopes capture angular velocity. This combination of sensors allows for a more holistic understanding of the complex movements involved in gait. Moreover, multi-sensor wearable systems often incorporate additional sensors like pressure

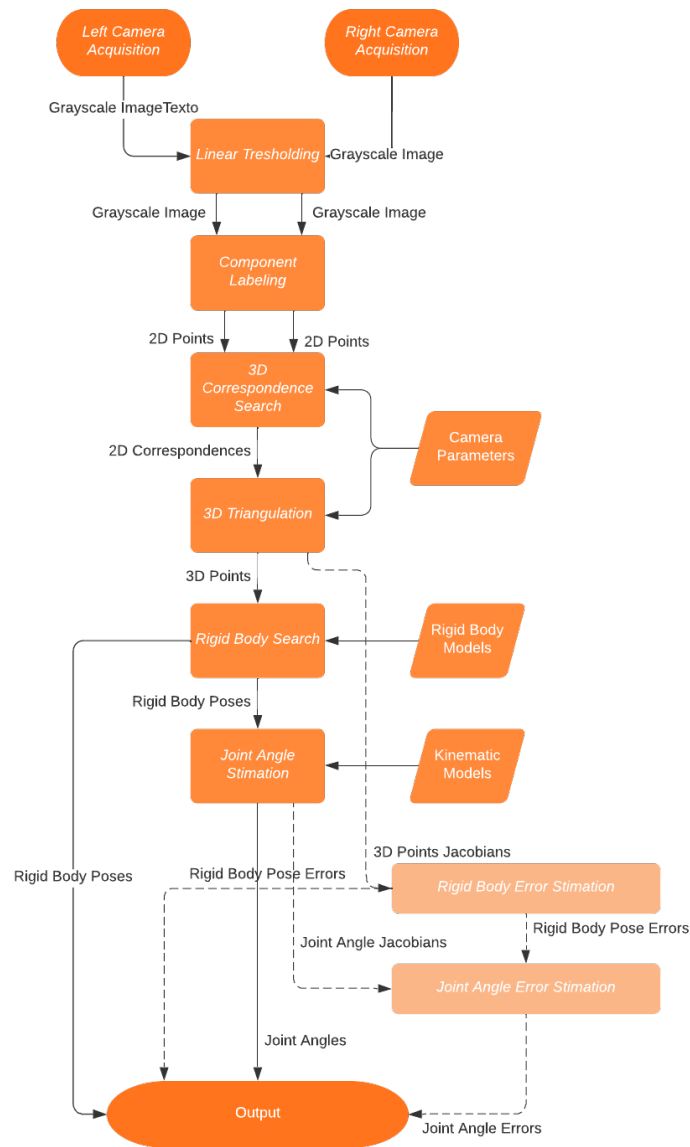


Figure 3.4: Optical motion capture process flowchart.

insoles and distance sensors. Pressure insoles provide valuable information about the distribution of forces during gait, enabling analysis of foot pressure patterns and identifying potential gait abnormalities. Distance sensors, on the other hand, offer measurements related to stride length or step distance, providing insights into the spatial parameters of gait [6]. By integrating data from these different sensors, it is possible to obtain a more comprehensive and accurate assessment of

gait parameters. The IMUs contribute to capturing the dynamic movements and orientation of the body during walking, while the pressure insoles provide insights into the forces exerted by the feet and the timing of foot contact with the ground. Distance sensors complement this information by offering spatial measurements related to the stride length or step distance [33].

Sensor fusion techniques can be applied to merge and synchronize the data from these sensors, enabling a more holistic analysis of gait. By combining information on body movements, forces exerted on the feet, and distance information, errors can be reduced, and a more detailed characterization of gait can be achieved. This integrated approach allows for a more comprehensive understanding of gait patterns, detection of gait abnormalities, and monitoring of rehabilitation progress.

3.3.3 Magneto-Inertial Measurement Units

Wireless sensor-based systems using magneto-inertial measurement units (MIMUs) have emerged as an alternative to camera-based laboratory systems. These sensors, which typically include tri-axial accelerometers, gyroscopes, and magnetometers, offer advantages such as light weight, portability, low costs, and miniaturization, enabling outdoor analysis over extended periods of time. In the case of MIMUs, orientation estimates are derived from the sensor's alignment with gravity (accelerometer), the Earth's magnetic field (magnetometer), and angular velocity (gyroscope). These estimates are represented in quaternion format, which defines 3D rotations in space [9]. However, in the specific project mentioned, the devices are referred to as IMUs instead of MIMUs, as the magnetometer data is excluded due to limited usability.

Despite their advantages, sensor-based systems have limitations that should be considered. One such limitation is the presence of drift, which introduces errors and leads to inaccurate orientation estimations. Ferromagnetic disturbances also affect IMUs and can result in errors in heading accuracy [9]. To mitigate these errors, various data correction algorithms can be employed. Furthermore, inaccuracies in sensor-based spatiotemporal parameters may arise from misalignment between anatomical and sensor-based body segment coordination systems. Calibrating these two coordination systems can help reduce such errors and improve accuracy.

Nevertheless, despite these limitations, wireless sensors have been successfully utilized in obtaining spatiotemporal parameters during gait analysis [34].

Accelerometer

An accelerometer measures proper linear acceleration, which refers to the physical acceleration experienced by an object. This can be expressed as:

$$\mathbf{a}_p = a_s - g \quad (3.1)$$

Thus, acceleration is measured relative to a free-falling or inertial observer who is temporarily at rest in relation to the object being measured. Since gravity acts uniformly on the inertial observer, it does not contribute to the proper acceleration [35].

The equivalence principle ensures the existence of a local inertial frame at every point in spacetime, and an accelerometer measures acceleration relative to that frame. These accelerations are often referred to as g-forces, which represent forces relative to ordinary gravity. On the Earth's surface, a normal force is exerted upwards with respect to the local inertial frame. Therefore, an accelerometer at rest relative to the Earth will read approximately 1 g upwards (the frame of a freely falling object near the surface). To obtain accurate measurements, this "gravity offset" must be subtracted from the acceleration resulting from motion relative to the Earth, and adjustments must be made for any effects caused by the Earth's rotation in relation to the inertial frame [35].

An accelerometer can be modelled as a second order spring mass damper system. When an acceleration (a) is applied to proof mass (m) suspended by springs with a spring constant (k), and having a damping (b), then the force ($F_{applied}$) acting on the proof mass is given by:

$$F_{applied} = ma_{applied} \quad (3.2)$$

The force exerted by springs and damping in the system can be defined as:

$$F_{spring} = kx \quad (3.3)$$

$$F_{damping} = b\dot{x} \quad (3.4)$$

Applying Newton's second law which states that the algebraic sum of all the forces equals the inertial force of the proof mass:

$$F_{applied} + F_{spring} + F_{damping} = m\ddot{x} \quad (3.5)$$

$$m\ddot{x} + b\dot{x} + kx = F_{applied} = m\ddot{x}_g = ma \quad (3.6)$$

The transfer function $H(s)$ of the system is given by:

$$ms^2x(s) + bsx(s) + kx(s) = F_{applied} = ma \quad (3.7)$$

$$s^2x(s) + \frac{b}{m}sx(s) + \frac{k}{m}x(s) = a(s) \quad (3.8)$$

$$H(s) = \frac{x(s)}{a(s)} = \frac{1}{s^2 + \frac{b}{m}s + \frac{k}{m}} = \frac{1}{s^2 + \frac{\omega_0}{Q}s + \omega_0^2} \quad (3.9)$$

ω_0 is the resonance frequency and (Q) is the quality factor given by:

$$\omega_0 = \sqrt{\frac{k}{m}} \quad (3.10)$$

$$Q = \frac{m\omega_0}{b} \quad (3.11)$$

Accelerometers work in the low frequency domain ($\omega \ll \omega_0$) with their mechanical sensitivity calculated by setting $s = 0$ in the transfer function $H(s)$ to get:

$$\frac{x}{a} \approx \frac{m}{k} = \frac{1}{\omega_0^2} \quad (3.12)$$

We require a high resonance frequency to have a wide sensing bandwidth, which can be attained by decreasing the size of the proof mass and increasing the stiffness of the springs. Unfortunately, the device's sensitivity is decreased as a result. There is a trade-off between sensitivity and bandwidth as a result[35].

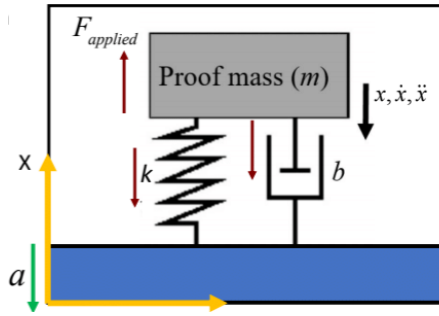


Figure 3.5: Model of an Accelerometer [35].

Gyroscope

As an inertial sensor, the gyroscope measures the angular velocity (rate) or angle of rotation (rate integrating) of an object. The Coriolis vibration gyroscope (CVG) is a type of gyroscope that uses vibrational elements to determine angle or angular velocity and is based on the Coriolis principle. It has a simple structural design and relies less on rotating elements than earlier mechanical rotor gyroscopes. The CVG is a great contender for gyroscope miniaturization because it combines the benefits of MEMS technology with large quantity, low cost, tiny size, lightweight, and low power consumption. On the other hand, the MEMS CVGs are able to detect multi-axis angular velocity on a single-chip architecture, in contrast to other kinds of gyroscope [36]. Considering a disk rotating about a vertical axis with a constant angular velocity ω and a mass m oscillating with a transverse velocity v_t .

From an observer fixed with the rotating disk, it appears that a force F_c perpendicular to the velocity v_t acts to oscillate the mass along the perpendicular direction.

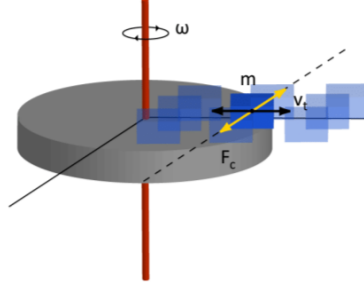


Figure 3.6: Model of a rotating disk for gyroscope explanation [36].

F_c is proportional to the angular velocity, the displacement is proportional to the force F_c . By measuring the displacement of the mass along the perpendicular direction it is possible to determine the angular velocity .

$$F_c = -2mv_t \times \omega \quad (3.13)$$

The driving mode of the MEMS vibrating gyroscope provides a constant and continuous vibration along the driving axis, and the sensing mode detects the movement of the vibration along the sensing axis when an external rotation is provided. These two operational modes make up the fundamental structure of the MEMS vibrating gyroscope [36].

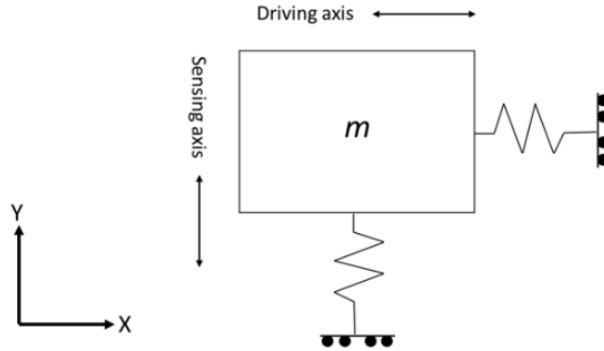


Figure 3.7: Simple depiction of a proof mass vibrating system [36].

The simplest two degrees of freedom equations of motion for MEMS vibrating gyroscopes and the equation of the Coriolis force are:

$$m \frac{d^2x}{dt^2} + c \frac{dx}{dt} + kx = F_D + 2m\Omega \frac{dy}{dt} \quad (3.14)$$

The response of the sensing mode is generally very small in magnitude compared to the driving mode response, so the Coriolis force $2m\Omega\frac{dy}{dt}$ will become negligible:

$$m\frac{d^2x}{dt^2} + c\frac{dx}{dt} + kx = F_D \quad (3.15)$$

$$m\frac{d^2y}{dt^2} + c\frac{dy}{dt} + ky = F_S - F_C \quad (3.16)$$

where F_D, F_S , and F_C are the driving, sensing, and Coriolis forces, respectively, m is the inertial mass, x is the displacement of the driving motion, y is the displacement of the sensing motion, c is the damping coefficient, k is the stiffness constant, and Ω is the external rotation rate [36].

In the Figure 3.8 the simplest vibratory gyroscope structure is shown. The sensing system is made up of a Coriolis force detector, while the driving system is made up of driving electrodes that produce oscillations with a specific amplitude. When the driving electrodes deliver a consistent and continuous momentum along the driving axis direction, the proof mass begins to oscillate. The identical proof mass rotates outside, which causes it to oscillate in the opposite direction from the driving axis. The driving momentum and external rotation combine to produce the Coriolis force, which is detected by the detecting electrodes on the orthogonal axis.

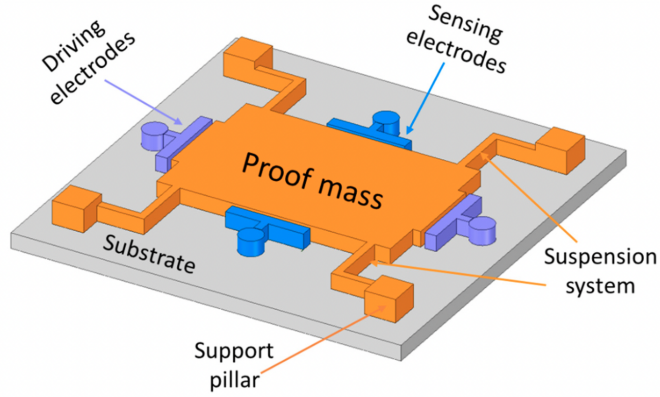


Figure 3.8: Schematic architecture of a single proof mass vibrating gyroscope [36].

The output error model of the MIMU gyroscope at room temperature is created in accordance with the error source and output characteristics of the gyroscope without taking the impact of temperature changes into account [37], as indicated in equation 3.17:

$$\begin{bmatrix} W_x \\ W_y \\ W_z \end{bmatrix} = \begin{bmatrix} \omega_{x0} \\ \omega_{y0} \\ \omega_{z0} \end{bmatrix} + \begin{bmatrix} L_{\omega x} & K_{\omega xy} & K_{\omega xz} \\ K_{\omega yx} & L_{\omega y} & K_{\omega yz} \\ K_{\omega zx} & K_{\omega zy} & L_{\omega z} \end{bmatrix} \begin{bmatrix} \omega_x \\ \omega_y \\ \omega_z \end{bmatrix} \quad (3.17)$$

Where, $W_i (i=x,y,z)$ is the measured angular rate, $\omega_{i0} (i=x,y,z)$ represents the zero bias, $\omega_i (i=x,y,z)$ is the real angular rate, $K_{\omega ij} (i,j=x,y,z, i \neq j)$ represents the non-orthogonal installation error coefficient, $L_{\omega i} (i=x,y,z)$ represents scale factor.

The gyroscope's error compensation model can be generated using the output error model discussed before, as illustrated in equation 3.18 :

$$\begin{bmatrix} \omega_x \\ \omega_y \\ \omega_z \end{bmatrix} = \begin{bmatrix} L_{\omega x} & K_{\omega xy} & K_{\omega xz} \\ K_{\omega yx} & L_{\omega y} & K_{\omega yz} \\ K_{\omega zx} & K_{\omega zy} & L_{\omega z} \end{bmatrix}^{-1} \begin{bmatrix} W_x - \omega_{x0} \\ W_y - \omega_{y0} \\ W_z - \omega_{z0} \end{bmatrix} \quad (3.18)$$

3.3.4 Pressure Insoles

Pressure insoles (PI) are devices used to measure and analyze the distribution of pressure on the feet during walking or other weight-bearing activities. They consist of thin, flexible sensor arrays that are inserted into the shoes, between the foot and the sole, and connected to a data acquisition system that records and analyzes the pressure patterns [38].

In prior studies the effectiveness of pressure-sensitive insoles to estimate ground-reaction force in real-time with reasonable accuracy has been proved [39]. These insoles have also proven to be beneficial for gait segmentation, enabling the provision of sensory feedback based on different phases of the gait cycle [40]. This particular sensing technology, offers advantages such as cost-effectiveness, immunity to temperature changes, and the elimination of unnecessary calibration procedures, making it suitable for everyday use [39].

There are different types of pressure insoles, including capacitive, resistive, and piezoresistive sensors. Capacitive sensors measure changes in the capacitance of a thin film in response to pressure, while resistive sensors use changes in resistance to measure pressure. Piezoresistive sensors use piezoresistive materials that change their resistance in response to applied pressure [41].

Several studies have evaluated the accuracy and reliability of pressure insoles. One study compared different types of pressure insoles and found that capacitive insoles provided the most reliable and accurate measurements of pressure distribution during walking [41]. Another study used pressure insoles to measure the effect of footwear on pressure distribution during walking and found that footwear with soft soles decreased pressure under the forefoot and heel, while footwear with hard soles increased pressure under the forefoot and midfoot [42].

The PI and their respective algorithms included in the INDIP system has already been validated for gait event identification in overground terrain [43]. Where the utilization of low-cost PI in conjunction with specific signal processing algorithms demonstrated minimal errors for both IC and FC. Then, these PI has been validated for characterizing gait by integrating them with IMUs as part of a multi-sensor

wearable system [6]. This integration enables accurate temporal estimations and facilitates a more comprehensive assessment of gait, even in real-world, free-living environments.

In the Figure 3.9 pressure insoles from the INDIP system are shown, these insoles contain 16 resistive pressure sensors that allow to measure more accurately the pressure made from each part of the foot.



Figure 3.9: Pressure insoles from INDIP System.

3.3.5 Distance Sensors

Distance sensors (DS) , also known as proximity sensors, are devices that measure the distance between the sensor and an object. These sensors use a variety of technologies to detect the presence of an object, including ultrasound, infrared, and laser.

Ultrasound sensors emit high-frequency sound waves and measure the time it takes for the waves to bounce back off of an object. These sensors are commonly used in applications such as parking sensors, object detection in robotics, and distance measurement in industrial applications [44].

Infrared sensors use infrared light to detect the presence of an object. These sensors are commonly used in applications such as proximity sensors in smartphones, motion sensors in home security systems, and obstacle detection in robotics [44].

Laser sensors emit a laser beam and measure the time it takes for the beam to bounce back off of an object. These sensors are commonly used in applications such as rangefinders, robot navigation, and distance measurement in industrial applications [44].

DS in gait studies and particularly with the INDIP system are time-of-flight infrared distance sensors to detect the alternating movements of the lower extremities. These DS were used in a previous study to evaluate a novel step-detection method called the inter-foot distance step counter (IFOD), which directly measures the distance between the feet [44]. By focusing on inter-foot distance, the IFOD method offers a unique approach to step detection, potentially overcoming limitations encountered by traditional IMU-based methods in challenging walking conditions.

Chapter 4

Materials

This chapter focuses on the acquired data, providing a detailed explanation of the systems utilized throughout the experiments. A comprehensive overview is provided regarding the selection of patients, the experimental protocol, and the setup established to gather the necessary data. Additionally, emphasis is placed on the methods employed for data processing, organization, and statistical analysis, highlighting their significance in ensuring accurate and reliable results. The chapter not only outlines the technical aspects of the data acquisition process but also delves into the steps taken to prepare the data for subsequent analysis, making it a comprehensive resource for understanding the entire experimental workflow.

4.1 VICON System

The Vicon Motion Capture System is a SP system widely regarded as the most precise and accurate motion capture (MOCAP) solution currently available [45]. It is utilized in gait analysis, rehabilitation, and can be integrated with other devices such as force plates or EMG sensors. It supports multiple programming languages, including Matlab and Python.

4.1.1 Hardware Components

Active Wand

The Vicon Active Wand is an electronic motion capture calibration device that contains five LEDs. The Active Wand is used to calibrate both optical and reference video cameras. As some reference video cameras don't have strobes, the LEDs in the Active Wand make it easier to identify and locate markers from the reference video camera images. [46]. This is first used for the dynamic calibration of the cameras once the LEDs start flashing, as soon as the brightness stabilizes it means

that the cameras and the wand are synchronized, then the wand it needs to be shaken in all the analysis volume up to the point in which the software indicates a successfully calibration.



Figure 4.1: Active Wand.

Motion Capture Cameras

For this project, fourteen infrared cameras are used as seen in Figure 4.3. These are positioned at the top on fixed and immobile supports (Truss System) to avoid movements that could affect the accuracy of the results (Figure 4.2).



Figure 4.2: Truss System for Vicon Cameras.

Markers

In motion capture two different types of markers are used, these are passive or active. In this particular work only passive markers were used (Figure 4.4). These

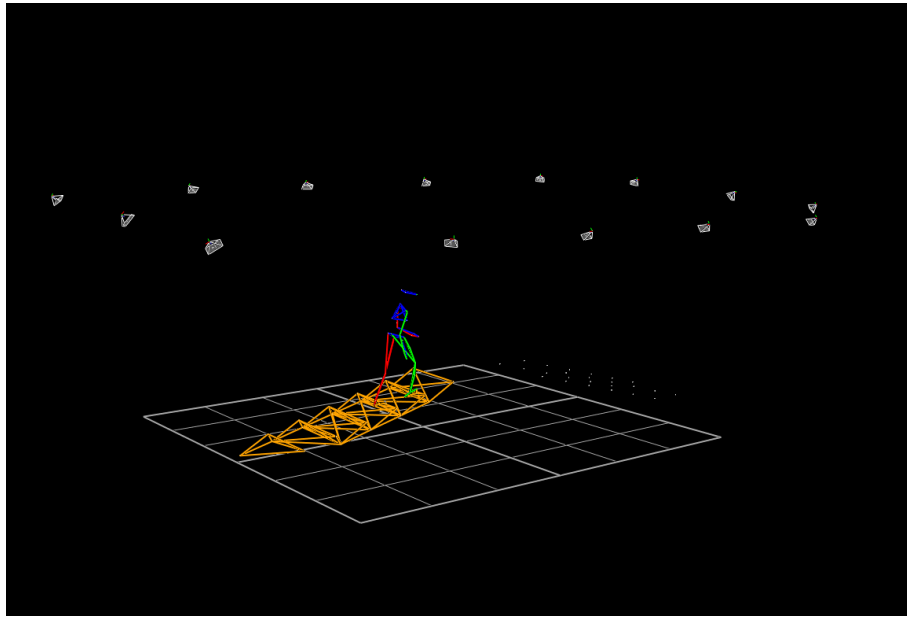


Figure 4.3: Vicon Cameras Positioning in Nexus Software.

types of markers are retroreflective, they reflect light when illuminated in the infrared.



Figure 4.4: Vicon Passive Markers.

4.1.2 Camera Calibration Process

This is a step for determining the calibration matrix that maps coordinates in the 3D world into the 2D image. This can be recovered linearly by the Direct Linear Transform Method. The output from this method are the parameters of the cameras that allow to find, starting from the 3D coordinates of the markers

recorded by the cameras, the 2D coordinates of a single marker.

4.1.3 Software

The software used is called Nexus, this is used for analyzing and obtaining the output data that retrieves the motion capture system. The software allows the creation and labelling of a 3-dimensional skeleton for the whole bunch of tests by considering the set of markers used and the antropometric parameters of the subject, such as height, weight, and length of the body segments. Then, from the predefined biomechanical model, the kinematic and/or kinetic parameters of interest, the names of the markers used, and the relationships between them are extracted.

First, a static test is carried out, with the subject standing in the center of the movement volume considered by the cameras so the system is allowed to collect all the data on the markers positioned on the subject.

4.2 INDIP System

This is a inertial based system which includes a magneto-inertial unit sensor, a distance sensor, and a plantar pressure insole combining them into a multi-sensor werable system. A comprehensive depiction of the INDIP system hardware has been presented in [6], offering detailed information about its components and specifications. Additionally, each of the advanced algorithms incorporated in the INDIP computational pipeline has been thoroughly explained in the same article, where respective algorithms have been previously described, validated, and evaluated.



Figure 4.5: INDIP System with PI, IMUs and DS.

4.3 Data Collection

Ten healthy subjects (Table 4.1) were chosen to be studied in different terrain conditions. All of the experiments were performed in the Hospital "Los Madroños" located in Brunette, Spain. The phases of the study are listed as:

- Phase 1: Recruiting subjects following the inclusion and exclusion criteria listed above.
- Phase 2: Providing information to the participant about the structure, duration, and other relevant topics of interest for the experiment, and obtaining the informed consent signature.
- Phase 3: Experimentation and data acquisition with INDIP, and VICON.
 - Instrumenting the subjects.
 - Conducting the tests.
 - De-instrumenting the subjects.
- Phase 4: Data processing and obtaining results.
- Phase 5: Evaluating the results based on metrics.

Table 4.1: Summary of participants for trials acquisitions.

Subject	Gender (M/F)	Age (y)	Height (cm)	Weight (Kg)	Shoe Size
1	F	23	170	66	39
2	F	24	163	55	39
3	F	25	168	57	38
4	M	23	182	78	43
5	F	32	166	57	37
6	F	26	164	53	39
7	F	25	170	60	37
8	M	24	183	80	43
9	F	24	162	52	39
10	M	24	179	65	41

4.4 Subject Selection

People participating in this study met the inclusion/exclusion criteria designed for this project. These criteria are the following:

Inclusion Criteria:

- Age between 18 and 50 years.
- Do not have any medical condition which prevent the subject to walk over irregular terrain or slope.
- Do not have any skin sensibility that does not allow the use of measure instrumentation.
- Height of 150 to 195 meters.
- Both genres.
- A maximum wight of 100 kg.
- Capable of following instructions.

Exclusion Criteria:

- Pregnant, lactating or postmenopausal woman.
- Usage of an external device that supports the spine or head, neck, or trunk.
- Hospitalization due to heart attack, cardiac surgery, or acute heart failure within 3 months prior to study entry or cardiovascular disease or major deep vein thrombosis (DVT) in the lower extremities (within the last 3 months)).
- Suffer balance disturbances.

It is important to emphasize that after the complete acquisition process, certain subjects had to be excluded from the study. The first two subjects were excluded due to a protocol change, the sixth subject experienced an issue with INDIP, and the acquisitions with the last subject could not be completed due to personal reasons. At the end, only data from six subjects were considered for the final results.

4.5 Experimental Protocol

The protocol involves a single experimental session for each evaluated case. The session begins with an explanation and clarification phase of the protocol to be followed.

The participant is instrumented with the measurement systems - VICON and INDIP - and the necessary anthropometric measures are taken. The participant performs different walks on a walkway (Figure 4.6), which may be in a horizontal

position or inclined at a 15-degree angle. The platform system consists of a 7 x 1 m walkway composed of two lateral platforms of 3 x 1 m joined to a central platform of 1 x 1 m by means of hinges. Beneath the central platform, there is a hydraulic lifting platform capable of reaching a height of up to 2 m. The created mechanism allows generating terrain inclinations on the lateral ramps of up to 15 degrees. Different terrains with varied hardness and shape are placed on top of this walkway. The participant performs four walks for each terrain condition



Figure 4.6: Base platform for experiments.

(approximately 4 min per condition), one trial is considered as a one-way walk. The conditions to be performed are listed in the following list:

- Flat terrain with the platform at 0 and 15 degrees. The flat terrain or over-ground is always necessary to start with a reference system. (2 configurations). Figure 4.6
- Wooden modules with a 15-degree inclination, in the sawtooth configuration. These are used to simulate terrain with positive and negative slopes. The tests will be carried out on the platform at 0 and 15 degrees. These modules are not symmetric so the subject will walk in an upward direction and in a downward direction, both in 0° and 15° . In this case each step will have a positive slope or negative slope with an angle that will vary respect of the platform inclination. (4 configurations). Figure 4.8.
- Unstructured terrain modules with the platform at 0 and 15 degrees. This is a soft terrain trying to simulate a mountain terrain with different floor irregularities. (2 configurations). Figure 4.8

- Mat with the platform at 0 and 15 degrees. (2 configurations). To replicate challenging conditions such as mud or surfaces that pose difficulty in executing FC, a soft terrain is simulated by placing a mat. Figure 4.8.

A resume of all terrain conditions with their respective condition number can be found in Table 4.2.

# Condition	Terrain	Degree
1	Overground	0°
2	Overground	15°
3	Mat	0°
4	Mat	15°
5	Unstructured	0°
6	Unstructured	15°
7	Sawtooth Upward	0°
8	Sawtooth Upward	15°
9	Sawtooth Downward	0°
10	Sawtooth Downward	15°

Table 4.2: Terrain conditions name and numbers.

In Figure 4.7 a graphic representation of all the conditions is presented.

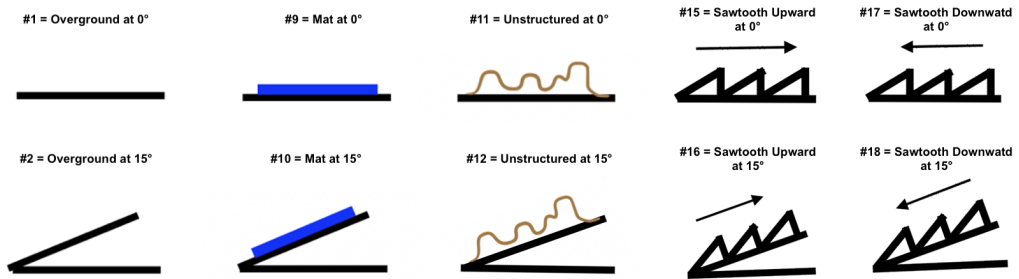


Figure 4.7: Graphical representation of each terrain condition.

The chronological sequence of the type of terrain is chosen randomly for each subject, completing all proposed combinations. The subject has 5 minutes of rest during the change of terrain. The subject performs the test at a comfortable speed, with which they feel safe and stable. Once the tests are completed, the markers and sensors are removed, and the study concludes. There are 10 configurations in total, so considering three walks and three returns per configuration, 60 acquisitions are obtained for each subject, taking a total time of approximately 60 minutes of acquisitions. Considering 5 minutes of terrain changes, a total of 40 minutes

is added. In summary, the total time of participation in this experiment is 100 minutes. The walking path from one side to the other of the platform is treated as a trial, without distinguishing between walking and returning. However, this distinction is only relevant in the case of the Sawtooth terrain, because of its asymmetry. A total amount of 600 data files from VICON and another 600 files from INDIP were acquired.

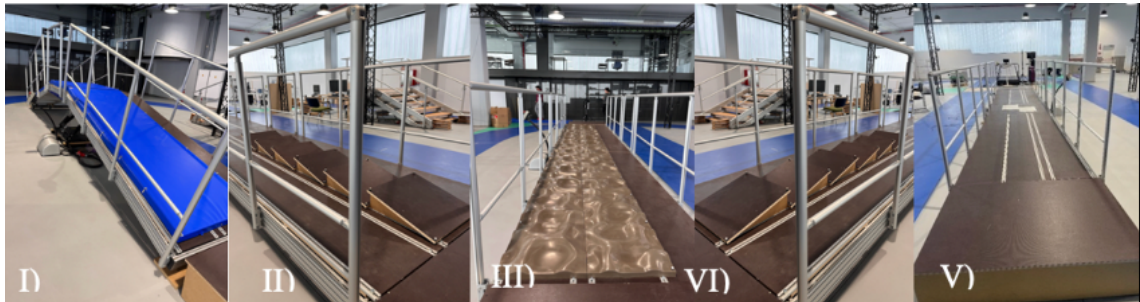


Figure 4.8: I) Mat terrain, II) Downward Sawtooth Terrain, III) Unstructured Terrain, VI) Upward Sawtooth Terrain, V) Plane Terrain.

It is important to note that an Excel sheet was maintained throughout the acquisition process. Table 4.3 presents an example of this table, which includes details such as trial information or file name, acquisition start time, Vicon trial number, GoPro video number, terrain description, acquisition state, and any relevant problems or additional information. This Excel sheet serves not only to describe the conducted experiment but also plays a crucial role in renaming the raw data exported by the INDIP system.

4.5.1 Systems Calibration

Before starting the acquisition both VICON and INDIP systems need to be calibrated.

Vicon Calibration.

For calibrating Vicon, as it has been introduced in Chapter 4, the following steps were performed:

- Active wand connection: The active wand was securely connected to the Vicon system. The active wand contained markers that emitted infrared signals, which were used for calibration.
- Preparation of calibration space: The Vicon cameras were set up in the desired configuration for calibration. The cameras had a clear view of the calibration

Table 4.3: Experiments description sheet.

File_name	Time	Vicon	GoPro	Description	State
subject_06_cond_15_run	17:28	4	GX015138	Upward Sawtooth	OK
subject_06_cond_15_run	17:29	5	GX015139	Upward Sawtooth	NO.
subject_06_cond_15_run	17:29	6	GX015140	Upward Sawtooth	OK
subject_06_cond_17_run	17:33	1	GX015141	Downward Sawtooth	OK
subject_06_cond_17_run	17:33	2	GX015142	Downward Sawtooth	OK
subject_06_cond_17_run	17:34	3	GX015143	Downward Sawtooth	OK
subject_06_cond_17_run	17:34	4	GX015144	Downward Sawtooth	OK
subject_06_cond_17_run	17:35	5	GX015145	Downward Sawtooth	OK
subject_06_cond_17_run	17:35	6	GX015146	Downward Sawtooth	OK
subject_06_cond_09_run	18:27	1	GX015171	Mat	OK
subject_06_cond_09_run	18:27	2	GX015172	Mat	OK
subject_06_cond_09_run	18:28	3	GX015173	Mat	OK
subject_06_cond_09_run	18:28	4	GX015174	Mat	OK
subject_06_cond_09_run	18:29	5	GX015175	Mat	OK
subject_06_cond_09_run	18:29	6	GX015176	Mat	OK
subject_06_cond_10_run	18:31	1	GX015177	Mat slope	OK
subject_06_cond_10_run	18:31	2	GX015178	Mat slope	OK
subject_06_cond_10_run	18:32	3	GX015179	Mat slope	OK
subject_06_cond_10_run	18:32	4	GX015180	Mat slope	OK
subject_06_cond_10_run	18:32	5	GX015181	Mat slope	OK

space, and obstructions were avoided. The Vicon software was launched: The Vicon software was opened on the computer, and the appropriate calibration option was selected.

- Active wand definition as a calibration tool: The active wand was designated as a calibration tool in the Vicon software.
- Calibration process performance: The instructions provided by the Vicon software were followed to perform the calibration. The active wand was waved within the calibration space while the Vicon cameras tracked its movements.
- Calibration data collection: The active wand was moved around the calibration space in various orientations and positions. The Vicon cameras tracked the markers on the wand, collecting data to calibrate the system.
- The calibration was completed: Once sufficient data was collected, the Vicon software processed the information and generated a calibration result. This

calibration result was used to improve the accuracy of the motion capture system.

- **Reference axis definition:** After calibration, the active wand was positioned in the middle of the platform for setting the reference axis.

INDIP Calibration

- **IMU Static Test:** static acquisition using the 3 INDIP MIMUs. In this test, the operator places all the devices on a level surface and initiates an acquisition that lasts for a minimum of 60 seconds. It is important to avoid any knocking or movement of the sensors during the acquisition.
- **Pressure Insoles Static Test:** this is conducted to ensure their proper functionality. During this test, an operator records the signals from the pressure insoles by applying pressure to the individual sensing units one by one. The order in which the sensing elements are pressed is not significant. This procedure is performed separately for both the right and left pressure insoles, one acquisition at a time.
- **Standing Test:** a brief static acquisition is conducted with the participant wearing all the INDIP MIMUs, pressure insoles, and distance sensors as shown in Figure 4.12. The participant is instructed to maintain a stationary position for a minimum of 10 seconds. This test is necessary to determine the orientation of the MIMUs in the global framework, enabling the computation of a rotation matrix to align the MIMU recordings during dynamic acquisitions. The recorded signals for the IMUS are presented in Figure 4.9.
- **Data Personalization Test:** this test is conducted to ensure proper placement of the pressure insoles inside the shoes and to identify any sensors that may not activate correctly. The test involves the following steps:
 - Stand still for a minimum of 10 seconds.
 - Lift the left foot and maintain the position for at least 5 seconds, representing a single right support phase.
 - Stand still again for at least 5 seconds, representing a double support phase.
 - Lift the right foot and hold the position for 5 seconds, representing a single left support phase.
 - Stand still once more for at least 5 seconds, representing a double support phase.

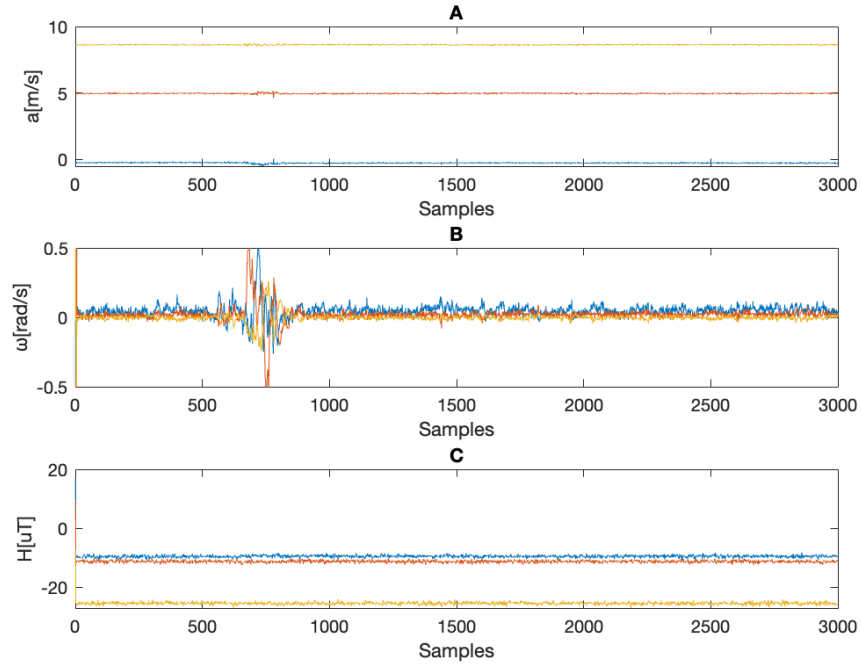


Figure 4.9: Signals for the Standing acquisition for the right foot of subject 3. A) Accelerometer readings; B) Gyroscope readings; C) Magnetometer readings.

- Walk comfortably at a normal pace along a J path where the subject starts walking and then returns to a point that is distanced from the initial point, creating an imaginary J on the floor. These actions are performed to validate the correct functioning and positioning of the pressure insoles, as well as to capture relevant data for personalization purposes. Personalization signals are presented in Figure 4.10.

4.6 Instrumentation

The participants were equipped with the two motion capture systems:

- i) The placement of 43 reflective optical markers required for the photogrammetry-based system (VICON) was performed. These markers were positioned according to the Plug-in-gait standard model on the subject’s chest, legs, and feet, following the arrangement shown in Figure 1 (estimated duration: 15 minutes). To prevent markers from being obscured by uneven surfaces, two additional markers were included on each side of the feet. This was done to mitigate the possibility of marker loss caused by surface irregularities. Additionally, each terrain was designated with

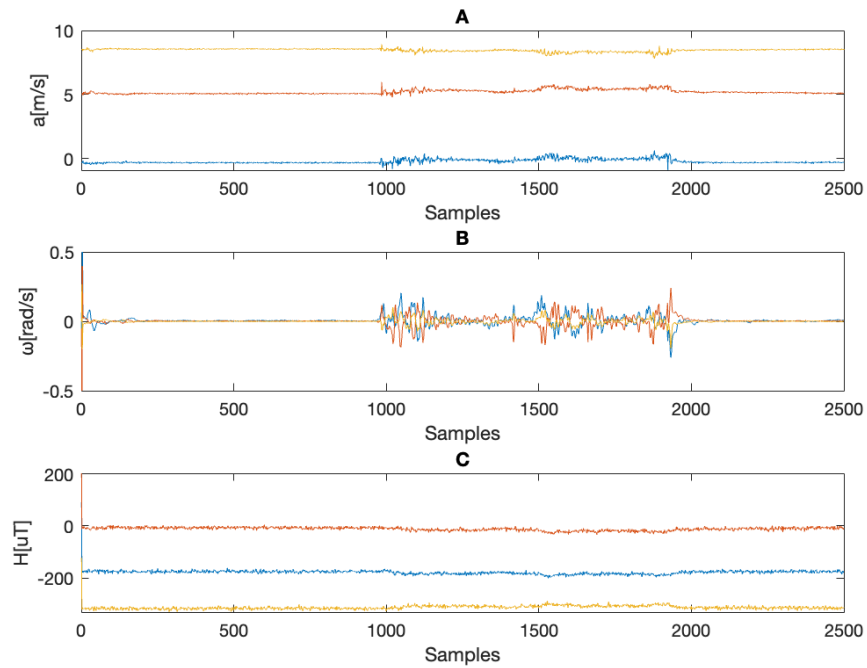


Figure 4.10: Signals for the Personalization acquisition for the right foot of subject 3. A) Accelerometer readings; B) Gyroscope readings; C) Magnetometer readings.

a predetermined set of markers to enable easier reconstruction using the NEXUS software. This facilitated the manual identification of events, streamlining the process.

ii) The sensors from the INDIP system were placed, which included two distance sensors on each leg, two magneto-inertial sensors on the feet and one on the pelvis, and two sensorized insoles with pressure sensors on the feet (estimated duration: 15 minutes). Anthropometric measurements were taken simultaneously to calibrate the VICON system model.

Next, the already mentioned calibration tests were carried out, and a quality check conducted.

In the Figure 4.12 is presented one subject instrumented before starting the acquisition.

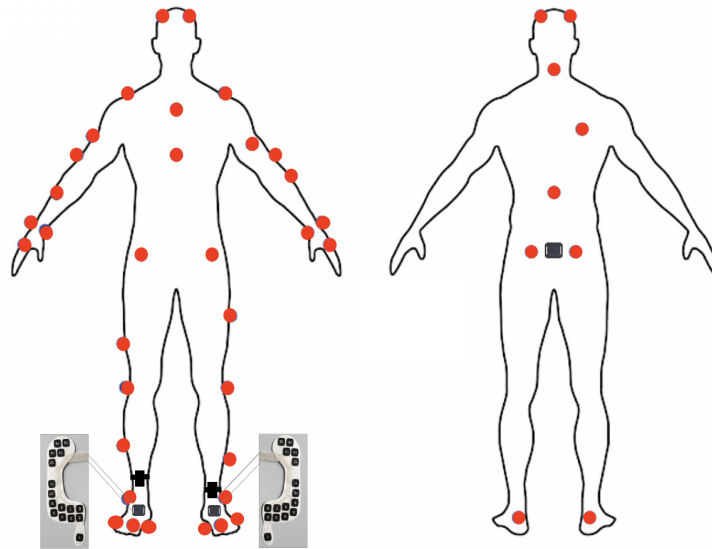


Figure 4.11: Representation of the subject instrumentation, vicon markers are red painted.

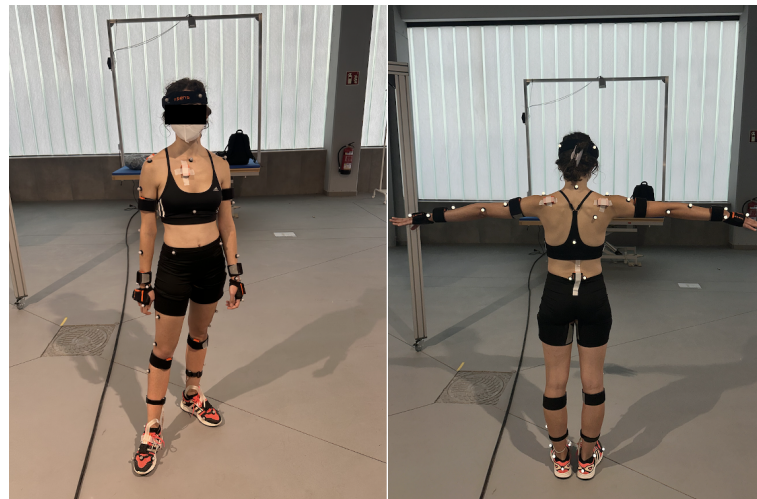


Figure 4.12: Experimental subject instrumentation.

4.7 Experimental Set Up

The initiation of all acquisitions in the Vicon system is done by connecting a trigger INDIP unit to the sync output connector of the Vicon Lock, as depicted in Figure 4.13. The acquisition process begins with the recording from the INDIP GUI via Bluetooth on the INDIP units. Subsequently, the Vicon recording is

initiated, which triggers the INDIP unit connected to the lock. Upon completion of the acquisition, the Vicon recording is stopped, followed by the cessation of the Bluetooth-connected INDIP units.

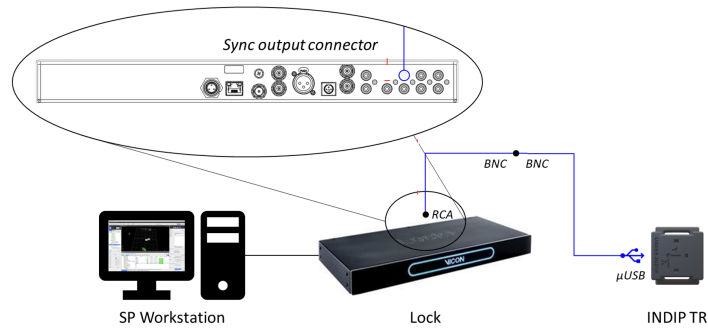


Figure 4.13: Experimental setup.

4.8 Data Preprocessing

4.8.1 Vicon Data Preprocessing and Organization.

The Vicon data is organized according to the EURO BENCH format [47] format which is presented in the Figure 4.14.

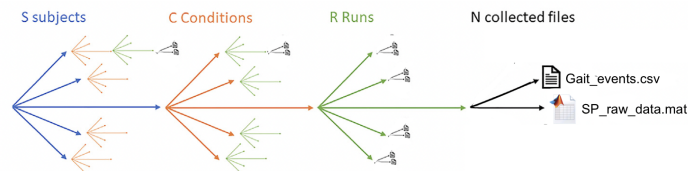


Figure 4.14: Data organization.

- The first output of the Nexus software is a CSV file with all the gait event information. Due to the irregularities of the surfaces, gait cycle segmentation for the reference system that consists in event identification was manually performed.
- The second output is a .mat file that contains all the marker trajectories. These trajectories are extracted to enable the calculation of spatio-temporal parameters.

4.8.2 INDIP Data Preprocessing and Organization

After completing all the Tests, the data recorded by each sensor are manually downloaded using the Matlab INDIP GUI. These data files are then saved as text files (TXT) into the Experimental Protocol folder within the corresponding Participant Folder. To organize and standardize the data, a Python code is employed. This code automatically reads the Excel table that was generated during the acquisition process and processes the corresponding TXT files. The TXT files are then saved as renamed files within the participant's designated folder. Furthermore, the automated organization process involves not only saving and organizing the data into a .mat structure but also interpolating the data from the INDIP units that were started using the GUI through Bluetooth. This interpolation is performed to synchronize the data based on the timestamps recorded by the trigger INDIP unit, which is connected to the VICON lock. The information in this arrangement is structured according to each individual, categorized by various types of environmental conditions. Within each category, you can locate individual trials or runs, with the sensor data divided into two parts: data obtained from distance sensors and pressure insoles, and data collected from the body's IMU for each body part. The standardized data is then saved as a Matlab structure (data.mat) into the corresponding Participant Folder. Finally, the data.mat structure serves as input to the collection of Matlab scripts and functions of the INDIP algorithm. These scripts and functions are designed to process the data and generate the desired output, which includes events and parameters related to the study. In order to increase the robustness of the INDIP system some algorithm modifications were implemented, which are discussed in the next chapter. The INDIP data is organized by also following the EURO BENCH format as seen in Figure 4.15.

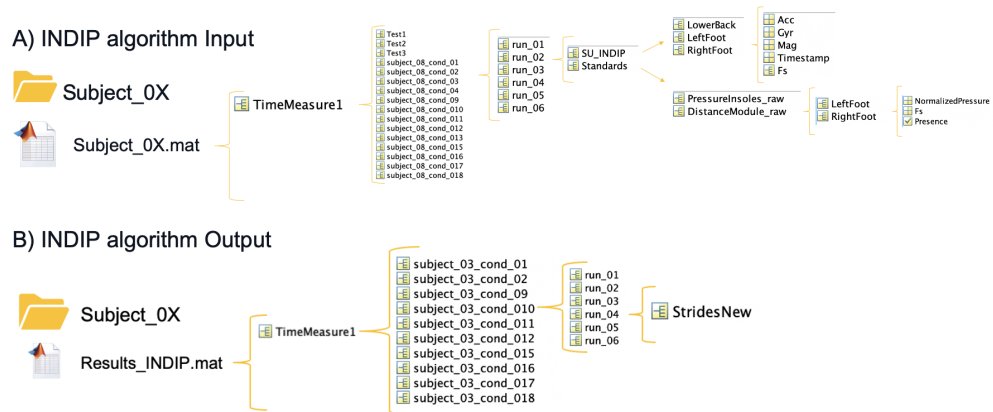


Figure 4.15: A) Input data organization for the INDIP algorithm, B) Output data organization from the INDIP algorithm.

StridesNew is a mat struct which contains:

- Initial Contact Events.
- Final Contact Events.
- ICFlags.
- FCFlags.
- Stride duration for each stride.
- Stride length for each stride.
- Stride clearance for each stride.
- Vertical displacement for each stride.
- Velocity for each stride.
- Foot Identification.

Chapter 5

Methods

This chapter delves into the detailed explanation of the algorithms utilized for processing the data acquired from the SP and INDIP systems. The data obtained from the Vicon system underwent both automated and manual processing within the system's software. The original algorithm of the INDIP system underwent a rigorous analysis and subsequent modifications. Consequently, this section exclusively highlights the specific components of the algorithm that were subjected to modification, while a comprehensive elucidation of the complete algorithm can be referenced in [6]. Additionally, the chapter concludes by presenting the respective metrics and methodologies employed for analyzing the processed data. These metrics and methods play a pivotal role in unraveling valuable insights from the collected dataset, ultimately contributing to a comprehensive understanding of gait dynamics in extreme terrain conditions.

5.1 Vicon Data Processing

To obtain the CSV output of the VICON system seen in Figure 4.14 where gait event information is contained, all trials are manually processed with Vicon Nexus. The complete pipeline is presented in Figure 5.1.

The first step involves importing the collected data into the software, where the markers are automatically reconstructed and labeled. If any data is missing, it is manually filled based on specific criteria. Then, the Dynamic Body Language Model is executed, and the trajectories are filtered using the Woltring filter. Afterward, the Dinamic Plug in Gait Model is applied to the processed data. During this process, events like Initial Contact (IC) and Final Contact (FC) are manually identified, considering a mean value between 10 and 12 gait cycles per trial, and 4 trials processed for each subject, at the end 4000 gait cycles were manually processed in the Vicon software, the FlowChart related to the event identification

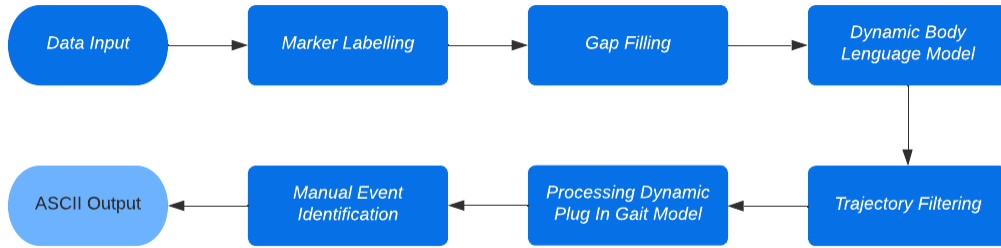


Figure 5.1: Vicon Processing Pipeline.

is presented in Figure 5.2. To accurately identify FC, the trajectory of the TOE marker and two additional markers placed in each side of the foot are evaluated using the software graphic interface. Similarly, the trajectory of the HEE marker is analyzed to identify IC, an example of this can be seen in Figure 5.3. These markers were selected based on their placement near the heel and toe regions of the foot, as these areas make initial contact with the ground and lift off from it, respectively. Additionally, to improve identification and minimize human error, the terrain structures are reconstructed in the software using terrain marker positioning (Figure 5.4). This enables the reconstruction of irregularities and the precise identification of the moment when the trajectory makes contact with the terrain. Finally, the events are exported in ASCII format, specifically as a CSV file that contains comprehensive event information.

As it has already said, the second output seen in Figure 4.14 contains the trajectories of the markers that are used for obtaining spatio-temporal parameters. In order to obtain them, the mean value between the trajectory of the TOE marker and the trajectory of the HEE marker is computed. This is necessary because no marker was placed on the INDIP system, so an approximate point is considered instead. Subsequently, the manually identified event instances from the Nexus software are imported, and these trajectories are segmented to estimate spatial parameters such as stride length. In Figure 5.5 an example of the anteroposterior trajectory with the respective IC is presented for each foot.

5.2 INDIP Data Processing and Algorithm Optimization

In order to enhance the INDIP robustness for characterizing gait in extreme terrains conditions some algorithm adaptations were conducted. The existing algorithms needed to be refined to account for the unique challenges posed by such terrains,

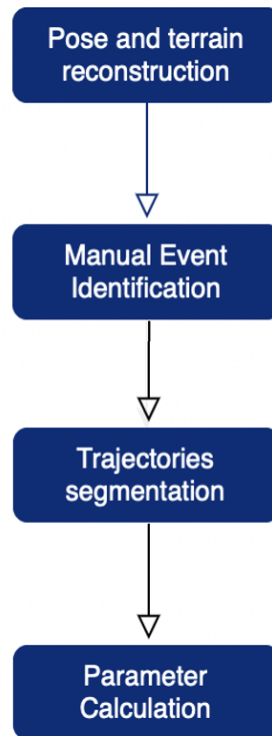


Figure 5.2: Flow Chart related to the manually event identification in Vicon.

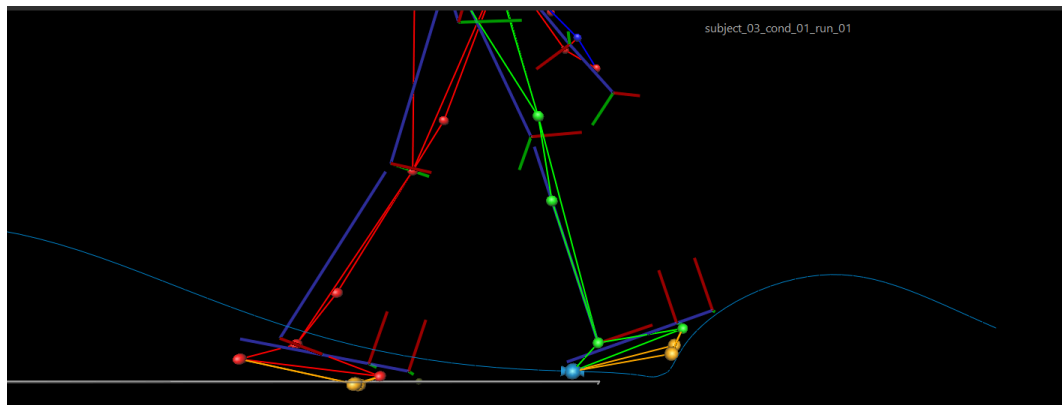


Figure 5.3: Marker trajectory in Nexus Software.

ensuring accurate and reliable gait analysis. The goal was to accurately capture and analyze gait patterns despite the unique challenges posed by these terrains.

Refinement of the algorithms was a key aspect of the modification process. Advanced signal processing techniques were developed and applied to effectively handle the dynamic nature of extreme terrains. This involved filtering the sensor

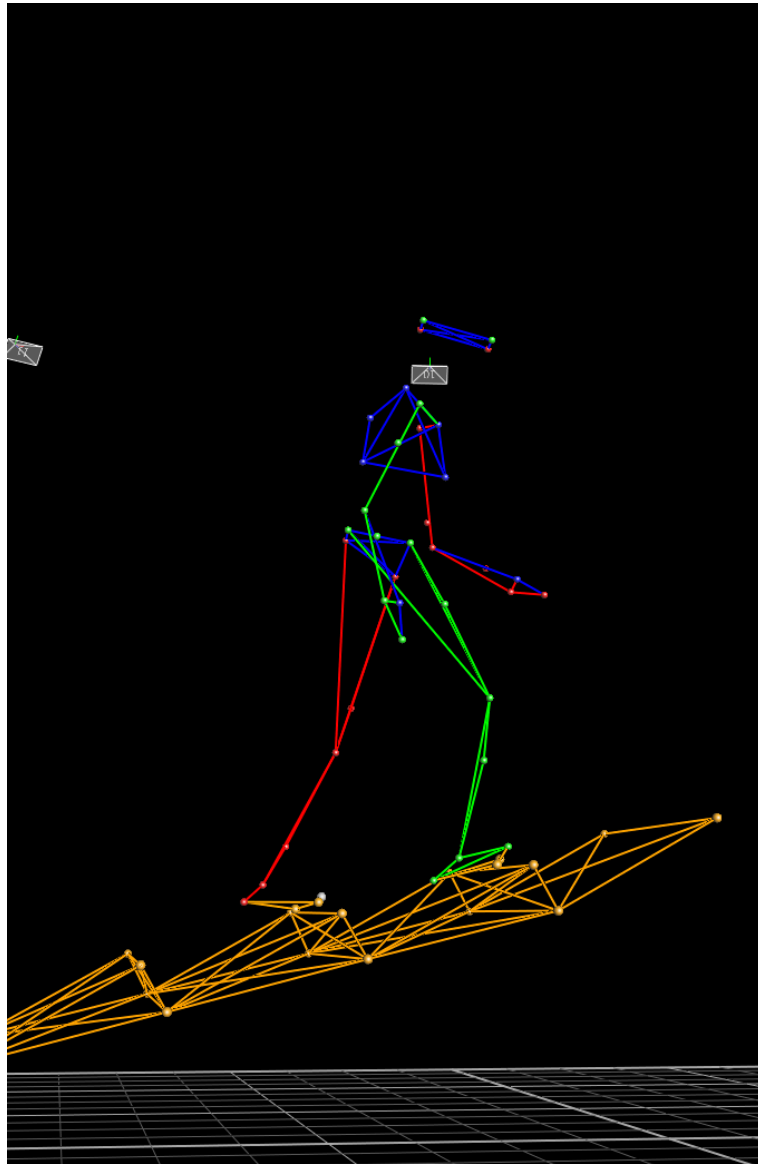


Figure 5.4: Nexus visualization of the reconstructed pose and terrain.

data and extracting relevant gait information while mitigating noise, artifacts, and motion interference arising from the challenging terrain conditions. The validation phase involved comparing the results obtained from both the original and modified algorithms to analyze the algorithm's improvement. This chapter solely focuses on presenting the modified methods, while the discussion of the results is reserved for the nexts chapters.

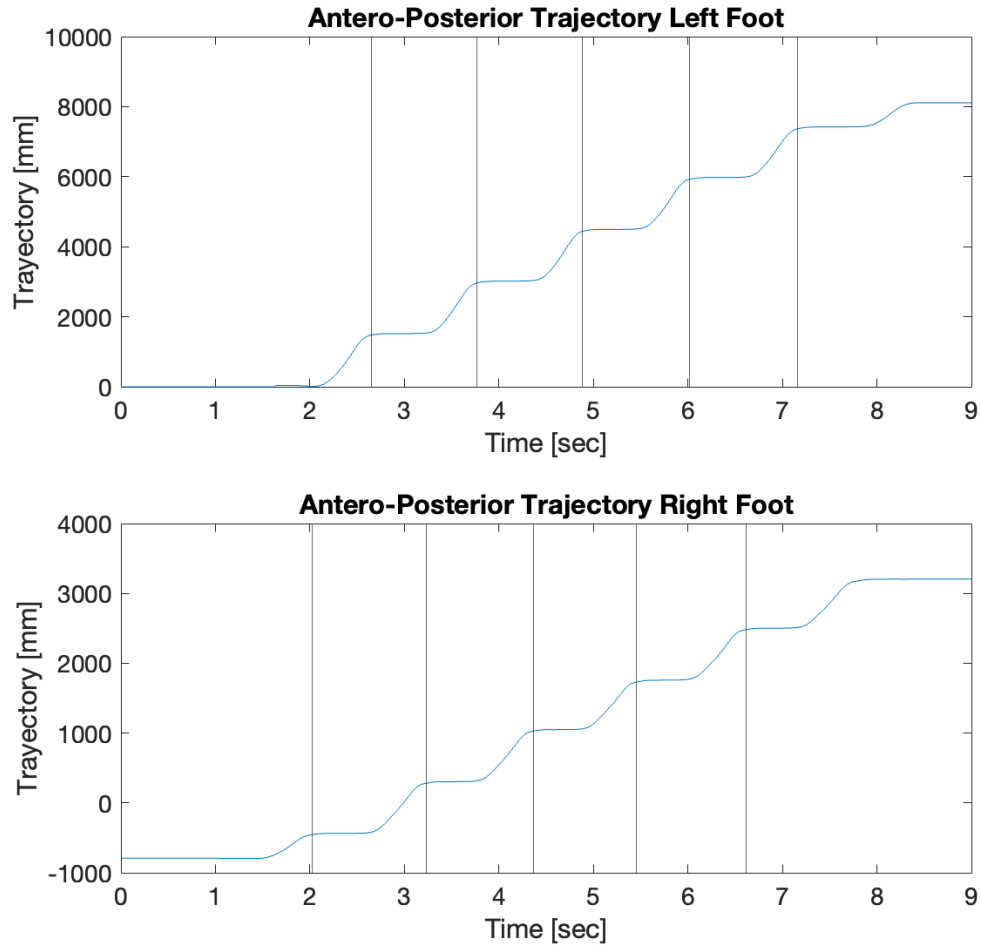


Figure 5.5: Left and Right Foot Antero-Posterior Trajectory from Vicon with IC identified.

5.2.1 Automatization of Personalization Phase

The original INDIP algorithm incorporates a function for obtaining quality flags from the data personalized acquisition explained in the preceding chapter. This function was designed to establish intervals for the Standing, Fly, and Personalization Phases based on the total standard deviation of each foot. Ideally, two time points were derived for each phase to indicate their respective beginnings and ends. However, due to noise or subject movement, the algorithm sometimes identified more than three phases, necessitating manual intervention by the operator. To optimize this function and minimize operator input, a verification process

was implemented after identifying the phase intervals. This check calculates the time differences between all phases and determines their minimum and maximum values. If a minimum difference exists after the third index, it is eliminated as it is likely a mistake since no phase should follow the third phase, which is the largest one. An example of this issue is illustrated in Figure 5.6, where a small interval was erroneously considered, causing the algorithm to crash. Following the aforementioned implementation, this problematic interval was disregarded, ensuring improved algorithm performance and stability.

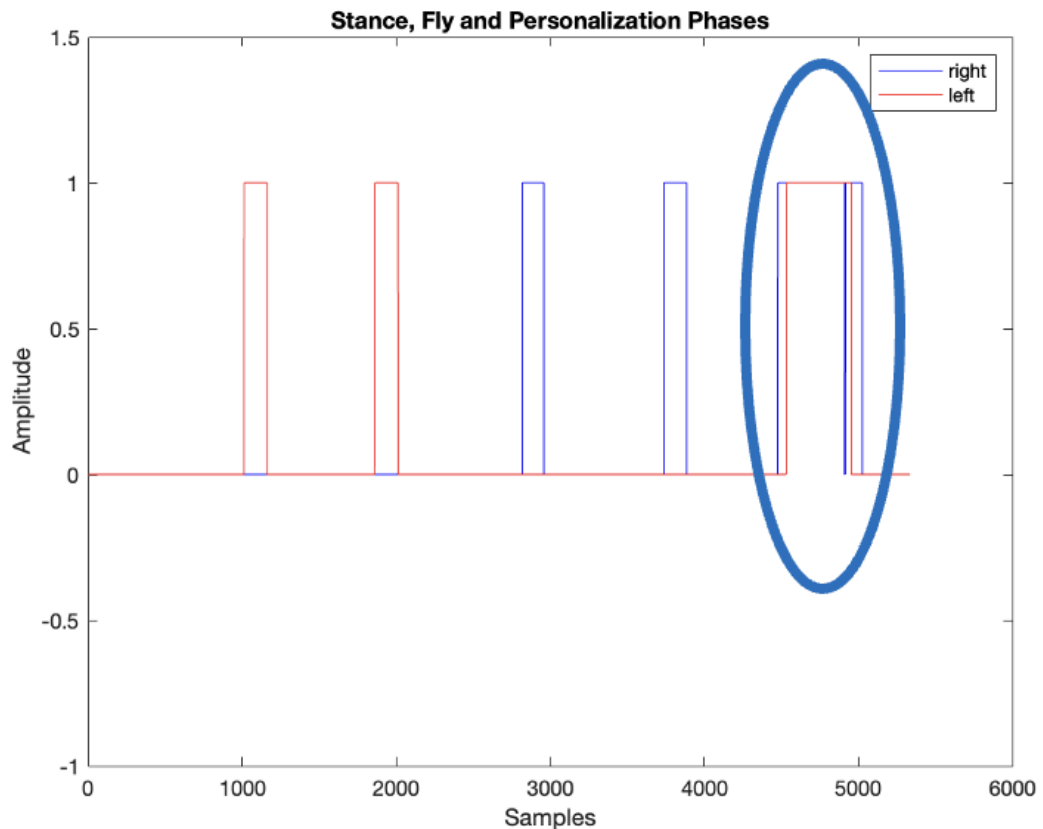


Figure 5.6: Stance, Fly and Personalisation problem identification.

Furthermore, changes were made to the threshold for finding high right and left foot motion to define the flags of each foot. Firstly, a constant value was used as threshold and this has been changed for a percentage of the maximum value. Additionally, modifications were made to the definition of trusted swing and stance phases when obtaining the dynamic flag. Originally, a constant number was used, which the operator adjusted for each subject. The stance phase is now defined as

the portion of the signal that is higher than 60% of the maximum value from the mean between all PI signals, while the swing phase is defined as the portion of the signal smaller than 35% of the mean between all PI signals. This last change was made to avoid algorithm crashes when signals were not intense enough to reach a constant number, an example of this case is shown in Figure 5.7, where the swing phase was previously defined with a threshold of 0.6, in this case, the mean signal it does not arrive to that amplitude.

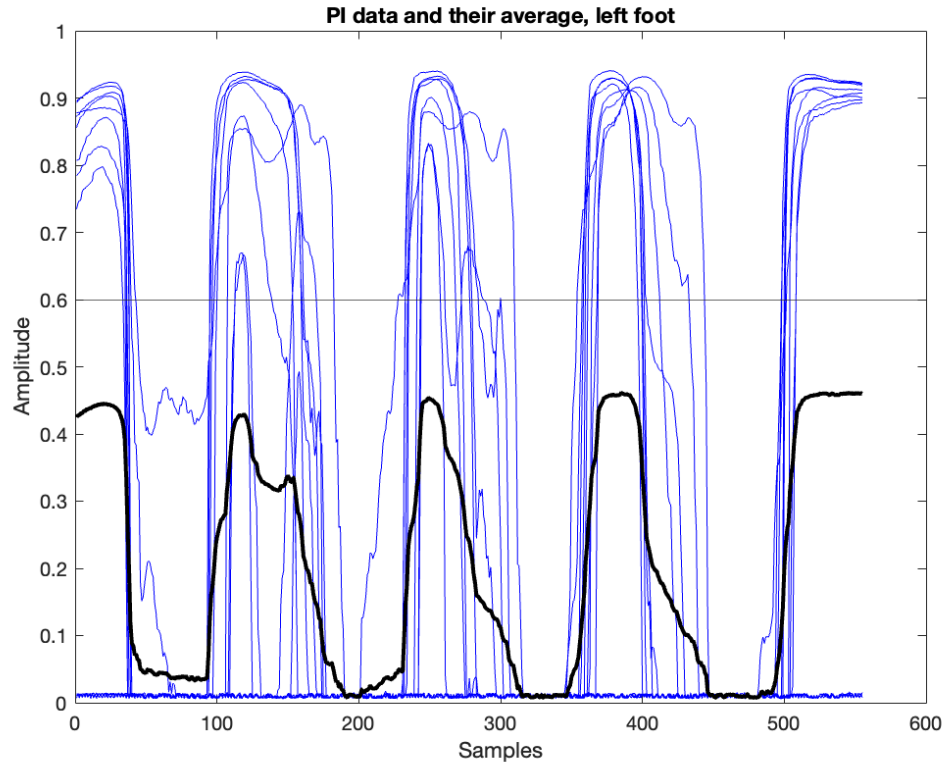


Figure 5.7: Problem of using a constant treshold for defining Stance Phase.

5.2.2 PI signal quality enhancement for improving event identification.

An illustration of a PI signal during normal walking is depicted in Figure 5.8. The figure displays the plotted signals from 16 sensors positioned on the insole. The swing phase, characterized by the absence of sensor activity, is clearly visible. Conversely, during the stance phase, the pressure exerted by the foot activates different sensors, resulting in their active state.

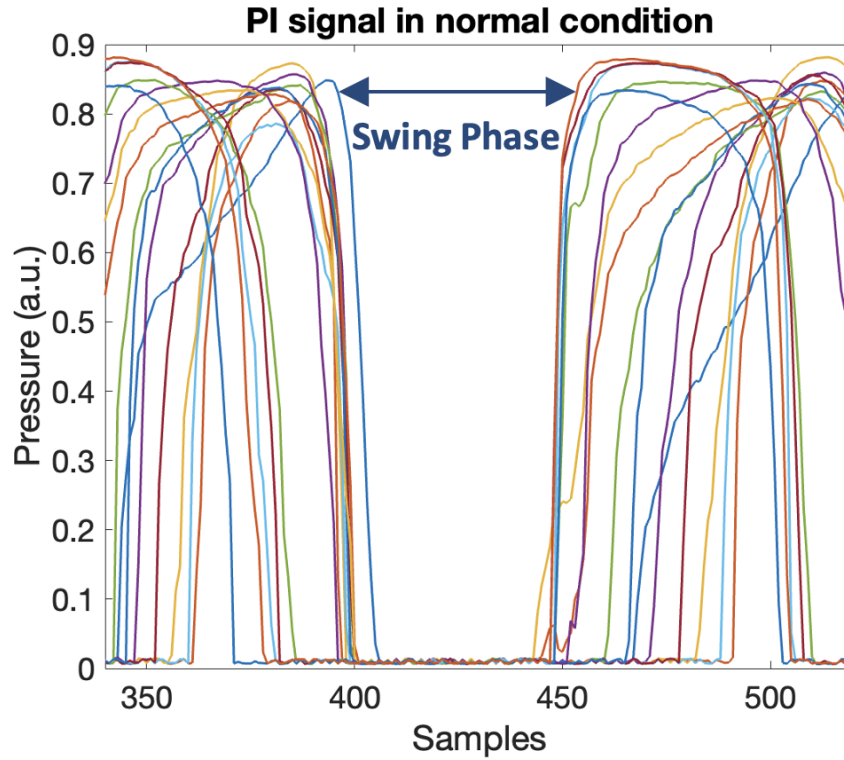


Figure 5.8: PI signal in normal walking condition.

A possible assumption is that surface irregularities can have an impact on the quality and accuracy of pressure insole measurements. When pressure insoles are used to analyze gait or assess foot pressure distribution, they rely on the assumption that the foot maintains consistent contact with the surface. However, in the presence of surface irregularities, such as depressions, or uneven terrain, this assumption could be challenged [48].

Surface irregularities can disrupt the normal distribution of pressure across the foot [48], leading to inaccurate measurements. For example, when encountering a bump or uneven surface, the pressure insole may register higher pressure readings in certain areas of the foot, even if the actual pressure applied by the foot is relatively low. Conversely, when walking over a depression or uneven terrain, the pressure insole may fail to detect or register adequate pressure in specific regions of the foot.

These discrepancies in pressure readings can possibly impact the quality of the data obtained from the pressure insoles. They can introduce noise and inconsistencies into the measurements, making it difficult to interpret and analyze the data accurately.

After checking some of the signals and results obtained with the original algorithm it was possible to realize that in some subjects the quality of the PI signals

was poor, increasing the time differences between INDIP and VICON results. In Figure 5.9, an example of the PI signal under extreme terrain conditions is shown. In this particular case, it can be observed that certain sensors remain active during the swing phase, suggesting that the foot is applying some pressure. However, according to the conventional definition of the swing phase, this should not be possible. This discrepancy in sensor activation during the swing phase can potentially result in misidentification of gait events. Therefore, it is crucial to minimize sensor activation during the swing phase to ensure accurate event detection.

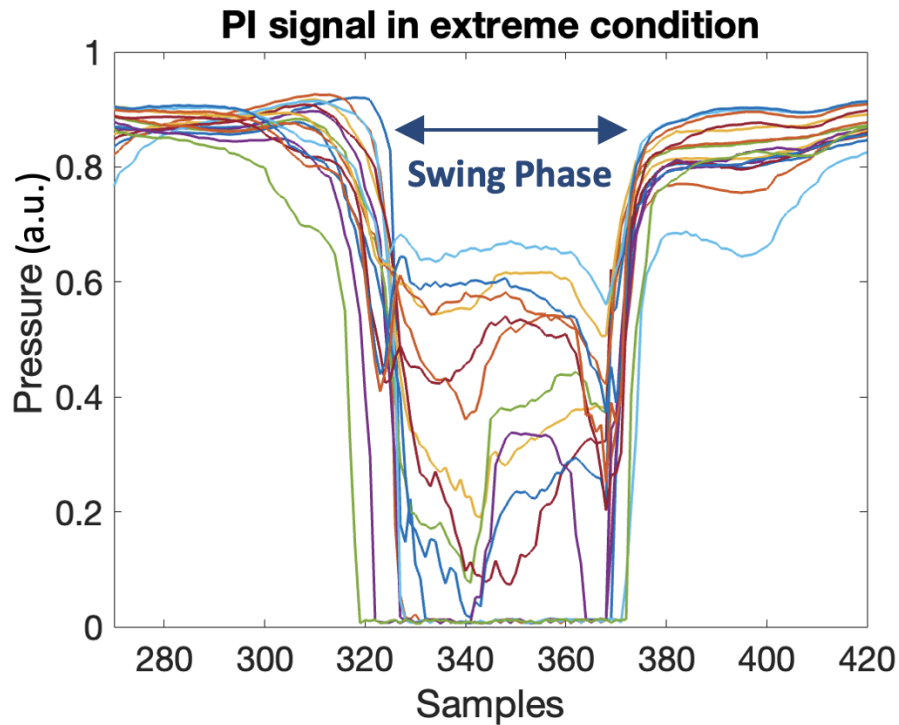


Figure 5.9: PI signal in extreme terrain walking condition.

With the purpose to increase the quality of the signals and reduce the time difference error between INDIP and VICON firstly the sensors were classified in two groups:

- False Positive Active sensors (FPAS): sensors that present signals that are active when they should be disabled, for example, in swing phase.
- True Positive Active sensors (TPAS): sensors that present signals that are disabled when they should be disabled, for example, in swing phase.

This classification was obtained by computing the correlation between the 16 sensors of the PI. Correlation is a measure of the degree to which two signals or

datasets are related to each other. It measures the similarity between two signals and indicates how much they vary together [49]. Considering two discrete-time signals $x[n]$ and $y[n]$ which are signals for two different sensors of the PI, the $C(x, y)$ correlation between them is defined as:

$$C(x, y) = \sum_{n=n_1}^{n_2} x[n]y[n] \quad (5.1)$$

where n_1 and n_2 define the interval over which we are calculating the correlation. In words, to compute a correlation between two signals, they are multiplied together and then added up the product. This gives a single number that represents how similar the signals are to each other. Considering this, the idea is to use the correlation to put signals which has a undesired activation together and separate them from those which are correctly activated. The correlation matrix between all sensors is represented in a heat map and shown in Figure 5.10.

First, a column mean is performed to obtain a single correlation value for each sensor related to the others, then, a second average is carry out to compute a unique threshold for separating between false positive sensors and true positive sensors. Experimental results shown that those sensors which have a correlation value higher than the threshold are the ones which are considered false positive sensors. An example of these groups is shown in Figure 5.11.

Once sensors were classified the general aim is to reduce the active part of the signal in the swing phase to a number close to zero. To do this the mean of these sensors is computed and multiplied for each signal of the false positive sensor. Figure ?? illustrates the calculated mean signal derived from all the falsely positive active sensors. Additionally, Figure 5.13 demonstrates the outcome of multiplying this mean signal with each of the falsely positive sensors.

Subsequently, a sigmoid function is applied for each sensor's signal for preserving the peaks and deepens the valleys [50]. Applying a sigmoid function to pressure insole signals can have several advantages such as:

- **Non-linearity:** The sigmoid function is non-linear, which means that it can capture complex relationships between the input and output signals [51]. In the context of pressure insole signals, this can help to capture more nuanced changes in pressure over time.
- **Improved interpretability:** The sigmoid function can normalize the output values to a range between 0 and 1, which can make it easier to interpret the data. For example, if the pressure insole signals are being used to measure the gait of a person, the sigmoid function can provide a normalized output that can be more easily interpreted by a clinician or researcher.

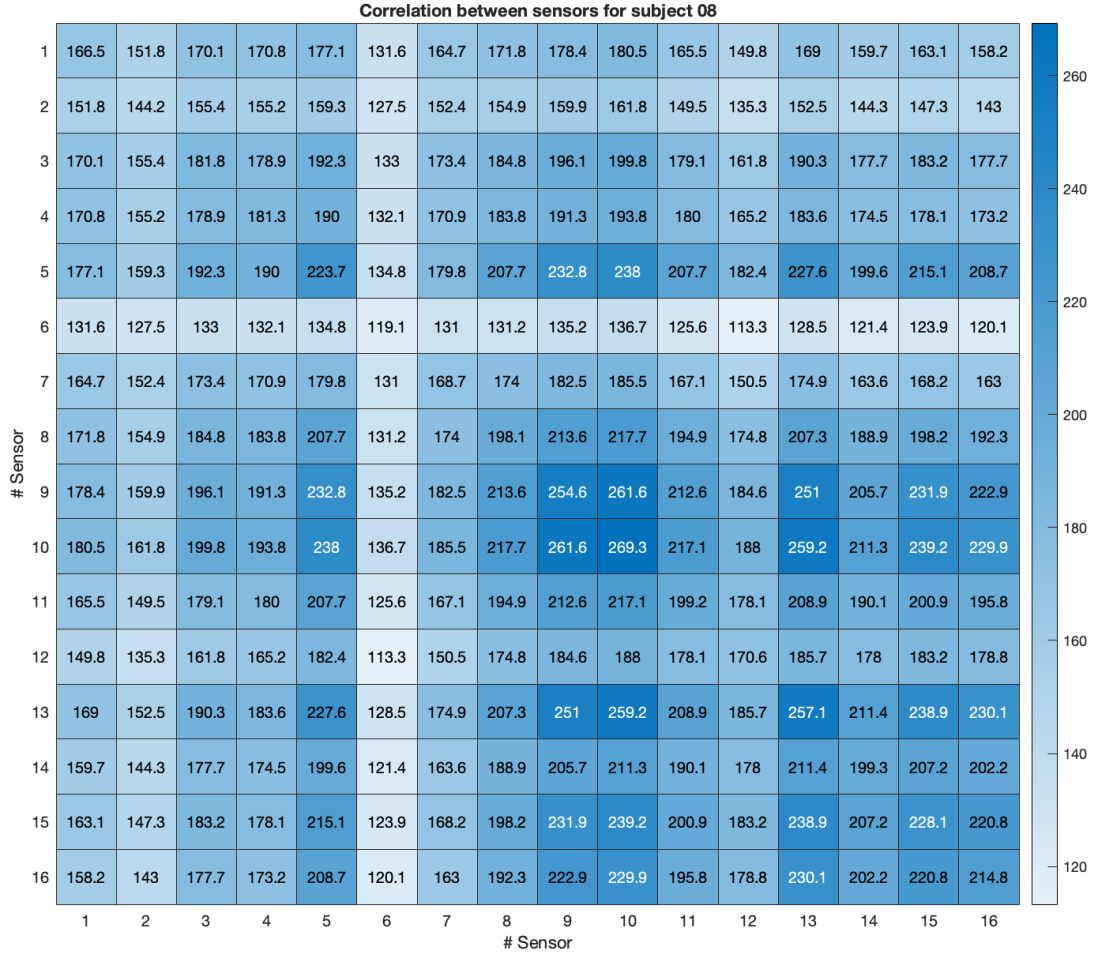


Figure 5.10: Correlation Heatmap between sensors.

- Noise reduction: The sigmoid function can smooth out noise in the input signal by compressing extreme values towards the center of the sigmoid function [52]. This can help to reduce the impact of random fluctuations in the data and make it easier to identify patterns and trends.

Overall, applying a sigmoid function to pressure insole signals can help to improve the interpretability and usefulness of the data, while also providing a non-linear approach to analyzing the data. Mathematically the sigmoid signal is defined as 5.2:

$$x_{new} = \frac{1}{1 + e^{-\phi \cdot x}} \tag{5.2}$$

In this equation, ϕ represents the output of the sigmoid function for a given

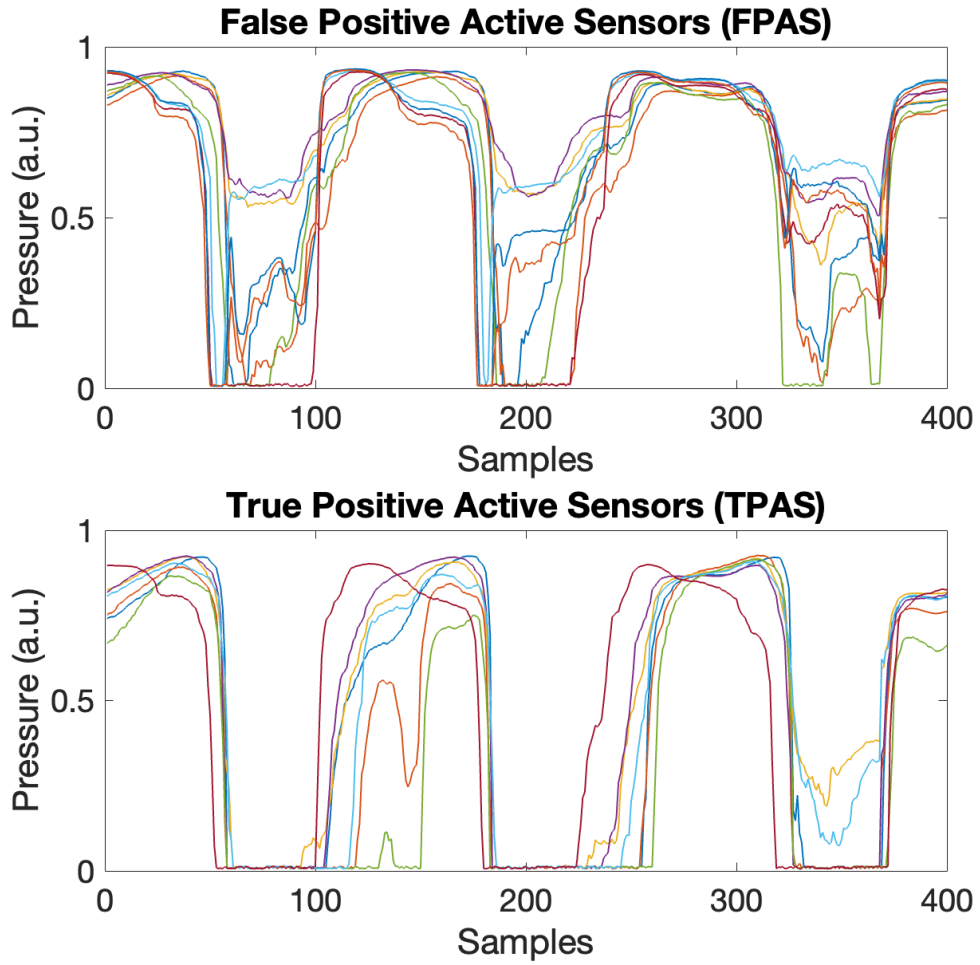


Figure 5.11: False positive sensors and true positive sensors classification.

input value x , which is the PI signal, and ϕ determines the slope of the sigmoid curve. Increasing the value of ϕ makes the curve steeper, while decreasing the value of ϕ flattens the curve.

With $\phi = 0.05$, x the PI signal to which is applied the sigmoid function and x_{new} the modified PI signal, the applied function with its coefficient is presented in Figure 5.14.

It is necessary to mention that this function is applied to the "False positive" sensor's signals after the mean correction as well as to the "True positive" sensors in order to enhance the general quality of the signals. As a result, there is not only a clearly quality improvements of the PI signals as seen in Figure 5.15 but also a reduction of the mean absolute difference respect to those events find with the Vicon system.

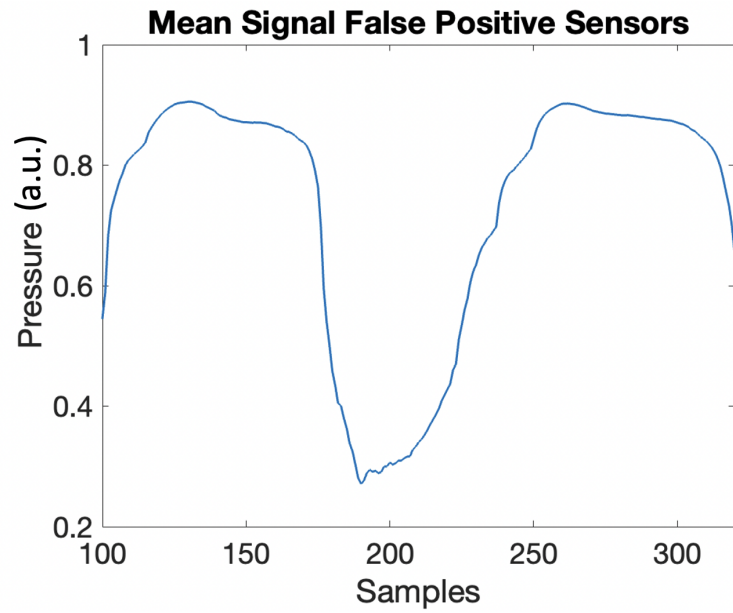


Figure 5.12: Mean FPAS Signal.

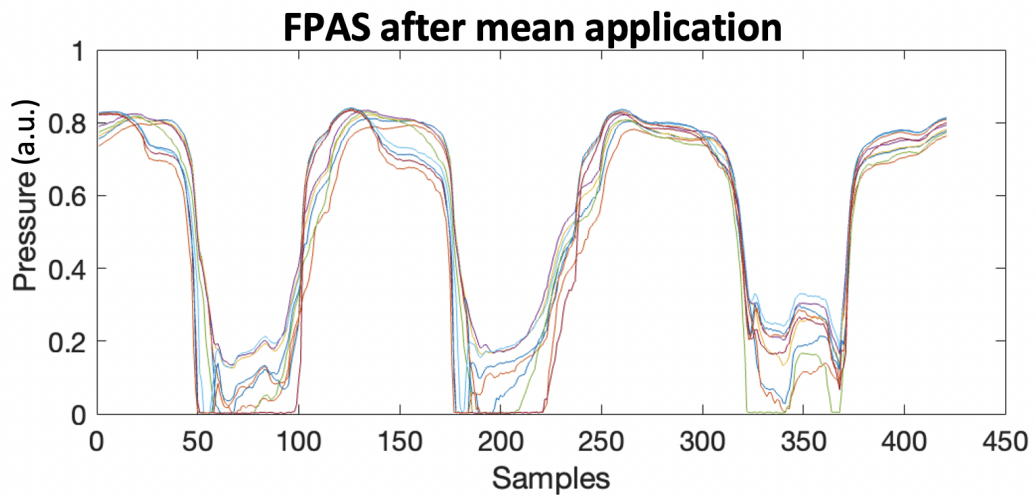


Figure 5.13: False positive active sensors after mean multiplication.

5.2.3 Rising and Falling edge new criteria

To obtain potential IC and FC instants, the INDIP algorithm detects minimum values associated with the ascending and descending segments of the PI signals. The algorithm operates on the principle that the IC corresponds to the minimum value preceding a rise in the signal, whereas the FC is determined as the minimum

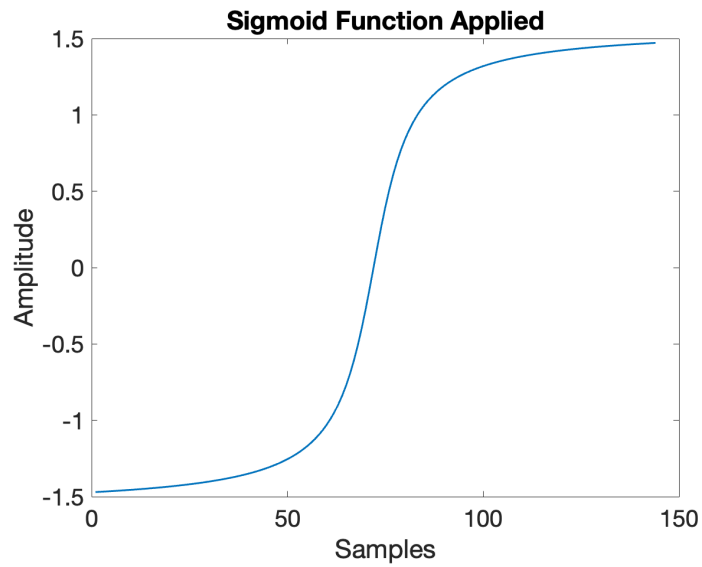


Figure 5.14: Applied sigmoid function with $\phi = 0.05$.

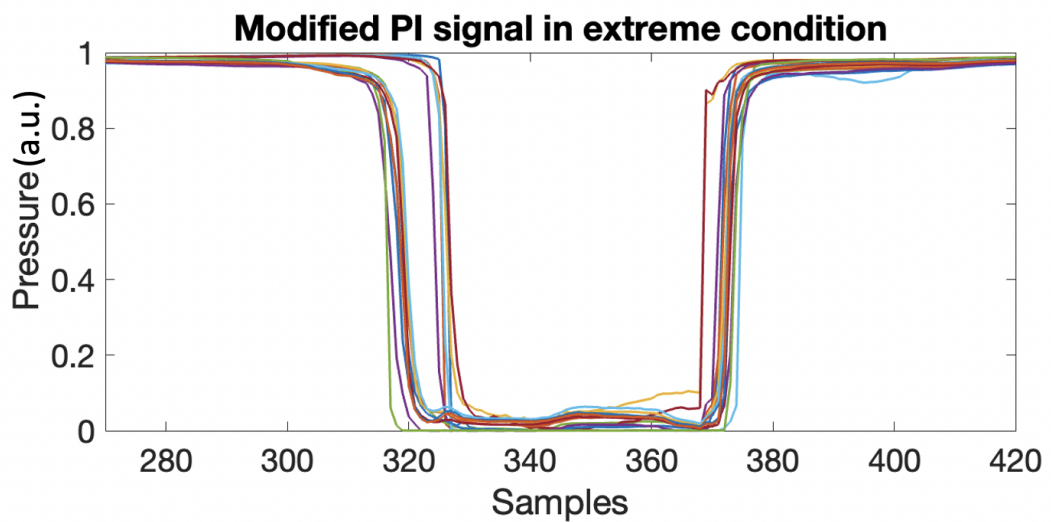


Figure 5.15: PI signals after sigmoid application.

value prior to a decline in the signal. This procedure entails calculating the first derivative of the signal and identifying the peaks as the rising and falling edges, respectively. By employing this approach, the algorithm effectively identifies the specific points in the PI signals that correspond to the IC and FC events during gait analysis.

Once the initial IC and FC are identified, a verification step is carried out to

discard insignificant rising and falling edges using two criteria. The first criterion involves analyzing the amplitude reached by the signal within a specific window, based on two conditions: the length of the window and the threshold for the amplitude. The second criterion considers the time interval between consecutive falling edges.

In Figure 5.16, the Final Contacts (FC) for one channel of the pressure insole sensor are shown. These FC points were determined by identifying the falling edge using the Original Algorithm. The preliminary FC points are indicated by the red markings, following the applied criteria.

It becomes evident that the original criteria and conditions are not effectively capturing the characteristics of the signal. This discrepancy arises from visually observing the signal, where the expected FC falling edges should transition from an amplitude close to one to a small value close to zero.

However, it is noticeable that certain falling edges with amplitudes smaller than one are incorrectly identified as definitive FC. This misidentification can have adverse effects, including impacting the accurate detection of true FC, as evidenced by the FC around 400 samples. Although lacking the red marking, it is clear that this is a valid FC. Additionally, the duration between consecutive falling edges is not accurately represented, and it is apparent that the first two FC, for example, are in close proximity to each other.

To address the issues with automatic identification, three procedures were implemented. Firstly, the window values for the first condition of the first criteria and the second condition of the first criteria were adjusted to 15 and 35 samples, respectively. Secondly, the amplitude thresholds for the first condition of the first criteria and the second condition of the first criteria were modified to 0.5 and 0.8, respectively. These threshold values were determined through experimental adjustments to ensure effectiveness across most channels.

Additionally, a second condition was introduced for the second criteria, which utilizes the derivative signal of the PI signal. Prior to applying the sigmoid method, the signals were not constrained within the range of zero to one. Consequently, the derivative signal exhibited inhomogeneity, with falling and rising edges being represented with varying amplitudes. However, after applying the sigmoid method, which possesses normalization properties, the signal is scaled between zero and one. This enables a steeper slope in the derivative signal when falling and rising edges occur in the original signal.

Considering this, a criterion was established that identifies proper FC based on the derivative value of the falling edge, requiring it to exceed 60% of the maximum value of the derivative signal. In Figure 5.17 is possible to appreciate that after the new conditions and criteria applied, the right FC were finally obtained.

It is important to clarify that this condition was exclusively applied to the falling edge check. In the case of the rising edge check, it was not necessary to implement

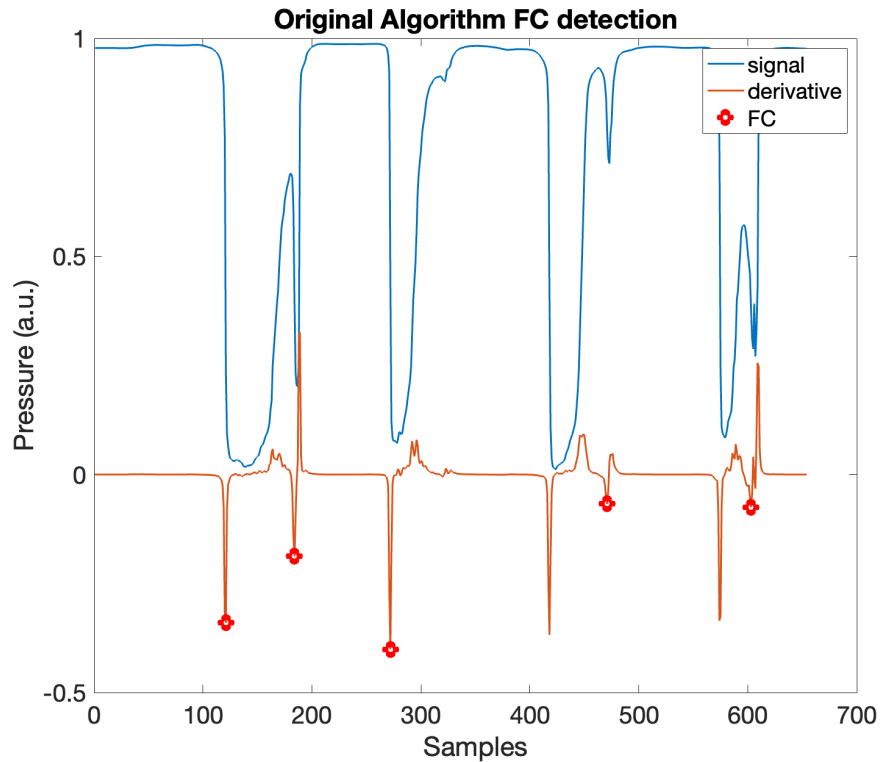


Figure 5.16: FC Candidates with the Original algorithm.

this condition since the slope of the curve is not as steep, and the original thresholds functioned effectively. This procedure was implemented to improve the accuracy of event identification in each channel, with the goal of achieving a more consistent identification across all channels. The objective was to identify sensors that belong to the same neighborhood and exhibit similar event patterns. By identifying closer candidate sensors within the same neighborhood, the overall event identification could be enhanced, resulting in more accurate results.

5.2.4 IC and FC selection refinement

After identifying events for each sensor, a neighborhood of active sensors is established for each sensor that has detected an event. A tern for each IC and FC events is found, composed by the respective rising or falling edge instant values, rising or falling minima and the three active sensors that belong to the same neighborhood and have registered those instants. Figure 5.18 displays all the potential events detected by each sensor in the pressure insoles for one complete gait cycle. Each event corresponds to an active sensor.

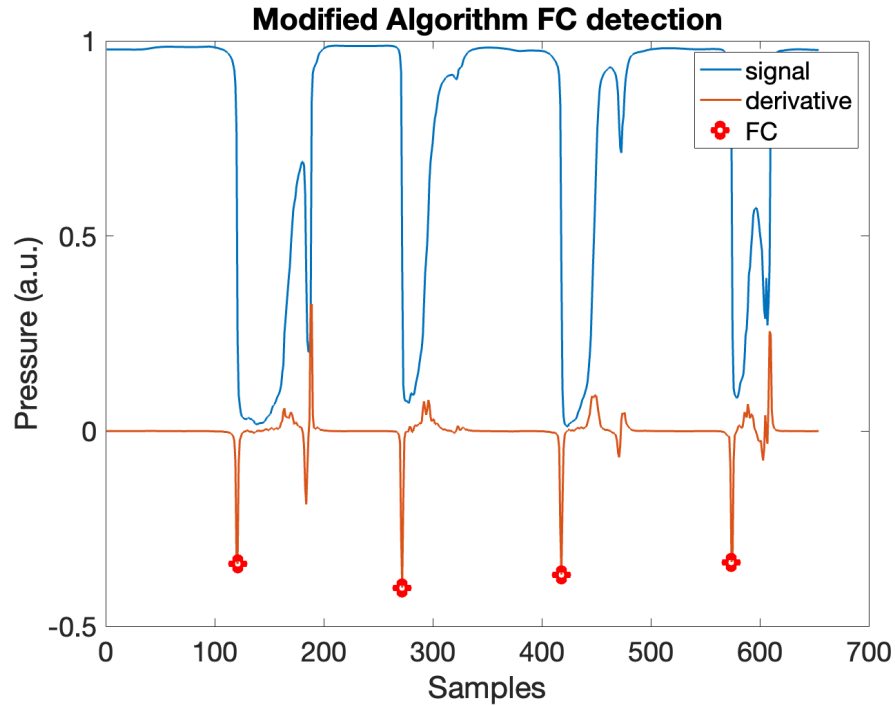


Figure 5.17: FC Candidates with the new criteria.

To identify the active sensors, the event detected by the first sensor is chosen as a candidate event, either IC or FC. The neighboring events detected by other sensors are considered as additional potential candidates. Consequently, three final candidates for each type of event are obtained by considering the events found by the sensor's neighborhood. It is important to highlight that the original code identifies the candidates sensors as those belonging to the same neighborhood to the first active sensor, without establishing any criteria. At the end an IC or FC candidate cell with 3 candidates for each active group is obtained. The candidate selection respect to the active sensors of Figure 5.18 is presented in Figure 5.19.

By examining Figure 5.18, it is evident that the active groups of FC and IC are widely dispersed across the falling and rising edges. This variability could be attributed to the signal fluctuations. One possible assumption is that the most accurate IC and FC are the ones that are closest to the majority of rising and falling edges observed across all channels.

In Figure 5.19, the candidates identified using the original code are displayed. It is distinct that some candidates are not well considered, as can be observed from various factors. Firstly, there are instances where the temporal distance between IC and FC is too short, indicating that some candidates from both groups are too closely positioned. Moreover, certain candidates within the same group are

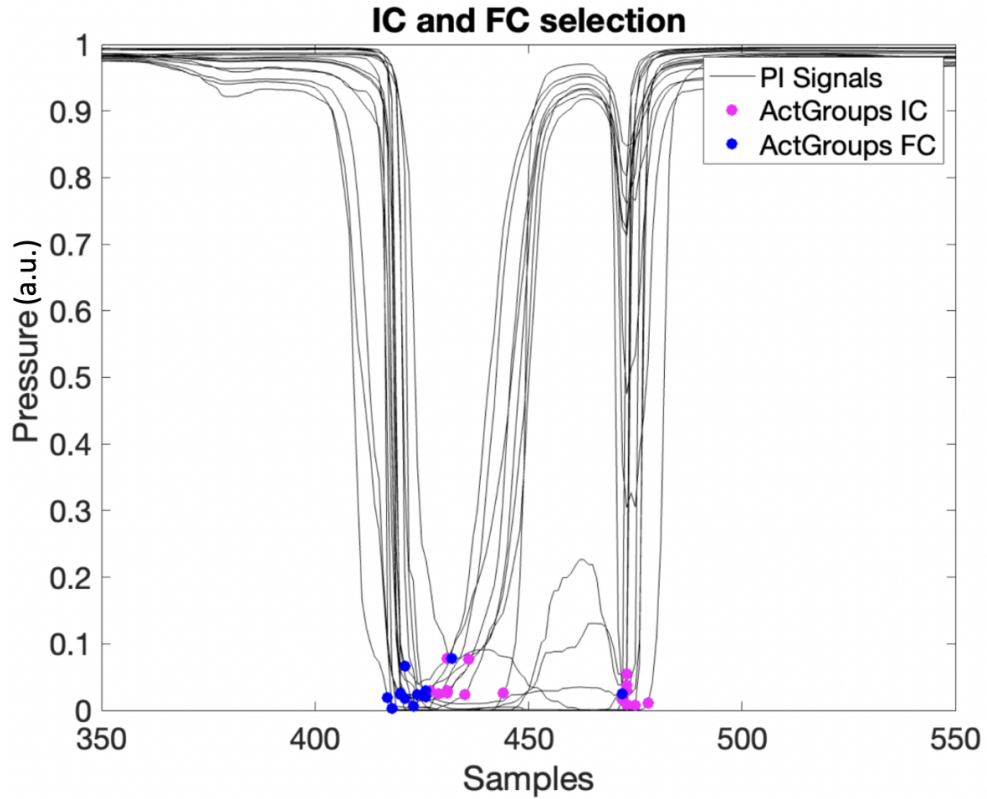


Figure 5.18: IC and FC found by each pressure sensor.

widely spread and exhibit significant temporal differences, implying that active sensors in the same neighborhood have detected different time instances of the respective events. The unsatisfactory outcome can be attributed to the absence of a criterion for selecting candidates from the active sensors. As previously mentioned, the original code operates by sequentially examining the neighborhood of the active sensors in increasing order. This approach lacks a systematic criteria for determining which candidates should be considered, leading to suboptimal results.

To address the issue and improve the selection of candidates based on the previously discussed assumptions, an additional algorithmic change was implemented. Instead of solely considering the first active sensor and its neighborhood, a new criterion was introduced that takes into account the concept of high density of active sensors. This criterion emphasizes the need for candidates to be located around areas with a higher concentration of active sensors.

The updated approach can be statistically translated into selecting the mode, which can be seen in Equation 5.3, among all events as the initial candidate. Subsequently, the neighborhood of this candidate is carefully evaluated to refine the final selection.

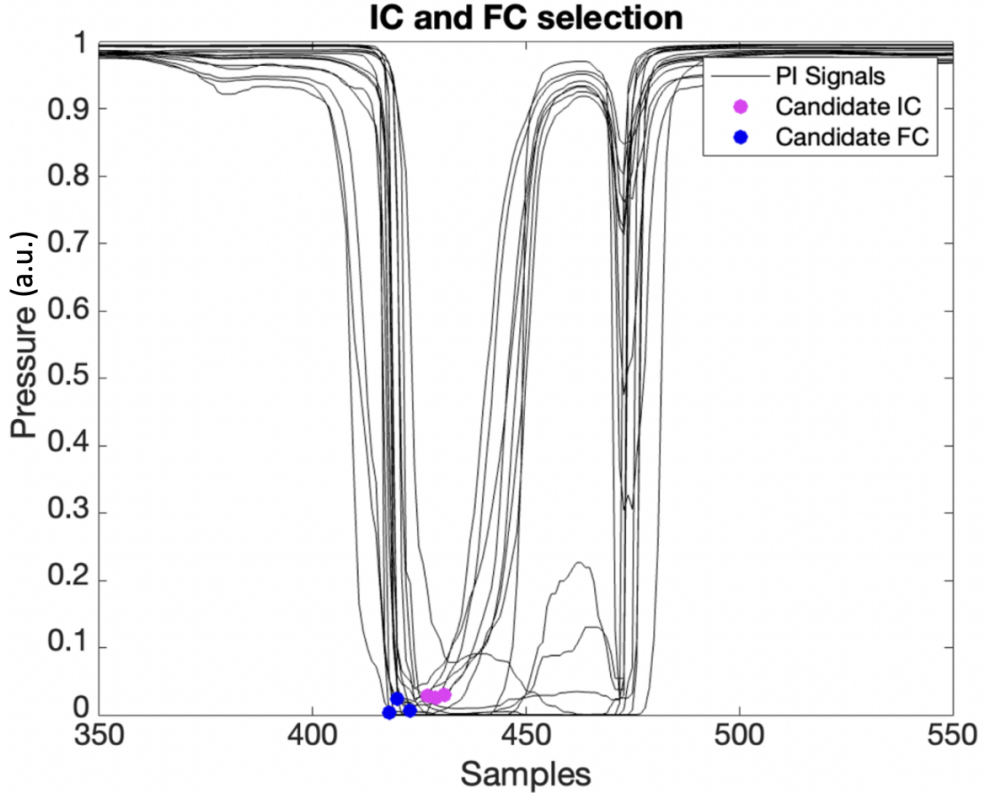


Figure 5.19: IC and FC candidates found with the original algorithm.

$$mode = L + h \frac{(f_m - f_1)}{(f_m - f_1) + (f_m - f_2)} \quad (5.3)$$

Where L is the lower limit of the modal class, h is the size of the class interval, representing the number of active sensors, f_m is the frequency of the modal class, f_1 is the frequency of the class that comes just before the modal class, f_2 is the frequency of the class that comes just after the modal class.

It is important to mention that if the mode of the active sensors does not have any active sensors in its immediate neighborhood, the closest value to this mode is considered as the first active sensor. This process continues until a group of active sensors belonging to the same neighborhood is identified. This ensures that even if the mode itself is not an active sensor, the algorithm searches for the closest value that represents an active sensor and then proceeds to find other active sensors in the vicinity to form a cohesive group.

The resulting candidates are presented in Figure 5.20. It is evident that the chosen candidates are not only closer to each other with increased homogeneity but also in closer proximity to the prominent falling and rising edges observed in

the signal. Additionally, it can be observed that there is a more distinct separation between IC and FC events, indicating improved accuracy compared to the previous case.

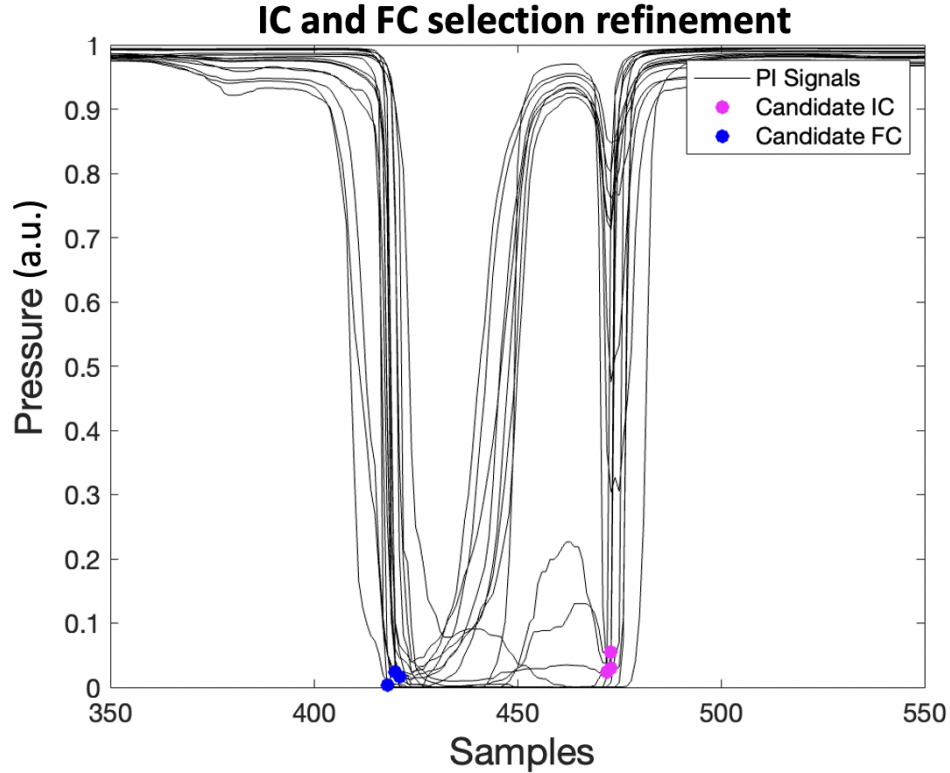


Figure 5.20: IC and FC candidates after applying the high density criteria.

5.3 Equally weighted PI and IMU event identification contribution

In the original algorithm, under normal overground walking conditions, if an event is detected by both PI and IMU systems from INDIP, the PI temporal value is defined as the right time instant if the difference between the two values falls below a predefined threshold. However, if the difference exceeds the threshold, a mean value is computed. This is done because the PI signals give direct information of the instant in which the foot touches or leaves the ground, a flowchart of the process can be seen in Figure 5.21.

Due to the already mentioned degradation in the quality of the PI signals, the reliability of PI as a gold standard in this particular case is questionable. Given

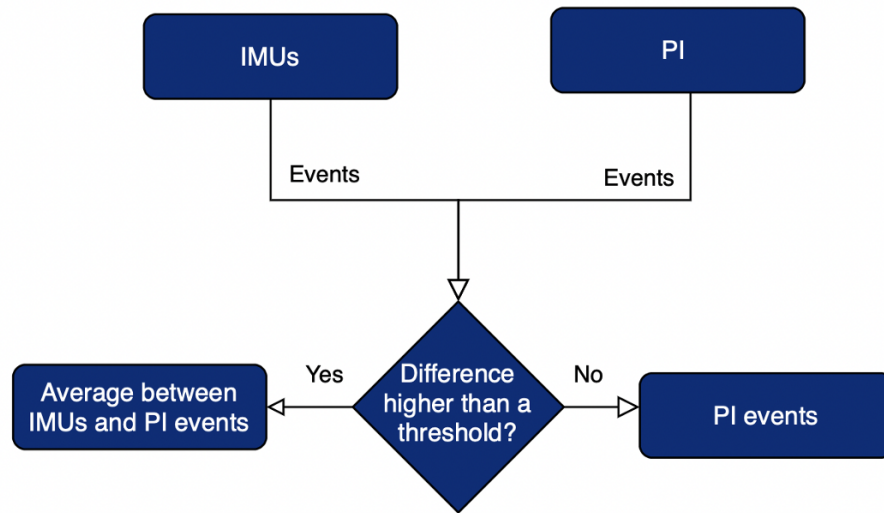


Figure 5.21: Original Algorithm Flowchart for merging PI and IMUs event information.

this, greater emphasis is placed on the IMU data. Therefore, the instantaneous values of each event detected by both systems are consistently averaged to achieve a balanced representation that considers the significance of the IMU data. Both systems receive equal weight in this process, the flowchart of the modified process can be seen in Figure 5.22.

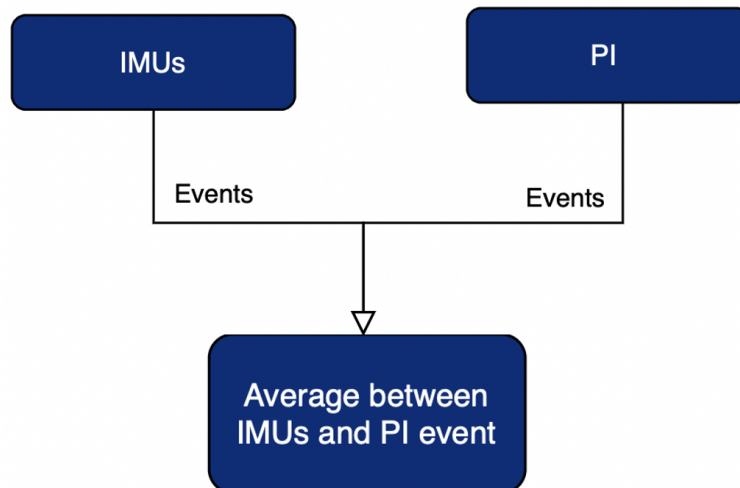


Figure 5.22: Modified Algorithm Flowchart for merging PI and IMUs event information.

To support this theory and perform this approach, the event instants identified with the SP system were compared with both PI and IMU systems by calculating the Mean Absolute Error. This comparison was conducted for each condition and each subject, resulting in two heatmaps. Furthermore, these results demonstrate that the inertial sensors are more sensitive but have lower specificity compared to the pressure insoles (PI). This implies that the PI system is better at identifying events and rarely misses any, while the values obtained from the inertial sensors are more accurate when an event is detected by both systems. Only in this case, the measurements from the inertial sensors can be considered the more precise and reliable option. Ultimately, all the values were averaged, and the resulting heatmaps can be observed in Figure 5.23 and Figure 5.24 respectively.

MAE BETWEEN PI AND SP EVENT INSTANTS							
Condition	Subject 03	Subject 04	Subject 05	Subject 07	Subject 08	Subject 09	Mean
Overground 0°	0.03	0.08	0.05	0.09	0.08	0.04	0.06
Overground 15°	0.02	0.07	0.05	0.08	0.05	0.03	0.05
Mat 0°	0.08	0.06	0.04	0.09	0.06	0.03	0.06
Mat 15°	0.05	0.06	0.05	0.07	0.07	0.03	0.05
Unstructured 0°	0.04	0.09	0.07	0.09	0.08	0.03	0.07
Unstructured 15°	0.05	0.09	0.02	0.07	0.06	0.04	0.05
Sawtooth Upward 0°	0.01	0.09	0.00	0.09	0.07	0.03	0.05
Sawtooth Upward 15°	0.05	0.08	0.02	0.09	0.07	0.02	0.06
Sawtooth Downward 0°	0.01	0.07	0.02	0.07	0.17	0.01	0.06
Sawtooth Downward 15°	0.03	0.06	0.01	0.05	0.06	0.01	0.04
Mean	0.04	0.08	0.03	0.08	0.08	0.03	0.05
Total Mean	0.05						0.05

Figure 5.23: Heatmap showcasing the MAE between events detected using the INDIP’s PI and events identified through the SP system.

MAE BETWEEN IMU AND SP EVENT INSTANTS							
Condition	Subject 03	Subject 04	Subject 05	Subject 07	Subject 08	Subject 09	Mean
Overground 0°	0.03	0.06	0.04	0.06	0.07	0.03	0.05
Overground 15°	0.02	0.07	0.01	0.07	0.02	0.02	0.04
Mat 0°	0.05	0.03	0.06	0.05	0.05	0.00	0.04
Mat 15°	0.00	0.04	0.03	0.03	0.03	0.01	0.02
Unstructured 0°	0.01	0.06	0.01	0.05	0.07	0.02	0.04
Unstructured 15°	0.01	0.08	0.03	0.02	0.05	0.03	0.04
Sawtooth Upward 0°	0.03	0.10	0.05	0.06	0.05	0.01	0.05
Sawtooth Upward 15°	0.00	0.08	0.03	0.00	0.10	0.05	0.04
Sawtooth Downward 0°	0.03	0.03	0.02	0.05	0.11	0.04	0.04
Sawtooth Downward 15°	0.01	0.01	0.02	0.03	0.08	0.03	0.03
Mean	0.02	0.06	0.03	0.04	0.06	0.02	0.04
Total Mean	0.04						0.04

Figure 5.24: Heatmap showcasing the MAE between events detected using the INDIP’s IMUs and events identified through the SP system.

Both figures were color-coded using the same scale, enabling the use of a color palette to discern differences. Figure 5.24 exhibits a slightly lighter color compared to Figure 5.23, suggesting that the time differences obtained with the IMUs are smaller than those obtained with the PI system. However, despite this distinction, the discrepancies between the values are not significant, allowing for an average to be calculated using the instants identified by both systems.

5.4 Data analysis

5.4.1 Event Identification Analysis

As explained before events were obtained from both INDIP and VICON systems. The PI of the INDIP system serves as the benchmark for event identification. This is because by analyzing foot pressure, it becomes possible to determine when an IC or FC occurs, as explained in previous chapters. Consequently, when it comes to identifying events, there is no notion of error, but rather distinctions (or differences) between systems. Metrics adopted to study the differences between these events are:

- Mean Absolute Difference (secs): refers to the expected value, or average, of the absolute difference between two independently and identically distributed random variables X and Y , which have the same unknown distribution (referred to as Q). With the respective standard deviation of the error.
- Mean Difference (secs): measures the absolute difference between the mean value in two different groups. In clinical trials, it gives you an idea of how much difference there is between the averages of the experimental group and control groups. With the respective standard deviation of the error.

A more graphic comparison is obtained through the use of a Bland Altman plot:

- Bland Altman Plot: is a type of graph used to assess the agreement between two methods of measurement or between two observers. The plot displays the differences between the two methods or observers (y-axis) against the mean of the two methods or observers (x-axis). The mean difference is represented by a horizontal line on the plot, and the limits of agreement are calculated as the mean difference plus and minus two standard deviations of the differences.

5.4.2 Spatio-temporal Parameters Analysis

In this particular scenario, VICON serves as a reliable reference point or gold standard because it directly provides trajectories through its system. These trajectories,

in turn, allow for the estimation of parameters. Therefore, the parameters obtained using the INDIP system will be compared to those obtained using VICON. Among the various parameters that could be considered, this project focused on studying the following ones:

- Spatial Parameters:
 - Stride Length.
- Temporal Parameters:
 - Stride Time.
 - Cadence.
- Velocity Parameters:
 - Walking Speed.

To analyze and determine statistical significance between these parameters in different conditions, a t-test was conducted. The t-test evaluates whether the means of the two data groups are statistically similar or different. It assesses the null hypothesis that there is no significant difference between the means of the two groups, determining if any observed differences are statistically significant or simply due to random chance. By performing the t-test, it is possible to assess whether the observed differences in the parameters across conditions are statistically meaningful. Besides, for a deeper statistical analysis various metrics were derived:

- Mean: is the average value of all the parameters. It is calculated by adding up all the values and dividing the sum by the number of data points. The mean is a measure of central tendency that represents the typical value in the dataset.

$$\text{Mean} = \frac{1}{n} \sum_{i=1}^n y_i \quad (5.4)$$

- Standard Deviation: is a measure of the amount of variation or dispersion in the parameters. It represents the average distance of each data point from the mean.

$$SD = \sqrt{\frac{1}{n} \sum_{i=1}^n (y_i - \mu)^2} \quad (5.5)$$

Where μ is the mean of the data.

- Mean Error (ME): refers to the average difference between the predicted and actual values of the parameters. It is calculated by taking the mean of the differences between the predicted and actual values.

$$ME = \frac{1}{n} \sum (y_i - \hat{y}_i) \quad (5.6)$$

Where n is the number of data points, y_i is the actual value of the i -th data point, and \hat{y}_i : the predicted value of the i -th data point.

- Mean Absolute Error (MAE): is a measure of the accuracy of a model, which represents the average absolute difference between the predicted and actual values. It is calculated by taking the mean of the absolute differences between the predicted and actual values.

$$MAE = \frac{1}{n} \sum_{i=1}^n |y_i - \hat{y}_i| \quad (5.7)$$

- Median Error (MDE): is a statistical metric that measures the central tendency or the average value of errors in a set of predictions or estimates. It provides an indication of the typical deviation between the predicted values and the actual values, without considering the direction of the errors.

$$MDE = median(y - \hat{y}) \quad (5.8)$$

Where y represents the actual or observed values, \hat{y} represents the predicted or estimated values, and $median$ denotes the median value of the set. If the number of absolute differences is odd, the median is the middle value. If the number of absolute differences is even, the median is the average of the two middle values.

- Median Absolute Error (MDAE): is a statistical metric that measures the central tendency or typical deviation of errors in a set of predictions or estimates. It is a robust alternative to Mean Absolute Error (MAE) that is less affected by outliers. The formula for calculating the median absolute error is as follows:

$$MDAE = median(|y - \hat{y}|) \quad (5.9)$$

Where y represents the actual or observed values, \hat{y} represents the predicted or estimated values, and $median(|x|)$ denotes the median of the absolute differences between the values in the set x .

- Interquartile Range Error (IQRE): is a statistical metric that measures the spread or dispersion of errors in a set of predictions or estimates. It is calculated based on the interquartile range, which is a measure of the variability within a dataset. The IQRE represents the spread or dispersion of errors in the dataset. It provides a measure of the middle 50% of the absolute differences, indicating the range in which the majority of the errors fall. The IQR Error is useful for understanding the variability and distribution of errors, particularly in situations where there may be outliers or skewed distributions.

$$IQRE = Q3 - Q1, \quad (5.10)$$

where Q1 represents the first quartile (25th percentile) of the absolute differences and Q3 represents the third quartile (75th percentile) of the absolute differences.

- Intraclass Correlation (ICC): is a statistical measure used to assess the similarity between two or more measurements made by different observers or methods. It represents the proportion of the total variance in the measurements that is due to the differences between the observers or methods. ICC values range from 0 to 1, with higher values indicating greater agreement between the measurements.

$$ICC = \frac{MS_u - MS_e}{MS_u + (k - 1) * MS_e} \quad (5.11)$$

Where MS_u is the between-group mean square, MS_e is the within-group mean square and k : the number of groups being compared.

For obtaining a graphic comparison between parameters values, bar plots with the proper standard deviation for both systems are used.

Chapter 6

Results

This chapter presents the results obtained using the original algorithm and compares them to the SP system. Additionally, it compares the results obtained using the modified code against the SP system. The chapter is divided into a first part in which the identification and differentiation of gait events between both systems are analyzed, and a second part for the calculation of spatio-temporal parameters. The results from both the original code and the modified code are compared with the reference system.

6.1 Event identification analysis

6.1.1 Original vs Modified Algorithm comparison

To enhance the clarity and structure of the comparison between event identification methods, the results will be categorized based on different terrain conditions. This categorization will allow for a direct comparison with the already explained metrics, between the original algorithm results and those obtained with the modified version, aiding in the evaluation of both codes. In every scenario, a Bland-Altman analysis will be carried out to showcase the differences in time between VICON and INDIP for all events, initially without discriminating between IC and FC. Subsequently, a separate analysis for specifically the IC and FC events is presented.

Plane Terrain at 0°

Figures 6.1, 6.2 and 6.3 presents the Bland Altman plots representing the time differences between the original INDIP algorithm in the first column with the optimized algorithm in the second column, both compared against the SP system for the **plane terrain at 0°**. For a more quantitative representation, in Table 6.1, the MD, MAD and STD of the MD are presented.

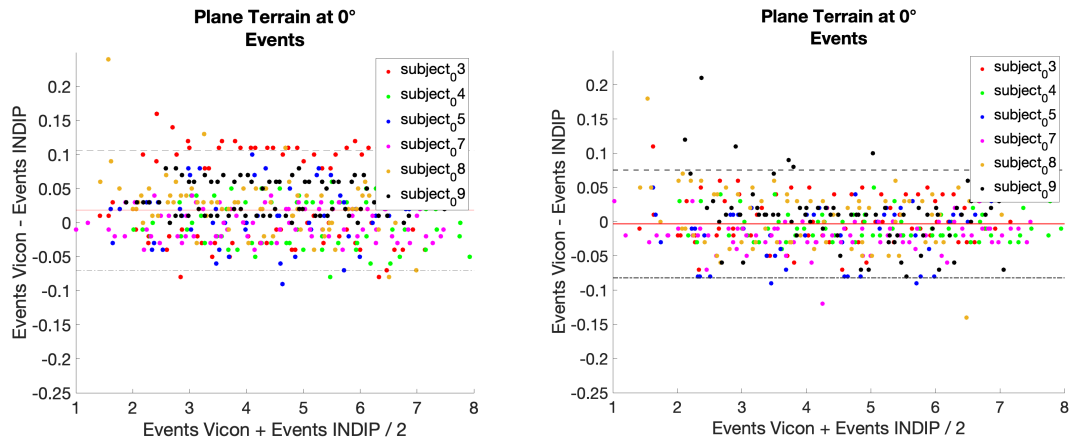


Figure 6.1: Bland Altman event differences for Plane Terrain at 0° with the A) Original Code and B) Modified Code.

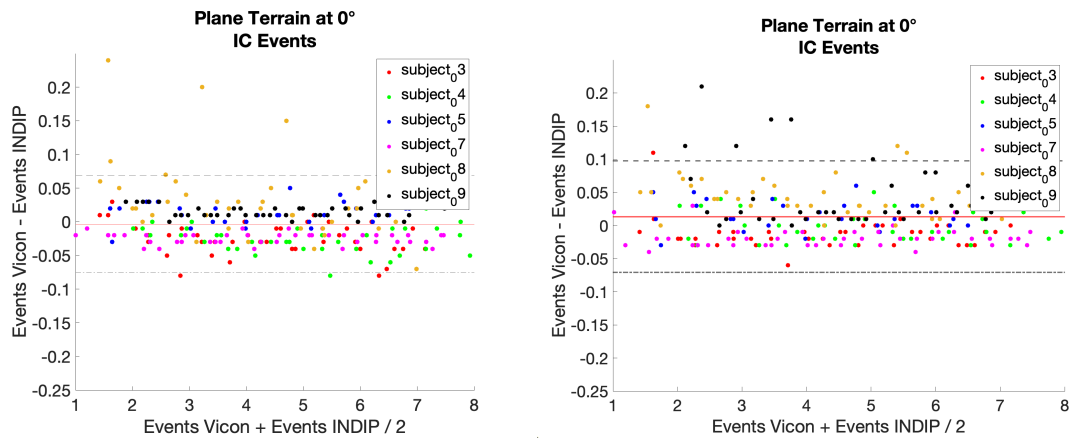


Figure 6.2: Bland Altman IC differences for Plane Terrain at 0° with the A) Original Code and B) Modified Code.

Plane Terrain at 15°

Figures 6.4, 6.5 and 6.6 presents the Bland Altman plots representing the time differences between the original INDIP algorithm in the first column with the optimized algorithm in the second column, both compared against the SP system for the **plane terrain at 15°** . For a more quantitative representation, in Table 6.2, the MD, MAD and STD of the MD are presented.

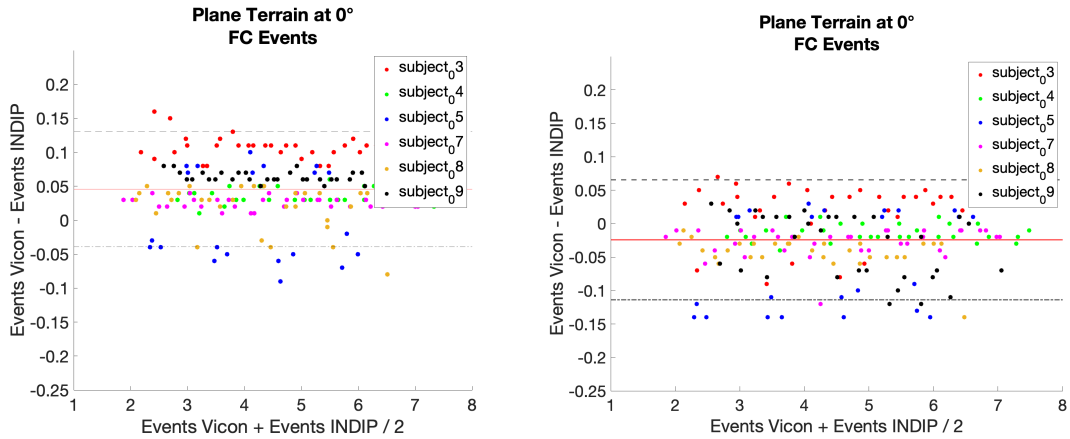


Figure 6.3: Bland Altman FC differences for Plane Terrain at 0° with the A) Original Code and B) Modified Code.

Table 6.1: Time differences for Plane Terrain at 0° between the original and modified code.

Overground 0°	Original Code			Modified Code		
Subject	MD (MD%)	MAD (MAD%)	MD STD	MD (MD%)	MAD (MAD%)	ME STD
3	0.00 (-0.08)	0.03 (0.82)	0.07	-0.03 (-0.81)	0.03 (0.91)	0.03
4	0.01 (0.11)	0.02 (0.43)	0.03	0.00 (-0.02)	0.01 (0.21)	0.01
5	0.01 (0.41)	0.03 (0.88)	0.05	-0.01 (-0.27)	0.04 (1.07)	0.04
7	0.02 (0.54)	0.02 (0.67)	0.02	0.00 (0.03)	0.01 (0.33)	0.02
8	0.06 (1.43)	0.07 (2.06)	0.09	0.05 (1.20)	0.09 (1.68)	0.06
9	-0.01 (-0.58)	0.04 (0.07)	0.03	-0.58 (0.04)	0.04 (0.07)	0.05

Mat terrain at 0°

Figures 6.7, 6.8 and 6.9 presents the Bland Altman plots representing the time differences between the original INDIP algorithm in the first column with the optimized algorithm in the second column, both compared against the SP system for the **mat terrain at 0°** . For a more quantitative representation, in Table 6.3, the MD, MAD and STD of the MD are presented.

Mat terrain at 15°

Figures 6.10, 6.11 and 6.12 presents the Bland Altman plots representing the time differences between the original INDIP algorithm in the first column with the optimized algorithm in the second column, both compared against the SP system for the **mat terrain at 15°** . For a more quantitative representation, in Table 6.4,

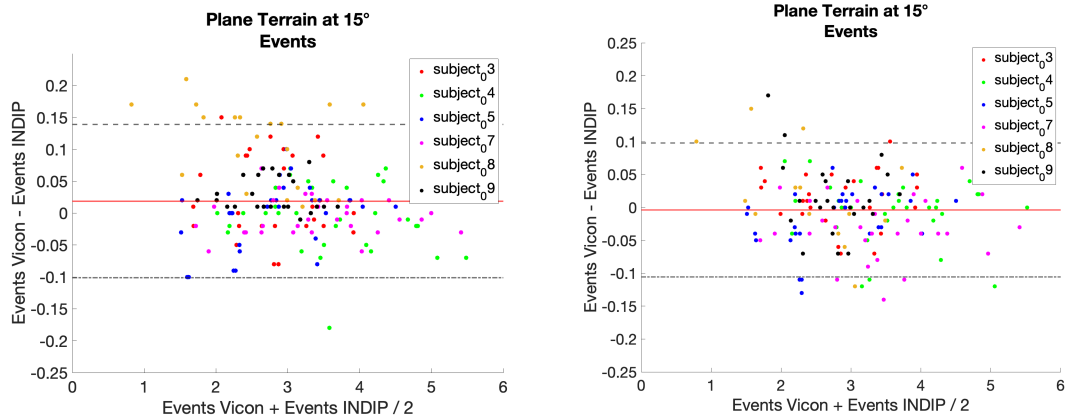


Figure 6.4: Bland Altman event differences for Plane Terrain at 15° with the A) Original Code and B) Modified Code.

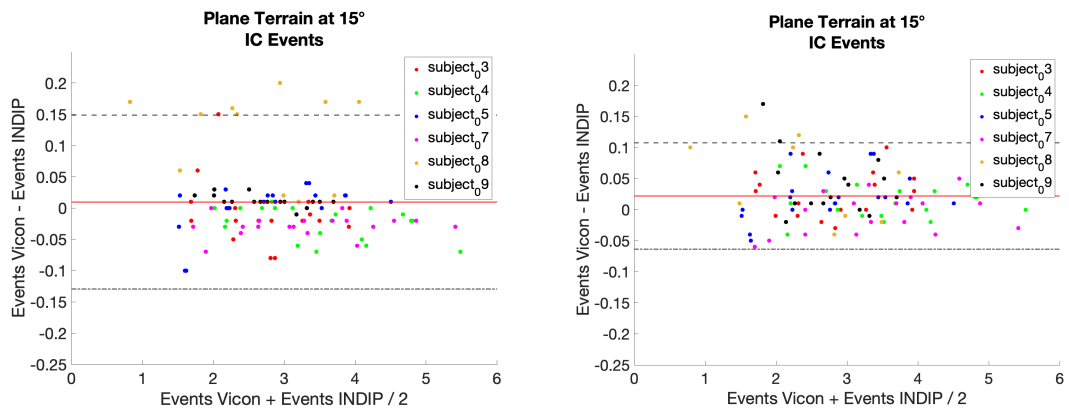


Figure 6.5: Bland Altman IC differences for Plane Terrain at 15° with the A) Original Code and B) Modified Code.

the MD, MAD and STD of the MD are presented.

Unstructured Terrain at 0°

Figures 6.13, 6.14 and 6.12 presents the Bland Altman plots representing the time differences between the original INDIP algorithm in the first column and the optimized algorithm in the second column, both compared against the SP system for the **unstructured terrain at 0°** . For a more quantitative representation, in Table 6.5, the MD, MAD and STD of the MD are presented.

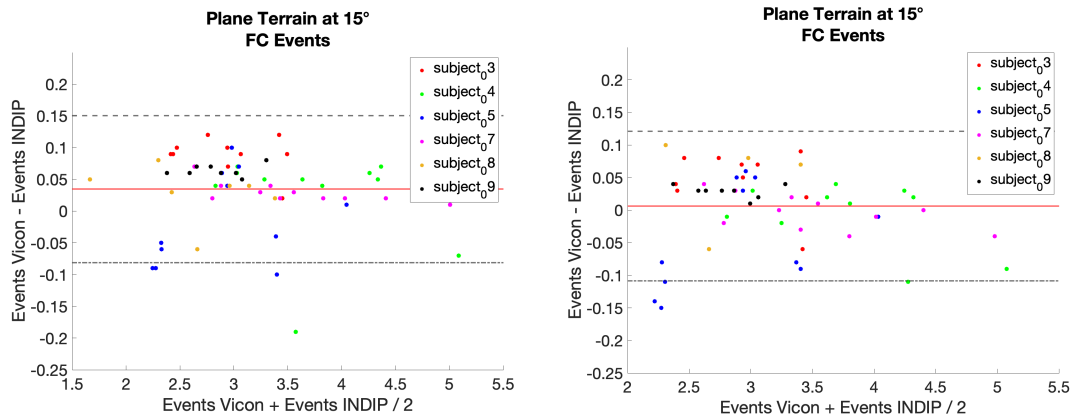


Figure 6.6: Bland Altman FC differences for Plane Terrain at 15° with the A) Original Code and B) Modified Code.

Table 6.2: Time differences for the overground terrain at 15° between the original and modified code.

Overground 15°	Original Code			Modified Code			
	Subject	MD (MD%)	MAD (MAD%)	MD STD	MD (MD%)	MAD (MAD%)	ME STD
3		0.03 (1.13)	0.03 (1.23)	0.04	0.03 (-1.03)	0.04 (1.30)	0.02
4		0.01 (0.13)	0.03 (0.95)	0.05	0.02 (-0.03)	0.03 (0.60)	0.00
5		0.02 (0.76)	0.03 (1.38)	0.05	0.04 (-0.14)	0.05 (1.48)	0.00
7		0.03 (0.95)	0.04 (1.36)	0.05	0.02 (0.21)	0.02 (0.49)	0.01
8		0.04 (0.66)	0.09 (4.35)	0.11	0.10 (0.42)	0.12 (4.71)	0.03
9		-0.02 (-0.76)	0.04 (1.66)	0.06	0.03 (-1.35)	0.03 (1.35)	0.03

Unstructured Terrain at 15°

Figures 6.16, 6.17 and 6.18 presents the Bland Altman plots representing the time differences between the original INDIP algorithm in the first column and the optimized algorithm in the second column, both compared against the SP system for the **unstructured terrain at 15°** . For a more quantitative representation, in Table 6.6, the MD, MAD and STD of the MD are presented.

Upward Sawtooth at 0°

Figures 6.19, 6.20 and 6.21 presents the Bland Altman plots representing the time differences between the original INDIP algorithm in the first column and the optimized algorithm in the second column, both compared against the SP system for the **upward sawtooth terrain at 0°** . For a more quantitative representation,

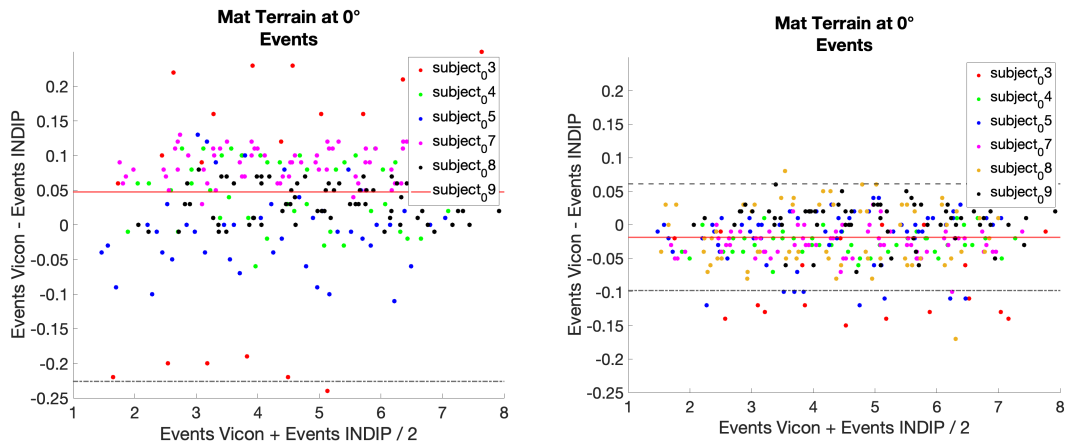


Figure 6.7: Bland Altman event differences for Mat Terrain at 0° with the A) Original Code and B) Modified Code.

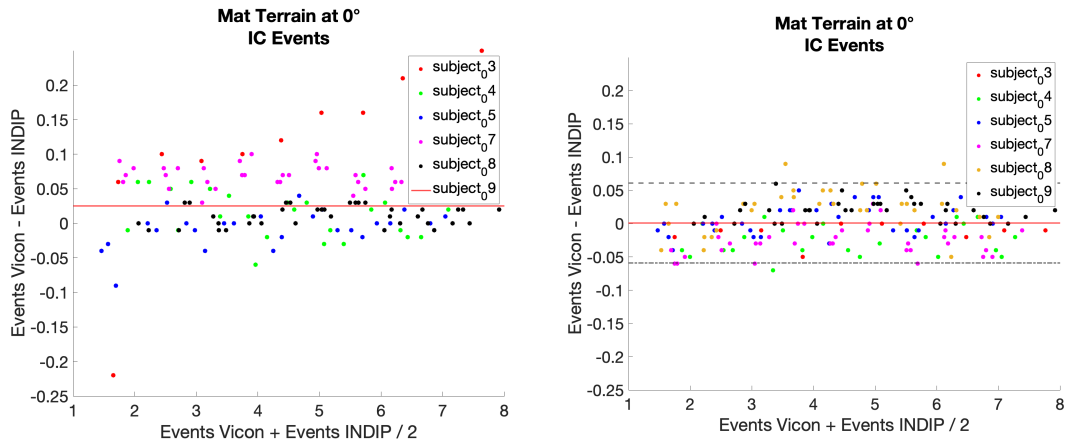


Figure 6.8: Bland Altman IC differences for Mat Terrain at 0° with the A) Original Code and B) Modified Code.

in Table 6.7, the MD, MAD and STD of the MD are presented.

Upward Sawtooth at 15°

Figures 6.22, 6.23 and 6.24 presents the Bland Altman plots representing the time differences between the original INDIP algorithm in the first column and the optimized algorithm in the second column, both compared against the SP system for the **upward sawtooth terrain at 15°** . For a more quantitative representation, in Table 6.8, the MD, MAD and STD of the MD are presented.

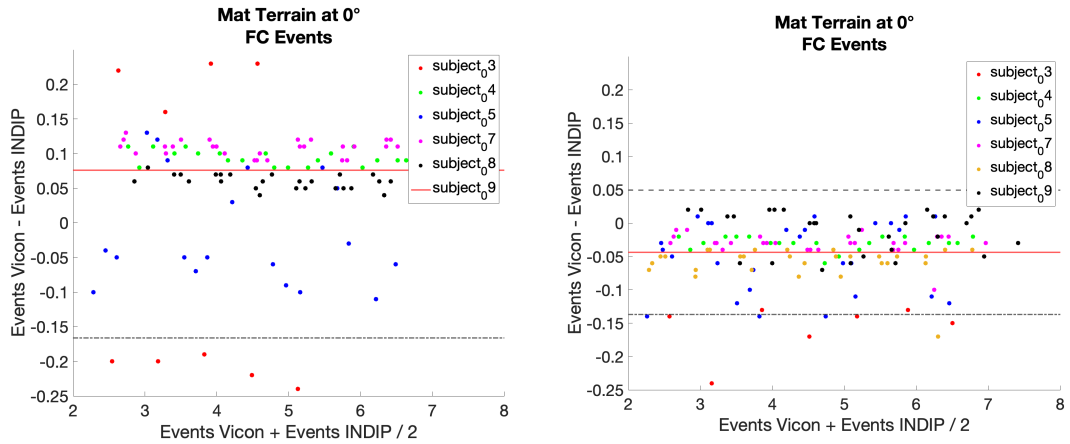


Figure 6.9: Bland Altman FC differences for Mat Terrain at 0° with the A) Original Code and B) Modified Code.

Table 6.3: Time differences for the Mat terrain at 0° between the original and modified code.

Mat 0°	Original Code			Modified Code		
Subject	MD (MD%)	MAD (MAD%)	MD STD	MD (MD%)	MAD (MAD%)	ME STD
3	0.05 (1.23)	0.25 (5.51)	0.26	-0.05 (-1.19)	0.19 (4.06)	0.19
4	-0.05 (-1.22)	0.06 (1.43)	0.05	0.03 (0.65)	0.03 (0.69)	0.02
5	-0.01 (-0.04)	0.05 (1.48)	0.09	0.02 (0.05)	0.03 (0.80)	0.04
7	-0.09 (-2.18)	0.09 (2.18)	0.02	0.03 (0.69)	0.03 (0.74)	0.02
8	NaN (NaN)	NaN (NaN)	NaN	0.12 (3.30)	0.12 (3.30)	0.05
9	-0.03 (-0.68)	0.03 (0.73)	0.03	-0.01 (-0.17)	0.02 (0.47)	0.03

Downward Sawtooth at 0°

Figures 6.25, 6.26 and 6.27 presents the Bland Altman plots representing the time differences between the original INDIP algorithm in the first column and the optimized algorithm in the second column, both compared against the SP system for the **downward sawtooth terrain at 0°** . For a more quantitative representation, in Table 6.9, the MD, MAD and STD of the MD are presented.

Downward Sawtooth at 15°

Figures 6.28, 6.29 and 6.30 presents the Bland Altman plots representing the time differences between the original INDIP algorithm in the first column and the optimized algorithm in the second column, both compared against the SP system for the **downward sawtooth terrain at 15°** . For a more quantitative

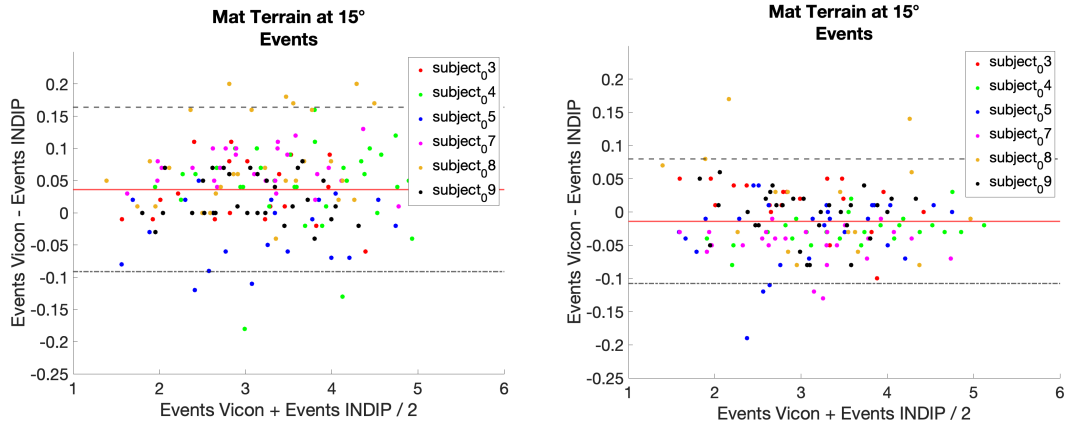


Figure 6.10: Bland Altman event differences for Mat Terrain at 15° with the A) Original Code and B) Modified Code.

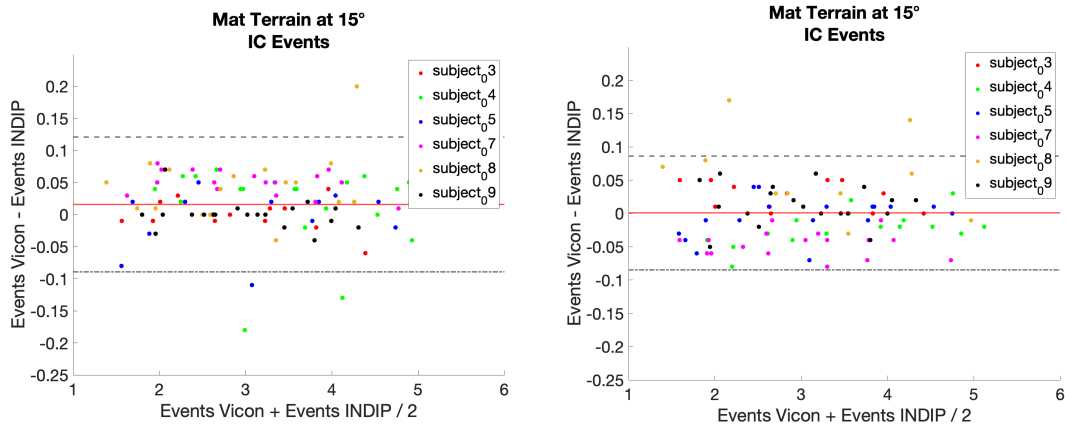


Figure 6.11: Bland Altman IC differences for Mat Terrain at 15° with the A) Original Code and B) Modified Code.

representation, in Table 6.10, the MD, MAD and STD of the MD are presented.

6.2 Spatio-temporal Parameters Analysis

In Table 6.11 all the final values calculated with the already mentioned metrics are presented, is important to highlight that these values are calculated with the spatio temporal parameters obtained with the modified code.

For presenting the mean and standard deviation values in a more graphic and visible way, the respective bar plot for each parameter is presented.

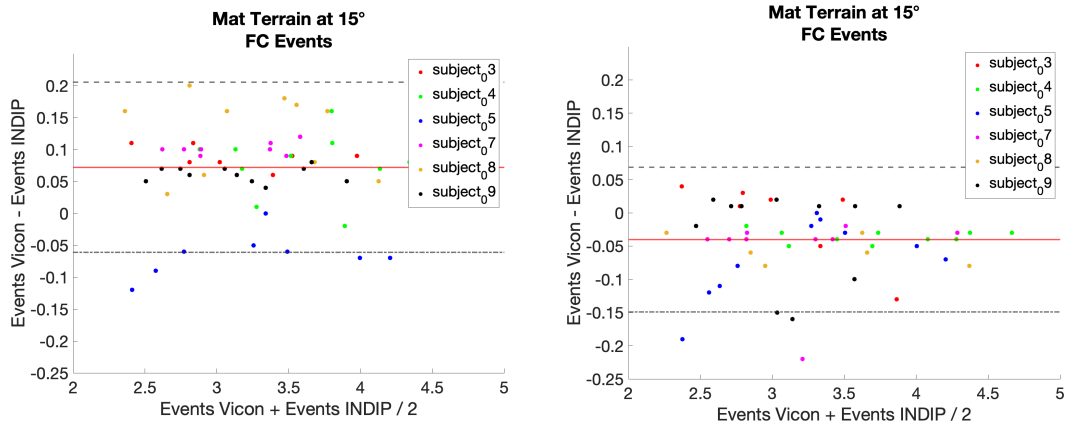


Figure 6.12: Bland Altman FC differences for Mat Terrain at 15° with the A) Original Code and B) Modified Code.

Mat 15°	Original Code			Modified Code		
Subject	MD (MD%)	MAD (MAD%)	MD STD	MD (MD%)	MAD (MAD%)	ME STD
3	-0.03 (-1.13)	0.04 (1.47)	0.05	-0.02 (-0.87)	0.03 (1.24)	0.04
4	-0.04 (-1.23)	0.07 (1.86)	0.07	0.02 (0.76)	0.03 (0.90)	0.02
5	0.03 (0.97)	0.04 (1.56)	0.05	0.03 (1.09)	0.04 (1.44)	0.05
7	-0.07 (-2.38)	0.07 (2.38)	0.03	0.05 (1.62)	0.05 (1.62)	0.03
8	-0.07 (-2.24)	0.09 (2.71)	0.09	0.06 (1.91)	0.06 (1.91)	0.08
9	-0.02 (-0.76)	0.03 (1.02)	0.04	0.00 (0.04)	0.03 (1.01)	0.04

Table 6.4: Time differences for the Mat at 15° between the original and modified code.

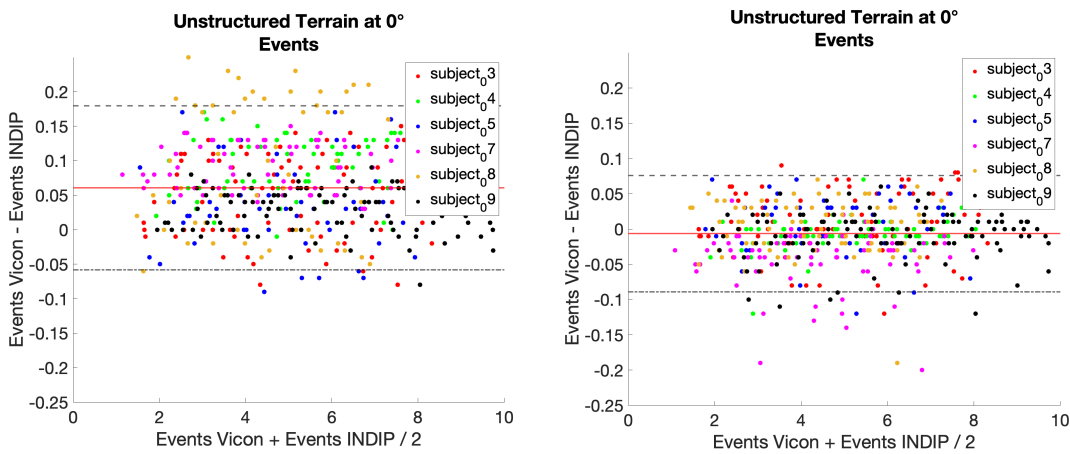


Figure 6.13: Bland Altman event differences for Unstructured Terrain at 0° with the A) Original Code and B) Modified Code.

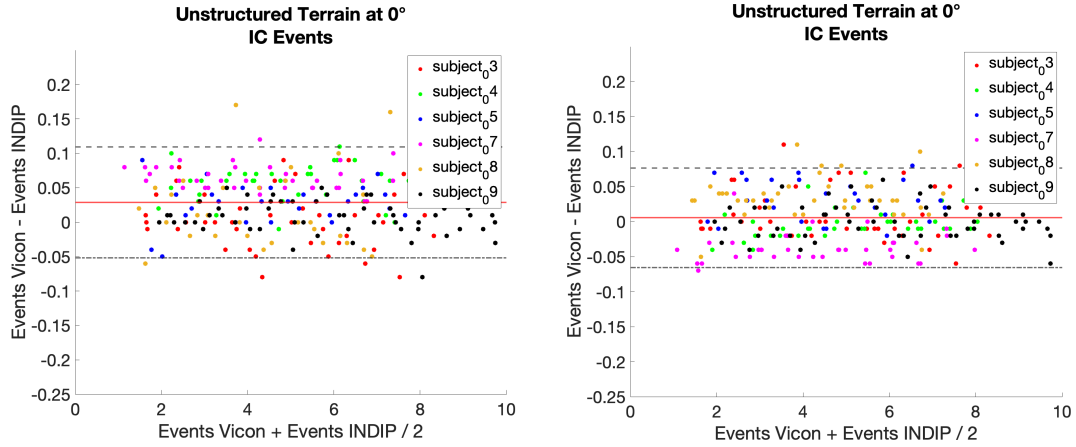


Figure 6.14: Bland Altman IC differences for Unstructured Terrain at 0° with the A) Original Code and B) Modified Code.

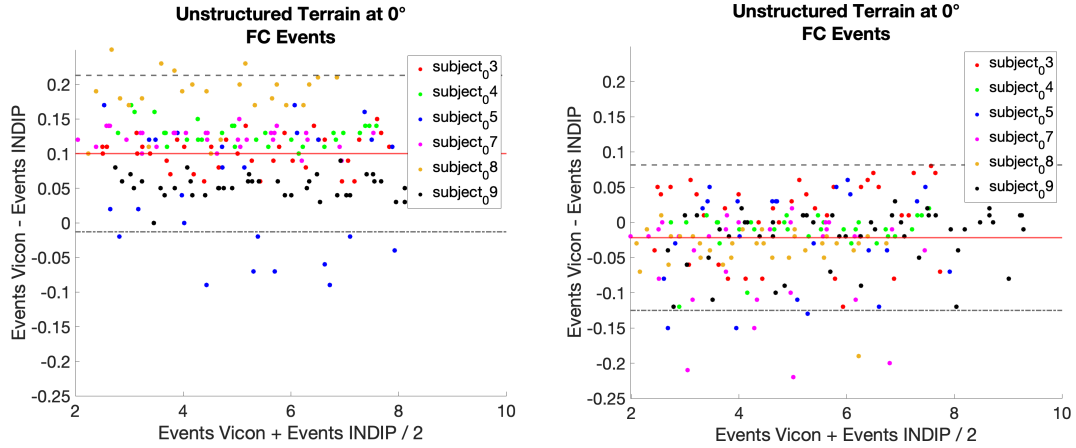


Figure 6.15: Bland Altman FC differences for Unstructured Terrain at 0° with the A) Original Code and B) Modified Code.

Unstructured 0° Subject	Original Code			Modified Code		
	MD (MD%)	MAD (MAD%)	MD STD	MD (MD%)	MAD (MAD%)	ME STD
3	-0.05 (-1.13)	0.06 (1.42)	0.06	-0.01 (-0.24)	0.04 (0.82)	0.05
4	-0.09 (-1.91)	0.09 (1.92)	0.04	0.01 (0.19)	0.02 (0.39)	0.02
5	-0.04 (-0.87)	0.06 (1.32)	0.06	-0.01 (-0.35)	0.04 (0.92)	0.05
7	-0.09 (-2.47)	0.09 (2.47)	0.03	0.04 (1.12)	0.04 (1.19)	0.04
8	-0.09 (-2.28)	0.10 (2.65)	0.10	0.05 (1.43)	0.05 (1.43)	0.05
9	-0.03 (-0.56)	0.04 (0.66)	0.03	0.01 (0.21)	0.02 (0.50)	0.03

Table 6.5: Time differences for the unstructured terrain at 0° between the original and modified code.

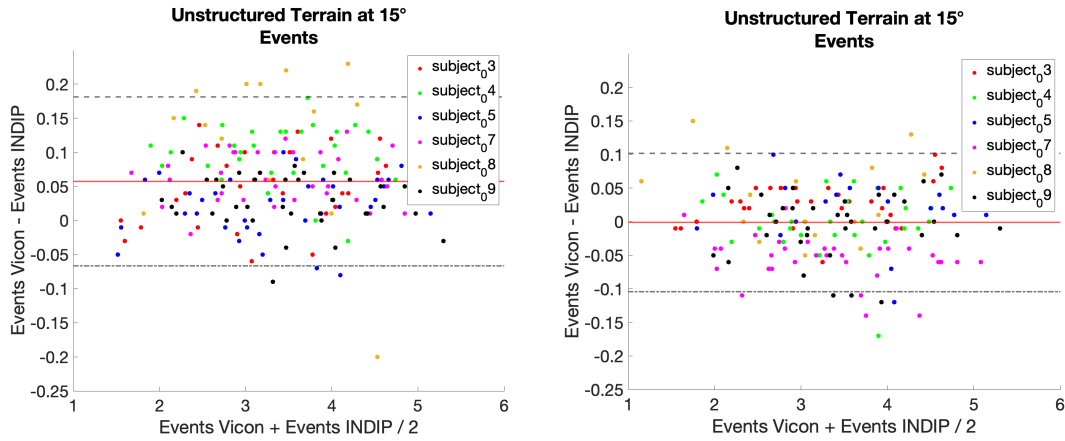


Figure 6.16: Bland Altman event differences for Unstructured Terrain at 15° with the A) Original Code and B) Modified Code.

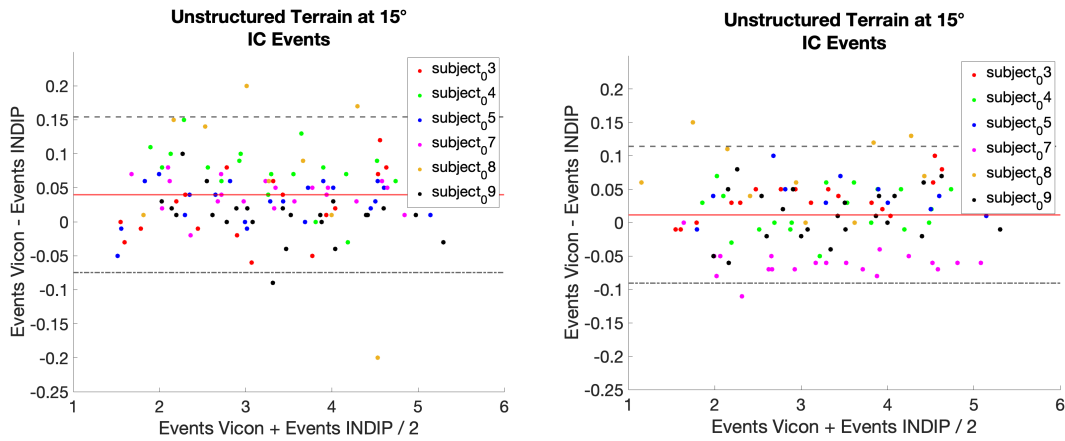


Figure 6.17: Bland Altman IC differences for Unstructured Terrain at 15° with the A) Original Code and B) Modified Code.

Unstructured 15° Subject	Original Code			Modified Code		
	MD (MD%)	MAD (MAD%)	MD STD	MD (MD%)	MAD (MAD%)	ME STD
3	-0.05 (-1.52)	0.06 (2.01)	0.06	-0.03 (-0.79)	0.03 (1.07)	0.03
4	-0.10 (-3.08)	0.10 (3.12)	0.04	0.00 (-0.12)	0.03 (0.95)	0.04
5	-0.02 (-0.62)	0.04 (1.27)	0.04	-0.01 (-0.47)	0.03 (0.95)	0.04
7	-0.06 (-2.02)	0.06 (2.07)	0.04	0.05 (1.62)	0.06 (1.70)	0.03
8	-0.13 (-5.44)	0.15 (5.98)	0.12	0.10 (3.33)	0.10 (3.35)	0.09
9	-0.03 (-0.93)	0.04 (1.22)	0.04	0.00 (-0.15)	0.03 (1.04)	0.05

Table 6.6: Time differences for the unstructured terrain at 15° between the original and modified code.

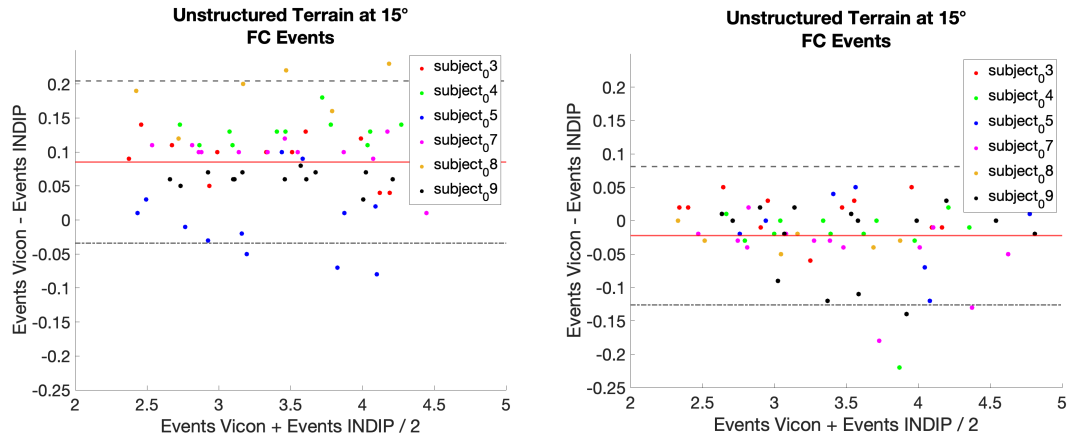


Figure 6.18: Bland Altman FC differences for Unstructured Terrain at 15° with the A) Original Code and B) Modified Code.

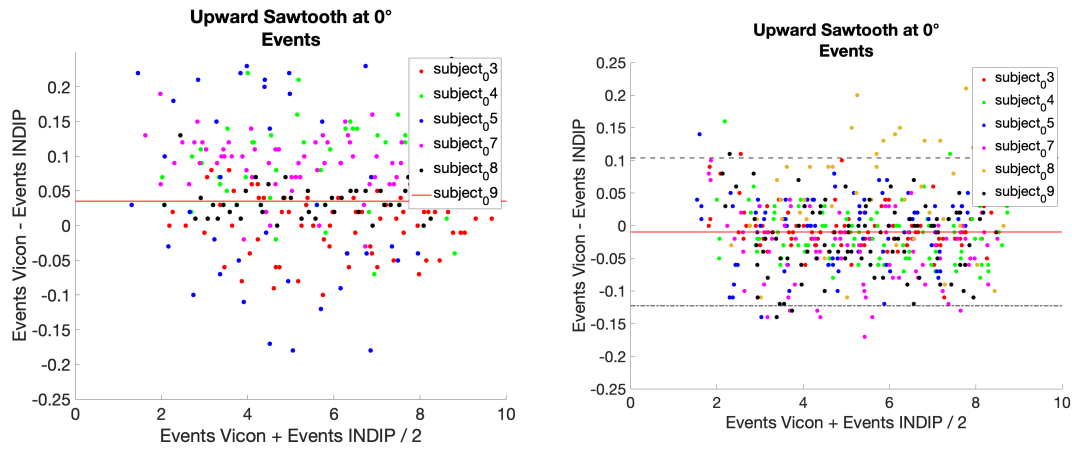


Figure 6.19: Bland Altman event differences for Upward Sawtooth Terrain at 0° with the A) Original Code and B) Modified Code.

Up Sawtooth 0°	Original Code			Modified Code		
Subject	MD (MD%)	MAD (MAD%)	MD STD	MD (MD%)	MAD (MAD%)	ME STD
3	-0.05 (-1.60)	0.06 (1.89)	0.06	0.00 (-0.09)	0.03 (0.69)	0.04
4	-0.12 (-3.47)	0.12 (3.47)	0.06	-0.10 (-1.99)	0.10 (2.09)	0.06
5	0.03 (-3.44)	0.79 (25.03)	0.82	0.01 (-0.28)	0.30 (7.20)	0.36
7	-0.07 (-1.90)	0.08 (2.12)	0.06	-0.09 (-2.15)	0.09 (2.17)	0.04
8	NaN (NaN)	NaN (NaN)	NaN	-0.34 (-9.73)	0.34 (9.73)	0.17
9	-0.03 (-1.03)	0.06 (1.85)	0.07	-0.04 (-0.81)	0.04 (0.81)	0.04

Table 6.7: Time differences for the Upward sawtooth terrain at 0° between the original and modified code.

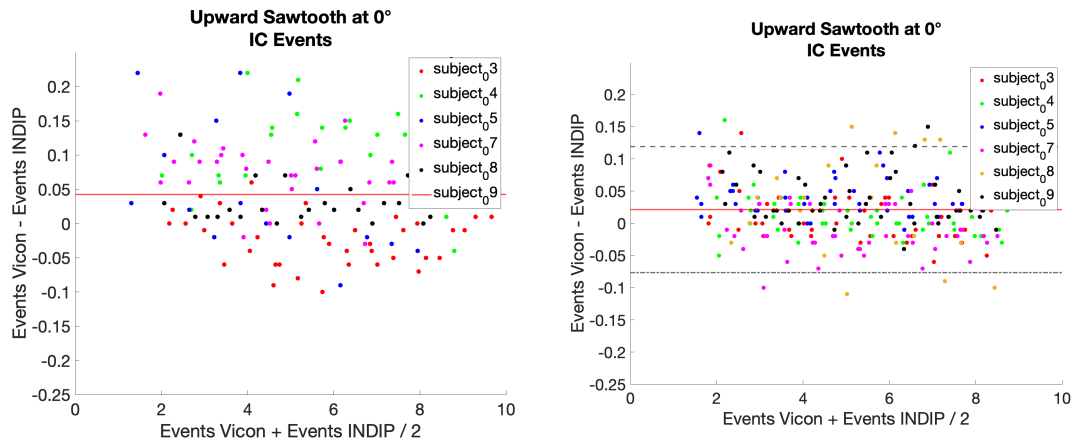


Figure 6.20: Bland Altman IC differences for Upward Sawtooth Terrain at 0° with the A) Original Code and B) Modified Code.

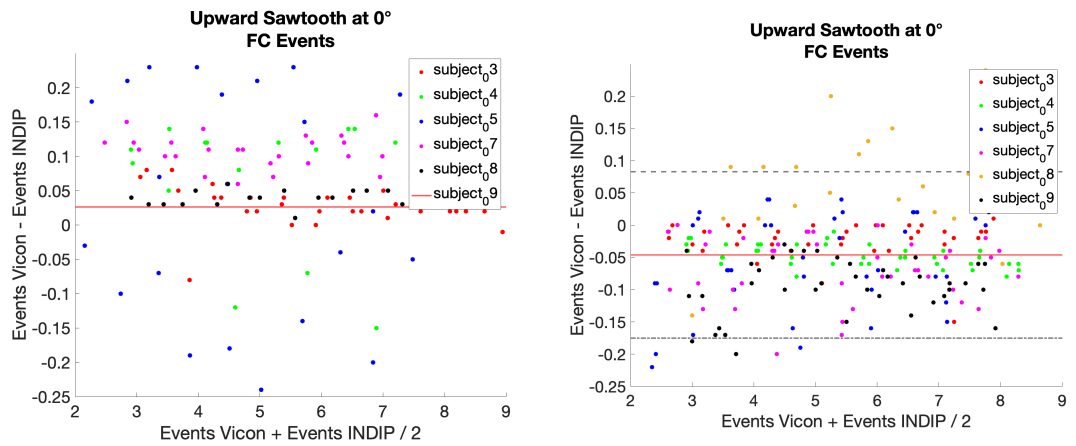


Figure 6.21: Bland Altman FC differences for Upward Sawtooth Terrain at 0° with the A) Original Code and B) Modified Code.

Up Sawtooth 15° Subject	Original Code			Modified Code		
	MD (MD%)	MAD (MAD%)	MD STD	MD (MD%)	MAD (MAD%)	ME STD
3	-0.03 (-1.01)	0.04 (1.20)	0.04	-0.03 (-0.88)	0.04 (1.08)	0.03
4	-0.13 (-3.67)	0.13 (3.67)	0.05	-0.03 (-0.88)	0.06 (1.60)	0.04
5	0.05 (-2.39)	0.80 (25.17)	0.82	0.14 (1.82)	0.42 (13.25)	0.72
7	-0.08 (-2.27)	0.09 (2.52)	0.06	0.03 (0.85)	0.04 (1.00)	0.04
8	-0.34 (-9.73)	0.34 (9.73)	0.19	-0.16 (-4.39)	0.22 (6.33)	0.17
9	-0.03 (-0.93)	0.04 (0.98)	0.04	-0.02 (-0.61)	0.05 (1.50)	0.04

Table 6.8: Time differences for the Upward sawtooth terrain at 15° between the original and modified code.

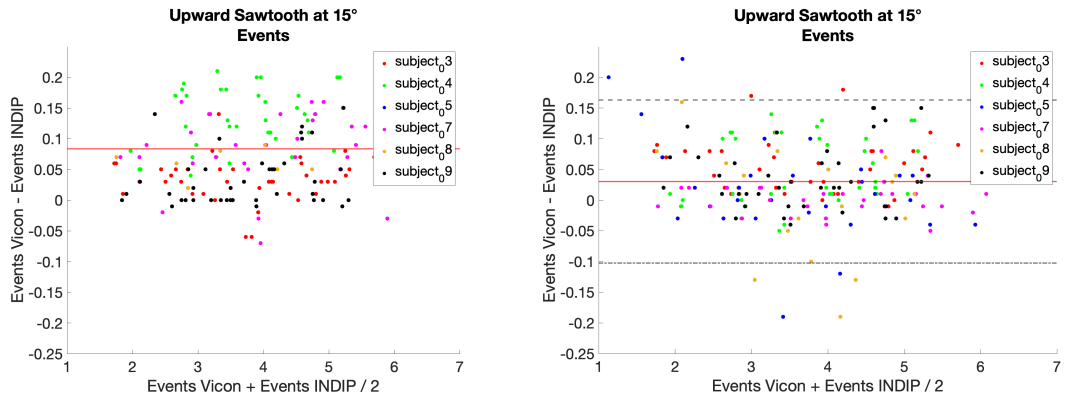


Figure 6.22: Bland Altman event differences for Upward Sawtooth Terrain at 15° with the A) Original Code and B) Modified Code.

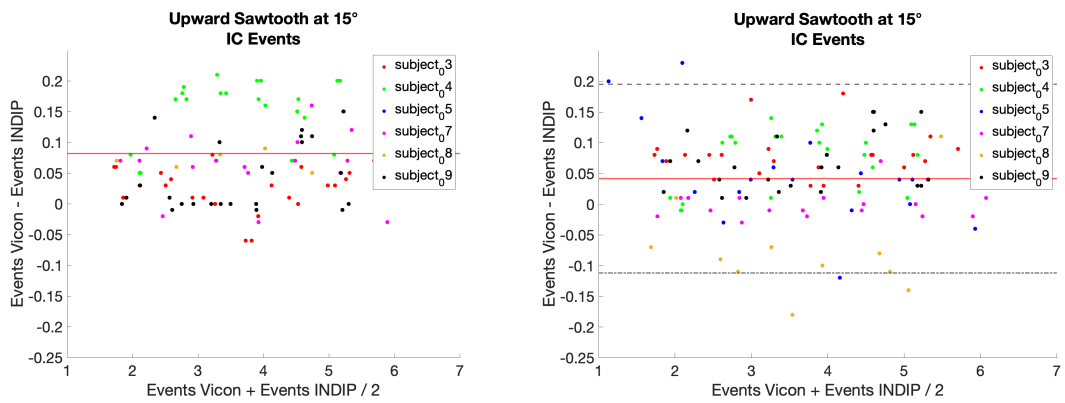


Figure 6.23: Bland Altman IC differences for Upward Sawtooth Terrain at 15° with the A) Original Code and B) Modified Code.

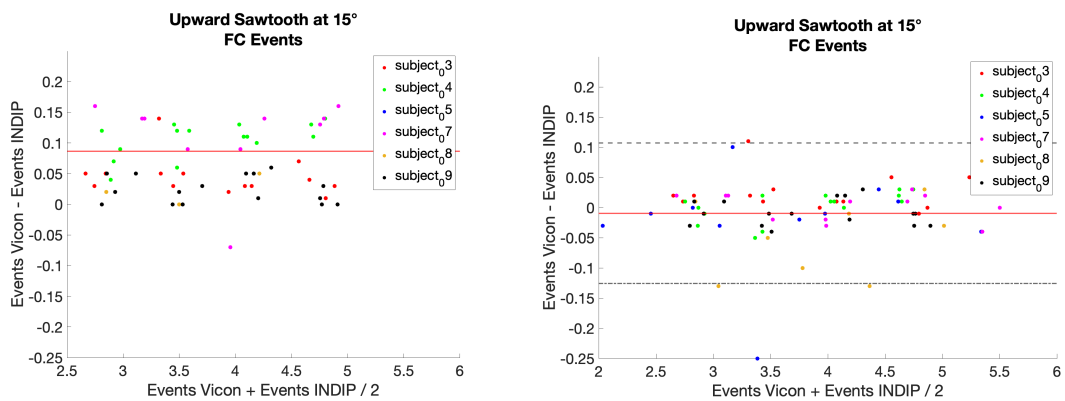


Figure 6.24: Bland Altman FC differences for Upward Sawtooth Terrain at 15° with the A) Original Code and B) Modified Code.

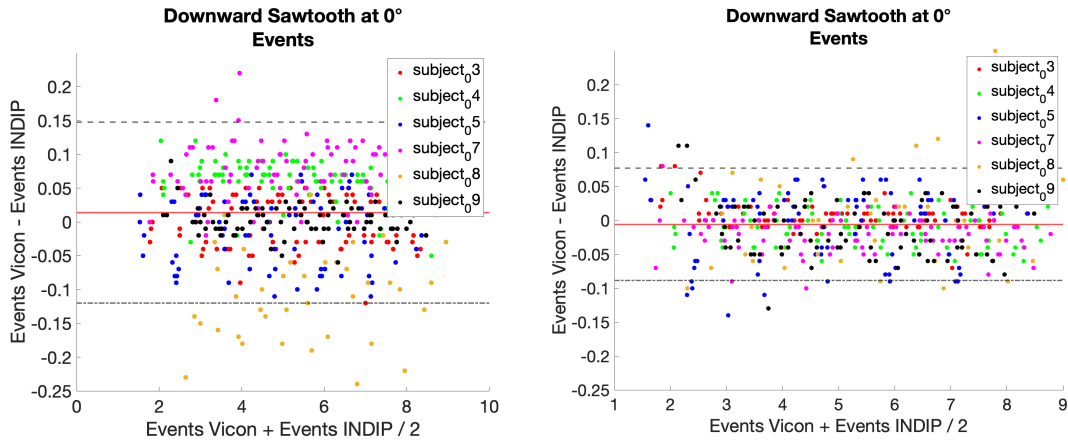


Figure 6.25: Bland Altman event differences for Downward Sawtooth Terrain at 0° with the A) Original Code and B) Modified Code.

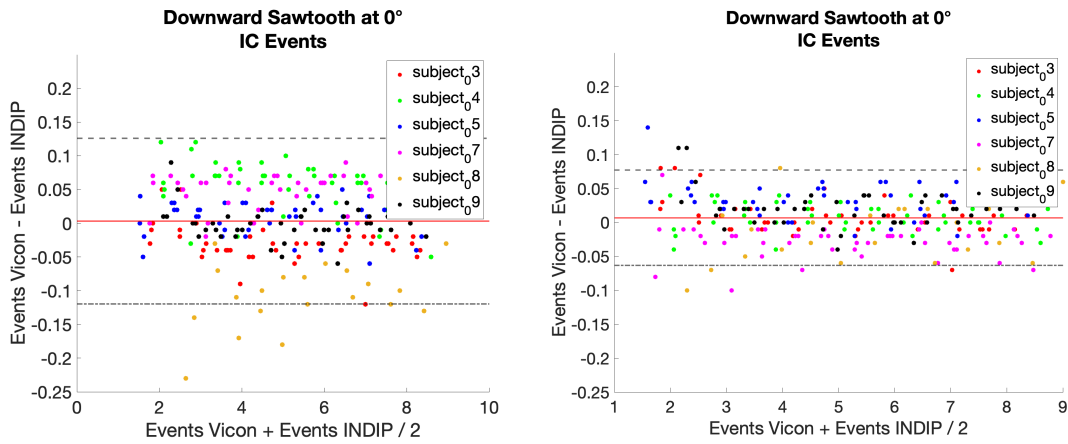


Figure 6.26: Bland Altman IC differences for Downward Sawtooth Terrain at 0° with the A) Original Code and B) Modified Code.

Down Sawtooth 0°	Original Code			Modified Code		
Subject	MD (MD%)	MAD (MAD%)	MD STD	MD (MD%)	MAD (MAD%)	ME STD
3	0.00 (-0.05)	0.04 (0.77)	0.04	0.00 (-0.01)	0.02 (0.41)	0.02
4	-0.06 (-1.37)	0.06 (1.43)	0.03	0.01 (0.18)	0.03 (0.53)	0.03
5	0.01 (0.24)	0.04 (0.97)	0.05	0.00 (0.02)	0.02 (0.87)	0.05
7	-0.07 (-1.62)	0.08 (1.64)	0.04	0.02 (0.40)	0.02 (0.54)	0.03
8	0.11 (2.37)	0.12 (2.50)	0.09	0.11 (2.14)	0.11 (2.14)	0.07
9	0.00 (-0.11)	0.02 (0.36)	0.02	0.01 (0.11)	0.01 (0.36)	0.03

Table 6.9: Time differences for the Downward sawtooth terrain at 0° between the original and modified code.

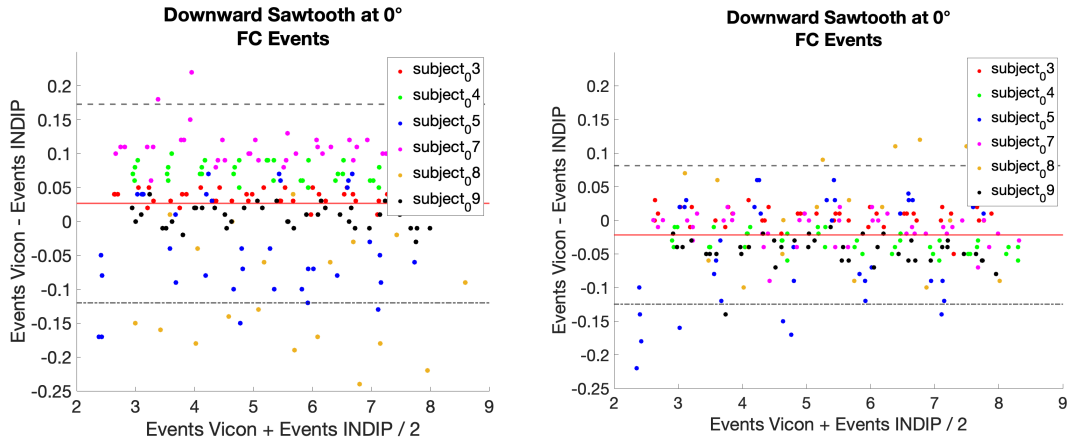


Figure 6.27: Bland Altman FC differences for Downward Sawtooth Terrain at 0° with the A) Original Code and B) Modified Code.

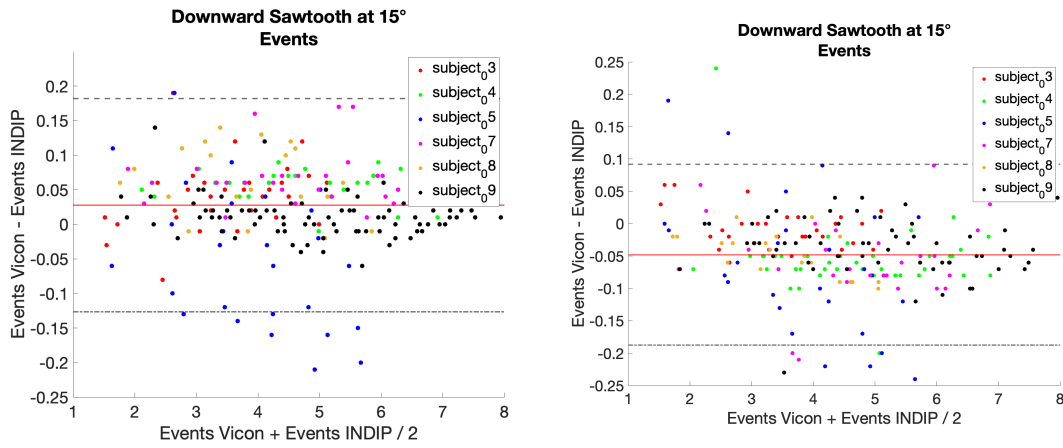


Figure 6.28: Bland Altman event differences for Downward Sawtooth Terrain at 15° with the A) Original Code and B) Modified Code.

Down Sawtooth 0°	Original Code			Modified Code		
Subject	MD (MD%)	MAD (MAD%)	MD STD	MD (MD%)	MAD (MAD%)	ME STD
3	-0.04 (-1.13)	0.05 (1.52)	0.05	-0.03 (-1.12)	0.04 (1.35)	0.04
4	-0.06 (-1.31)	0.06 (1.33)	0.02	0.02 (0.10)	0.04 (1.19)	0.02
5	0.05 (0.82)	0.11 (3.42)	0.13	0.03 (0.14)	0.12 (3.61)	0.12
7	-0.07 (-1.59)	0.07 (1.59)	0.04	0.04 (0.83)	0.05 (1.12)	0.05
8	-0.06 (-1.95)	0.07 (2.07)	0.05	0.02 (0.59)	0.06 (1.55)	0.05
9	-0.02 (-0.57)	0.03 (0.78)	0.07	-0.02 (-0.59)	0.05 (1.32)	0.07

Table 6.10: Time differences for the Downward Sawtooth terrain at 15° between the original and modified code.

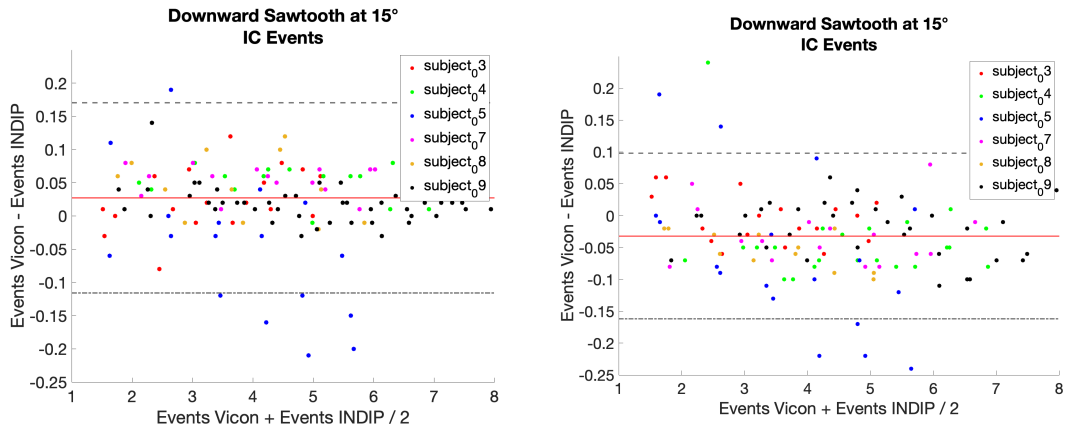


Figure 6.29: Bland Altman IC differences for Downward Sawtooth Terrain at 15° with the A) Original Code and B) Modified Code.

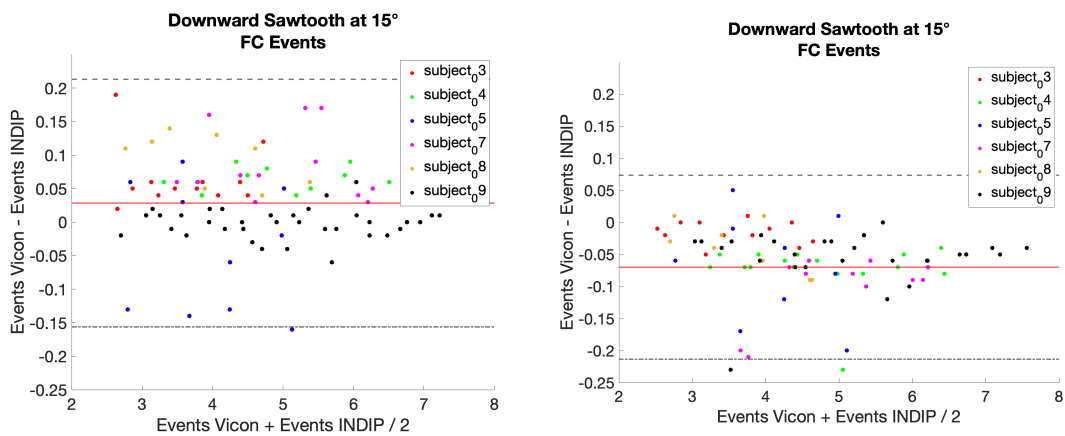


Figure 6.30: Bland Altman FC differences for Downward Sawtooth Terrain at 15° with the A) Original Code and B) Modified Code.

Table 6.11: Spatio-temporal parameters values obtained with the final algorithm modification.

Parameter	Condition	M ± STD (INDIP)	M ± STD (SP)	ME (ME%)	MDE (MDE%)	IQRE (IQRE%)	MAE (MAE %)	MDAE (MDAE %)	ICC1,1
Stride Length (m)	Overground 0°	1.46±0.11	1.47±0.09	0.02 (1.58)	0.00 (0.60)	0.08 (6.15)	0.05 (4.02)	0.04 (3.53)	0.80
	Overground 15°	1.22±0.17	1.22±0.16	0.00 (-0.35)	0.01 (0.79)	0.09 (7.30)	0.06 (4.57)	0.04 (3.99)	0.89
	Unstructured 0°	1.57±0.12	1.56±0.08	0.01 (0.85)	0.01 (0.80)	0.09 (5.96)	0.06 (3.78)	0.05 (2.84)	0.67
	Unstructured 15°	1.23±0.13	1.23±0.11	0.00 (0.12)	0.00 (0.60)	0.11 (9.33)	0.07 (5.38)	0.05 (4.20)	0.75
	Soft 0°	1.38±0.23	1.37±0.21	0.01 (0.97)	0.00 (0.50)	0.11 (8.24)	0.07 (4.98)	0.05 (3.92)	0.92
	Soft 15°	1.06±0.21	1.05±0.16	0.01 (0.82)	0.01 (0.78)	0.09 (9.26)	0.07 (6.77)	0.05 (4.85)	0.85
	Sawtooth Upward 0°	1.02±0.09	0.99±0.08	0.03 (2.89)	0.00 (0.50)	0.09 (8.46)	0.06 (6.18)	0.04 (4.42)	0.7
	Sawtooth Upward 15°	0.98±0.10	0.94±0.03	0.04 (4.04)	0.00 (0.20)	0.12 (13.00)	0.08 (8.02)	0.05 (5.71)	0.15
	Sawtooth Downward 0°	1.01±0.08	0.98±0.04	0.03 (2.85)	0.00 (0.70)	0.07 (7.43)	0.05 (5.59)	0.04 (4.49)	0.35
	Sawtooth Downward 15°	0.75±0.23	0.74±0.22	0.01 (1.71)	-0.01 (-0.83)	0.09 (11.66)	0.06 (9.08)	0.05 (5.90)	0.92
Stride Time (s)	Overground 0°	1.11±0.07	1.14±0.08	-0.01 (-0.56)	0.03 (2.05)	0.03 (2.51)	0.03 (2.26)	0.01 (0.97)	0.84
	Overground 15°	1.20±0.14	1.20±0.15	0.00 (-0.38)	0.00 (-0.49)	0.05 (4.30)	0.04 (3.32)	0.03 (2.11)	0.93
	Unstructured 0°	1.25±0.08	1.25±0.08	0.01 (0.44)	0.00 (0.29)	0.04 (3.25)	0.03 (2.00)	0.02 (1.60)	0.91
	Unstructured 15°	1.30±0.15	1.30±0.14	0.00 (0.04)	0.00 (0.07)	0.04 (3.00)	0.03 (2.11)	0.02 (1.44)	0.96
	Soft 0°	1.22±0.08	1.21±0.09	0.00 (0.06)	0.00 (0.43)	0.04 (3.15)	0.03 (2.06)	0.02 (1.58)	0.93
	Soft 15°	1.22±0.16	1.22±0.16	0.00 (0.42)	0.01 (0.81)	0.06 (4.95)	0.04 (3.01)	0.03 (2.52)	0.96
	Sawtooth Upward 0°	1.16±0.09	1.16±0.09	0.00 (0.43)	0.02 (2.29)	0.04 (3.69)	0.04 (3.36)	0.02 (1.88)	0.80
	Sawtooth Upward 15°	1.40±0.19	1.38±0.19	0.02 (1.20)	0.02 (2.48)	0.05 (3.45)	0.03 (2.63)	0.02 (1.48)	0.96
	Sawtooth Downward 0°	1.15±0.08	1.16±0.07	0.00 (-0.13)	0.02 (2.89)	0.04 (3.53)	0.02 (2.11)	0.02 (1.75)	0.92
	Sawtooth Downward 15°	1.30±0.33	1.31±0.32	-0.02 (-1.02)	0.01 (1.24)	0.08 (6.94)	0.05 (4.03)	0.04 (3.09)	0.97
Walking Speed (m/s)	Overground 0°	1.31±0.11	1.28±0.11	0.03 (2.49)	0.03 (2.05)	0.08 (6.05)	0.07 (4.49)	0.04 (3.50)	0.81
	Overground 15°	1.03±0.18	1.03±0.18	0.00 (0.13)	0.00 (-0.49)	0.08 (8.47)	0.05 (4.82)	0.04 (4.35)	0.94
	Unstructured 0°	1.26±0.11	1.25±0.08	0.01 (0.46)	0.00 (0.29)	0.08 (6.54)	0.05 (4.08)	0.04 (3.47)	0.71
	Unstructured 15°	0.96±0.14	0.96±0.14	0.00 (0.16)	0.00 (0.07)	0.10 (9.35)	0.05 (5.78)	0.05 (4.78)	0.88
	Soft 0°	1.14±0.18	1.12±0.16	0.01 (0.94)	0.00 (0.43)	0.08 (7.49)	0.05 (4.83)	0.04 (3.52)	0.91
	Soft 15°	0.88±0.17	0.87±0.13	0.01 (0.54)	0.01 (0.81)	0.09 (11.06)	0.07 (7.69)	0.05 (5.77)	0.81
	Sawtooth Upward 0°	0.88±0.08	0.86±0.06	0.02 (2.62)	0.02 (2.29)	0.09 (10.36)	0.06 (6.53)	0.04 (4.72)	0.34
	Sawtooth Upward 15°	0.71±0.10	0.69±0.08	0.02 (3.00)	0.02 (2.48)	0.11 (15.35)	0.06 (8.84)	0.05 (8.15)	0.65
	Sawtooth Downward 0°	0.88±0.08	0.85±0.06	0.03 (3.03)	0.02 (2.89)	0.07 (7.79)	0.05 (5.73)	0.04 (4.39)	0.62
	Sawtooth Downward 15°	0.59±0.15	0.57±0.13	0.02 (2.99)	0.01 (1.24)	0.08 (13.73)	0.05 (9.91)	0.04 (6.68)	0.84
Cadence (steps/min)	Overground 0°	106.03±7.49	108.31±5.55	0.75 (0.72)	0.00 (0.00)	2.54 (2.53)	2.50 (2.33)	1.12 (0.96)	0.81
	Overground 15°	101.72±13.07	101.14±12.16	0.58 (0.59)	-0.74 (-0.78)	4.09 (4.31)	3.54 (3.42)	2.08 (2.07)	0.92
	Unstructured 0°	96.18±6.28	96.56±6.07	-0.38 (-0.38)	-0.76 (-0.79)	3.17 (3.24)	1.89 (1.99)	1.54 (1.60)	0.92
	Unstructured 15°	93.67±10.75	93.68±10.90	0.00 (0.07)	0.00 (0.00)	2.71 (3.00)	1.97 (2.13)	1.24 (1.45)	0.96
	Soft 0°	99.29±7.25	99.29±6.97	0.00 (0.02)	0.00 (0.00)	2.97 (3.14)	2.05 (2.07)	1.50 (1.58)	0.93
	Soft 15°	99.72±13.40	100.11±13.84	-0.39 (-0.28)	-0.72 (-0.77)	5.25 (4.90)	2.99 (3.00)	2.40 (2.59)	0.96
	Sawtooth Upward 0°	104.06±7.97	104.34±7.40	-0.28 (-0.19)	0.00 (0.00)	3.99 (3.69)	3.46 (3.30)	1.93 (1.84)	0.78
	Sawtooth Upward 15°	87.24±10.51	88.22±10.49	-0.98 (-1.04)	0.00 (0.00)	3.13 (3.40)	2.32 (2.52)	1.15 (1.50)	0.94
	Sawtooth Downward 0°	104.53±6.71	104.38±7.10	0.15 (0.21)	0.00 (0.00)	3.70 (3.53)	2.21 (2.12)	1.85 (1.75)	0.92
	Sawtooth Downward 15°	98.28±24.57	97.20±24.35	1.08 (1.30)	0.81 (0.84)	6.37 (7.09)	3.93 (4.16)	3.01 (3.04)	0.98

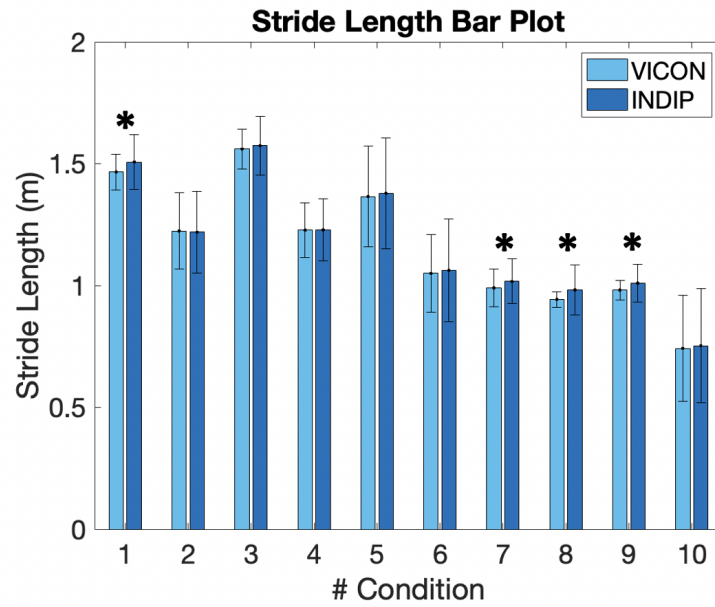


Figure 6.31: Barplot for comparing mean and standard deviation values for SL obtained with both systems.

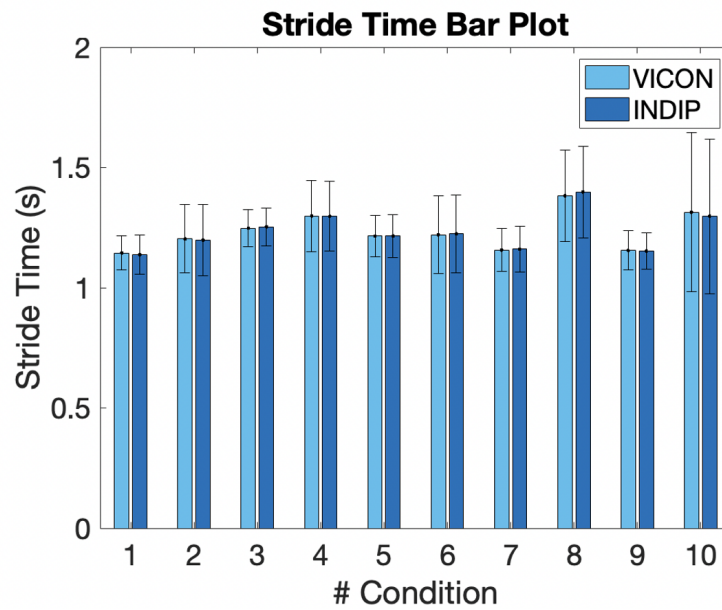


Figure 6.32: Barplot for comparing mean and standard deviation values for ST obtained with both systems.

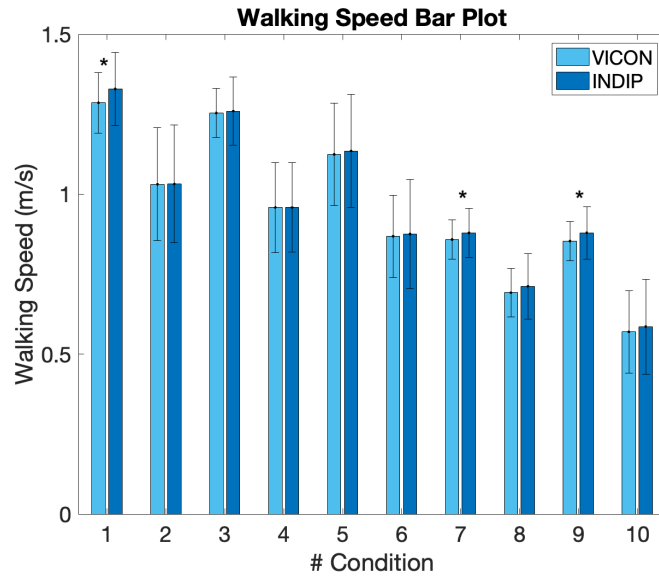


Figure 6.33: Barplot for comparing mean and standard deviation values for WS obtained with both systems.

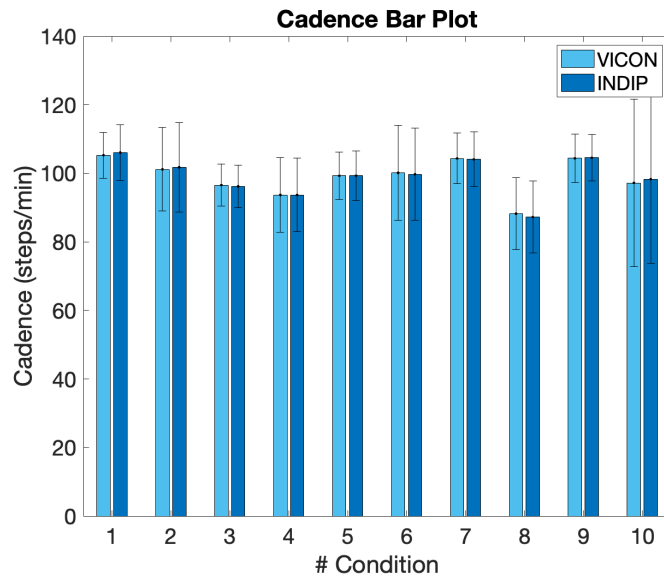


Figure 6.34: Barplot for comparing mean and standard deviation values for Cadence obtained with both systems.

Chapter 7

Discussion

The discussion chapter provides a comprehensive analysis and interpretation of the obtained results from the study evaluating the performance of the INDIP system in estimating gait parameters using both the original and modified algorithms. This section aims to delve into the implications and significance of the findings, comparing them with existing literature and shedding light on the strengths and limitations of the system. To begin the discussion, an analysis based on the identified events is conducted to evaluate the enhancement of the new optimized system in automatic event identification. This analysis examines the accuracy and reliability of the system in detecting key gait events, such as heel strike and toe-off, comparing the performance of the original and modified algorithms. The implications of improved event identification for subsequent parameter estimation are discussed, emphasizing the potential benefits of the modified algorithm in enhancing the overall accuracy of the INDIP system. Subsequently, the discussion shifts towards the results of spatiotemporal parameters obtained using the modified algorithm. The findings are analyzed and compared with existing literature to assess the system's performance and determine its effectiveness in accurately estimating these spatiotemporal parameters. By comparing the obtained results with previous research findings, the discussion highlights the system's advancements, potential applications, and areas that require further investigation or refinement. Ultimately, this comprehensive analysis and interpretation of the results contribute to a deeper understanding of the INDIP system's capabilities and limitations in estimating gait parameters, supporting its potential use in clinical and research settings. It is worth noting that out of the initial 10 subjects, only data from 6 subjects were processed. This reduction in the sample size was due to protocol changes, a recording error by the INDIP system, and a subject's withdrawal from the experiment for personal reasons.

7.1 Event Identification Analysis

In this section, the results presented in the previous chapter will be discussed. As observed, the results for gait events were analyzed separately for each terrain condition. Consequently, the discussion of the results will be organized accordingly. The Bland-Altman plots provide valuable insights into the mean differences and dispersion of the values. Therefore, comments on these images will be made, along with quantitative descriptions related to the tables presenting the mean differences and mean absolute differences.

For this part, the focus will be on examining the performance of the original algorithm compared to the optimized algorithm. The observed trends, improvements, and limitations in each terrain condition will be explored. Furthermore, the impact of the modifications on key metrics such as mean differences, mean absolute differences, and standard deviations will be discussed. By considering both the visual representation of the Bland-Altman plots and the numerical data presented in the tables, a comprehensive analysis can be provided.

7.1.1 Plane Terrain at 0°

This is the most frequently observed scenario in gait studies, where the ground is flat and there is no inclination. The INDIP algorithm has previously been validated for this specific terrain [6]. The results obtained from the original code, presented in the first column, demonstrate an acceptable range along the y-axis for temporal differences between systems. This range spans from a minimum of -0.1 seconds to a maximum of 0.1 seconds, with only a few outliers belonging to the third subject falls beyond this range. Notably, in the FC identification, there is a few number of events near or outside the acceptable range for subjects 5 and 8. This occurrence may be attributed to insufficient quality control measures before conducting the tests. Upon examining the second column, it becomes apparent that the modified algorithm does not significantly alter the results obtained from the original algorithm. This outcome can be attributed to the already acceptable level of error in the algorithm, indicating its effective functioning. However, there is a slight reduction in the range difference, and it is also noticeable that the overestimation of FC events for subject 8 has been mitigated, but now the negative range of the FC events has been increased. The mean difference between events is in zero so with the optimization of the algorithm results are more close to the ones obtained with the Vicon system. This observation is also evident in Table 6.1, where a significant reduction in errors is not observed. However, the most noticeable reduction is observed in the case of subject 8, which aligns with the previous discussion regarding the FC events.

7.1.2 Plane Terrain at 15°

This scenario also exemplifies a case where the algorithm performs well, and the errors are not significant enough to warrant concern. Figures 6.4, 6.5, and 6.6 illustrate that there is no substantial reduction in time differences between systems before and after the code modification. This observation is further supported by the data presented in Table 6.2.

7.1.3 Mat Terrain at 0°

This is the first instance where the algorithm begins to exhibit failures. The terrain in question is a mat, and it is reasonable to assume that the pressure will vary along the path. Table 6.3 reveals that NaN values are present for Subject 8. This occurs because the original algorithm failed to correctly identify all the events, resulting in a mismatch with the events recorded by the Vicon System. Consequently, no time difference can be computed. Additionally, Figures 6.7, 6.8, and 6.9 clearly depict the significant time differences between events, not showing the upper positive range in the plot and also exhibiting a high dispersion. This pattern is further reflected in Table 6.3, which displays the highest difference for Subject 3.

After implementing the modified algorithm, the range of time differences is not only reduced but also the dispersion of events, notably for the fifth subject. Furthermore, events performed by Subject 8 are now properly identified for comparison with the Vicon system, a feat that was initially unattainable.

7.1.4 Mat Terrain at 15°

Upon examining Figure 6.10, it can be observed that the maximum range has been reduced from approximately 0.16 seconds to 0.08 seconds. However, in this case, the minimum value of the range has slightly increased. Figure 6.12 indicates that this reduction is due to an underestimation of the FC, where the minimum range value has changed from 0.05 to approximately 0.09 in the original code. Nonetheless, it is positive to note that the mean difference, represented by the red line, is now centered around 0. This indicates that the range is more balanced, and most of the values obtained with the modified algorithm have a lower difference compared to the SP system. Table 6.4 reveals that while the reduction of differences is not very noticeable for subjects 3, 5, or 9, the differences have been roughly halved for subjects 4, 6, 7, and 8.

7.1.5 Unstructured Terrain at 0°

In Figure 6.13, for the unstructured terrain at 0°, it is evident that the range of time differences is quite wide, reaching a maximum value of almost 0.2 seconds.

Notably, there are numerous yellow dots representing outliers, for subject 8. Examining Figure 6.15, it becomes clear that this increase and presence of outliers are primarily due to FC events. However, with the optimized algorithm, the maximum difference is reduced to 0.1 seconds, and the outliers for subject 8 are corrected. Conversely, the outliers for subject 5 in blue either remain unchanged or may have increased slightly. Returning to Figure 6.13, the results obtained with the modified algorithm demonstrate a maximum difference below 0.1 seconds. Although the minimum difference has increased, it remains within the acceptable range of 0.1 seconds for accuracy. Moreover, the mean difference with the modified algorithm is approximately 0, as observed in Table 6.5. Subject 8, in the original code, exhibited a relative MD of -2.28% and a relative MAD of 2.65%, both of which were reduced to 1.43% with the modified code. Additionally, the standard deviation of the mean difference decreased from 0.1 to 0.5, indicating more consistent data. It is worth noting that for subject 7, although the differences were reduced, the standard deviation of these differences slightly increased with the optimized code. Another noteworthy observation is the sign of the mean differences in the original code, where there was an underestimation of values, leading to negative values for this metric in most cases. However, this issue is resolved in the modified code for the majority of cases.

7.1.6 Unstructured Terrain at 15°

In a similar manner to the previous case, the time differences between the INDIP and VICON systems using the original INDIP code exhibited a wide range of up to approximately 0.2, with some outliers, particularly for subject 8. However, these issues were resolved in the optimized algorithm. In Figure 6.16, the range of time differences is significantly reduced, which can be attributed to the enhancement of the PI signals and the modification of the criteria for selecting possible IC values. The same improvement is observed in Figure 6.18 for FC instants. These enhancements are further supported by the data presented in Table 6.6. For instance, the relative MAD for subject 8 was reduced from almost 6% to 3%.

7.1.7 Upward Sawtooth at 0°

This represents another scenario where the original algorithm fails to identify the same number of events as the SP system for subject 8. Moreover, as illustrated in Figure 6.19, subject 5 poses a problem as all the data points are widely scattered, resulting in a significant range of time differences. This issue is observed not only for the FC (Figure 6.20) but also for the IC, as evident in Figures 6.20 and 6.27. In Figure 6.20(B), it is noticeable that the error with subject 5 is consistently reduced, leading to a meaningful improvement. This improvement is also reflected in Table

6.7, where subject 8 is marked with a NaN value, indicating the impossibility of calculating the respective values for this subject. Additionally, subject 5 exhibits the highest MAD with a value of 25%, which is reduced to 7% after applying the modified algorithm. Another noteworthy observation is the reduction in the standard deviation of the differences, with most cases experiencing a decrease. For instance, subject 5, which initially had a variability of the error around 0.82, sees it reduced to 0.36. In general, most of the values are reduced after applying the modified algorithm. However, it is worth noting that subject 7 shows a slight increase in terms of MD and MAD.

7.1.8 Upward Sawtooth at 15°

The original code encountered a significant problem in this case, as evident in Figure 6.22, where the range of time differences spans from -0.6 to approximately 0.8, which are not indicated in the plot. The presence of numerous outliers indicates a specific issue with subject 5, as all the blue data points are widely scattered. This problem affected both IC and FC, as depicted in Figures 6.24 and 6.24. Table 6.8 provides further insights, revealing a relative MAD of approximately 25%, indicating an extreme case of error. However, with the optimized algorithm, this error is mitigated, reducing the relative MAD to 13.25%. Additionally, it is worth noting that SD of MD is close to 1, suggesting heterogeneity in the errors. This indicates that there may have been issues during data acquisition, which have been partially addressed by the more robust algorithm.

7.1.9 Downward Sawtooth at 0°

In this particular case, the original code initially performed well, with a range of time differences between systems, reaching around 0.15, as shown in Figure 6.25. This slight excess can be attributed to a problem in the identification of FC, as evident in Figure 6.27. With the optimized algorithm and the applied methods, the overestimation of FC values is reduced, with a maximum difference of approximately 0.8 seconds. Besides, it has also been a reduction on the maximum negative value of the range of differences, being now smaller than 0.1 seconds. On the other hand, the differences in IC instants, depicted in Figure 6.26, are highly reduced, likely due to the application of the sigmoid function that enhances the valleys.

7.1.10 Downward Sawtooth at 15°

In this case, the original algorithm performs worse compared to the previous case, resulting in a high range of time differences being close to 0.2. Moreover, the

minimum value of the range is more negative than the acceptable limit of -0.1, as shown in Figure 6.28. Notably, in Figures 6.29 and 6.30, it can be observed that this significant difference occurs in both event results. However, with the modified code, the range of time differences is reduced to fall within the acceptable value of 0.1, but maintaining the performance related to the negative value of the range. It is important to mention that subject 5 still exhibits outliers that persist in the optimized algorithm. This aspect is also evident in Table 6.10, where the row for subject 5 indicates a slight increase in the relative MAD with the optimized code. For the remaining cases, the MAD is not significantly reduced, suggesting that the optimization methods may be less robust in these instances.

7.2 Spatio-temporal Parameters Analysis

The gait parameters studied are:

- Stride Length (m)
- Stride Time (secs)
- Walking Speed (m/sec)
- Cadence (steps/min)

Upon examining the bar plots presented in Figures 6.31, 6.32, 6.33, and 6.33, it is evident that the results obtained from both the VICON and INDIP systems regarding the spatio-temporal parameters are remarkably similar between all cases. The mean and standard deviation of both parameters exhibit close resemblance in all conditions. However, it is worth noting that there is a slightly higher variation in the INDIP results observed in the stride length among all conditions, which can be attributed to the integration techniques involved in the calculation of spatial parameters. In Figure 6.31 and 6.33 some asterisks can be seen, these indicates the conditions that present statistical significant difference, calculated with the T-Test. For the stride length, there is statistical significant differences for:

- Condition 1: Overground Terrain at 0°.
- Condition 15: Upward Sawtooth Terrain at 0°.
- Condition 16: Upward Sawtooth Terrain at 15°.
- Condition 17: Upward Sawtooth Terrain at 0°.

The Walking Speed presents statistical significant differences in all the same conditions except for the 16.

Table 6.11 provides an overview of the parameter values along with the corresponding metrics, which were defined in Chapter 5. These calculations were performed for all subjects, categorized based on the different terrain conditions. A similar validation procedure was followed in the study "A multi-sensor wearable system for the assessment of diseased gait in real-world conditions," which also utilized these metrics.

In that study, the INDIP system demonstrated good performance compared to the SP system, with maximum errors for Stride Length of 1.22% (relative ME), 0.92% (relative MDE), an IQRE up to 16%, a maximum relative MAE of 10%, a maximum relative MDAE of 6%, and ICC values ranging from 0.92 to 0.98. These results were obtained for overground conditions, and they are consistent with the findings of the present study. Specifically, our study yielded a relative ME of 1.58%, an MDE of approximately 1.52%, an IQRE with a maximum of 6.15%, an MAE of around 4%, an MDAE also around 4%, and ICC values as low as 0.8, indicating some discrepancies between the two systems.

As anticipated, similar terrain conditions exhibited comparable parameter values for stride length. However, in the case of inclined terrain, the relative ME and MDE were slightly lower. This is likely due to the smaller number of steps taken on inclined surfaces compared to overground conditions. The relative IQRE, MAE, and MDAE were slightly higher for inclined terrain.

Regarding the other types of terrains, the ME ranges from 0.12% to 4.04%, with the latter being the only one higher than 3%. This indicates that there are some variations depending on each type of terrain, but overall, the range of errors is quite low, which makes the estimations acceptable. Additionally, the MDE ranges between 0.03% and 2.78% for the different types of terrains. Furthermore, the MDAE values consistently remain lower than the MAE values.

For unstructured terrain at 0° and 15°, the system also performed well, demonstrating similar parameter values as previously mentioned. In the case of unstructured terrain at 0°, the ICC was lower than that of 15°, which can be attributed to the larger number of steps taken in the first condition. In the soft terrain where the mat is placed results are similar to the previous case, but now the ICC is slightly higher for the 15° of inclination. The higher error is observed in the Sawtooth Upward condition at 15°, with a relative percentual mean error of 4%, IQRE of 13%, and an ICC of 0.15. These results indicate that this scenario represents the worst case for the INDIP, where it performs poorly. The elevated IQRE value is also observed in the Downward condition at 15°. This could be attributed to the increased slope, as it introduces not only a 15° terrain inclination but also a 15° inclination of the modules relative to the platform. This situation poses challenges in defining the dynamic reference system for each stride.

Furthermore, it is important to note that in this type of sawtooth terrains, the majority of error values are higher compared to other types of terrains, not only at 15° but also at 0° . This may be due to the minimal 15° inclination of each module and the distribution of pressure during each step. During the experiments, it was observed that the difficult terrain conditions caused subjects to walk differently. Some subjects only placed their foot at the extreme end of the module without fully placing the entire foot on it, while others only placed their heel or toe down. These variations in walking patterns contribute to the worst-case scenario.

The comparison of stride time with the previous study mentioned [6] cannot be directly made because the parameters were not calculated, and the duration is based on a walking bout defined as a sequence of at least two strides. However, in terms of stride time, a much better absolute agreement can be observed, with an ICC of 0.97. The higher relative mean error is approximately 1.20%, which is remarkably low, corresponding to a time difference of only 0.02 seconds. Moreover, the mean values and standard deviations are similar, differing only by a few hundredths. These findings suggest that the INDIP system is more accurate in calculating temporal parameters compared to spatial parameters. This difference can be easily understood as spatial parameters are indirectly derived through integration processes of acceleration and velocity signals, whereas temporal parameters are directly calculated using the time measured by the sensors, estimated through the collected samples.

In the previous study [6], the higher mean error related to the duration of certain gait phases was approximately 3%. In contrast, in the current study, the higher error is about 1.2%, which is extremely acceptable considering the results obtained with the INDIP system. This particular value is obtained for the Sawtooth Upward terrain at 15° , and the standard deviation of these values is very similar for both the INDIP and SP systems, indicating that the time variability of the walk for different subjects was captured by both systems.

In the mentioned article, the relative ME and MDE for walking speed ranged from 0.3% to 1.57% and 0.37% to a maximum of 1.24%, respectively, with reliable data values (ICC>0.93). The MAE had a maximum of 11.21%, while the MDAE ranged between 3.20% and 7.10%. For cadence, the maximum ME was 0.92% and 0.37%, with MAE ranging between 3.45% and 6.28%, and MDAE with a maximum of 2.75% and a minimum of 1.37%. The minimum ICC was approximately 0.73, indicating a significant amount of variability or inconsistency between the measurements, and a maximum IQRE of 6.28% was observed. In the current project, the maximum ME for walking speed was 3% in the Sawtooth Downward at 0° . The MDE values were lower than the ME, with a maximum of 2.89%, but a negative value of -0.49% was observed for the overground condition. The ICC values were generally reliable for some terrains, but in the worst case, it did not exceed 0.34, with an IQRE of approximately 15.35%, indicating a lack of precision and accuracy in the estimation

or measurement process. As usual, the MDAE values were slightly lower than the MAE, ranging between 3.5% and 8.15% for the former, while the latter varied between 4% and 9.91%. In terms of cadence, the variability observed by both the SP and INDIP systems is quite similar. There are some ME values close to 0, but there are also negative errors, with the lowest being -1% for the Sawtooth Upward at 15° condition. The MDE values are mostly around 0%, indicating minimal deviation from the true values, while the MDAE ranges from 0% to 3%. The highest MAE value recorded is 4.16%, and the maximum IQRE is approximately 7%. In terms of reliability, the ICC values are generally high, with only 2 cases falling below 0.90.

Chapter 8

Conclusions

The primary aim of this thesis was to optimize and validate the algorithm of a multi-sensor system known as INDIP, which incorporates IMUs, PI, and DS. This system was modified to accurately characterize human gait in extreme terrain conditions. Analyzing gait in such terrains provides valuable reference data that can be utilized in the development of robotic systems aimed at replacing or assisting human locomotion.

This study marks the first instance where a multi-sensor system has been employed to gather information on gait across various complex terrains. The experiments conducted in this project were not only unique but also introduced novel methods for enhancing the performance of the system. The implementation of these methods had not been previously explored, further contributing to the innovative nature of this research. After a comprehensive analysis of the results, it can be concluded that the INDIP system performs effectively in overground conditions, consistent with previous studies cited throughout the thesis. It demonstrates minimal time differences between identified events and exhibits accurate parameter calculations when compared to the SP system. However, when applied to different terrain conditions characterized by irregular pressure distribution and diverse inertial signals, the system's performance is affected, particularly in relation to the signals from pressure insoles. The quality of these signals is compromised, resulting in suboptimal outcomes.

To address these challenges, modifications and additional methods were incorporated into the INDIP system's algorithm. These enhancements aimed to create a more robust version capable of handling variations in pressure distribution, which proved to be a critical factor in these non-standard terrain conditions. The evaluation of results obtained with the original algorithm, combined with an assessment of signal quality, guided the development of this improved version.

Comparing the outcomes of the SP system and the modified INDIP system, a notable reduction in time differences for event identification and a decrease in

errors concerning gait parameters were observed in most cases. Consequently, a robust system that can accurately characterize gait in extreme terrain conditions was achieved.

In terms of limitations encountered during the progress of this thesis, it should be noted that the number of subjects included in the study was ultimately lower than initially anticipated. Furthermore, not all the PI were properly calibrated before the experiments, resulting in increased time difference errors between events. Another limitation pertains to the reduced length of the platform used for the studies. Particularly, when the platform was set at a 15° incline, the length was halved compared to the standard length at 0° , consequently reducing the number of steps available for analysis. The smaller sample size limited the statistical power and may impact the generalizability of the results to a larger population. Additionally, the presence of uncalibrated PI could have introduced inaccuracies in the event identification process. Moreover, the reduced length of the platform, especially at an incline, limited the number of steps that could be analyzed, potentially affecting the overall assessment of gait performance.

Future developments can offer several avenues for exploration. Firstly, expanding the study to include a larger and more diverse sample size would enhance the generalizability of the findings and provide a more comprehensive understanding of gait performance in this type of terrains. Incorporating advanced calibration techniques for PI and exploring alternative sensor technologies or combining multiple sensor modalities would improve accuracy and robustness. Additionally, future developments should include an emphasis on exploring a wider range of extreme terrains, not only simulated but also in real world environments. This could involve studying gait in environments with challenging surfaces such as rocky terrains, slippery surfaces, or even extreme weather conditions. This broader exploration would deepen our understanding of how gait is affected by different environmental factors, allowing the development of algorithms and control strategies that enable robots to navigate and traverse similar environments. Finally, the development of real-time analysis and feedback methods would enable immediate adjustments and interventions to optimize gait performance. By addressing these areas of future development, researchers can advance the field of gait analysis in extreme terrains, refine assistive technologies, and improve outcomes in various challenging scenarios.

In conclusion, the INDIP system demonstrates its efficacy in overground conditions and successfully addresses the challenges posed by different extreme terrains through algorithmic modifications. By significantly reducing time differences and improving parameter accuracy, it offers a reliable and practical solution for gait analysis in such conditions. Further research and development may continue to refine the system and explore its potential applications in various challenging scenarios.

Bibliography

- [1] David Pinto-Fernandez, Diego Torricelli, Maria del Carmen Sanchez-Villamanan, Felix Aller, Katja Mombaur, Roberto Conti, Nicola Vitiello, Juan C Moreno, and Jose Luis Pons. «Performance evaluation of lower limb exoskeletons: a systematic review». In: *IEEE Transactions on Neural Systems and Rehabilitation Engineering* 28.7 (2020), pp. 1573–1583 (cit. on p. 2).
- [2] Stephanie Blair, Mark J Lake, Rui Ding, and Thorsten Sterzing. «Magnitude and variability of gait characteristics when walking on an irregular surface at different speeds». In: *Human movement science* 59 (2018), pp. 112–120 (cit. on p. 2).
- [3] Satoru Shirasaka, Tamotsu Machida, Hiroshi Igarashi, Satoshi Suzuki, and Masayoshi Kakikura. «Leg Selectable Interface for Walking Robots on Irregular Terrain». In: *2006 SICE-ICASE International Joint Conference*. IEEE. 2006, pp. 4780–4785 (cit. on p. 2).
- [4] Justin Carpentier and Pierre-Brice Wieber. «Recent Progress in Legged Robots Locomotion Control». In: *Current Robotics Reports* 2.3 (Sept. 2021), pp. 231–238 (cit. on p. 2).
- [5] Hongchao Zhuang, Haibo Gao, Zongquan Deng, Liang Ding, and Zhen Liu. «A review of heavy-duty legged robots». In: *Science China Technological Sciences* 57.2 (Feb. 2014), pp. 298–314 (cit. on p. 2).
- [6] Francesca Salis et al. «A multi-sensor wearable system for the assessment of diseased gait in real-world conditions». In: *Frontiers in Bioengineering and Biotechnology* 11 (2023). ISSN: 2296-4185. DOI: 10.3389/fbioe.2023.1143248. URL: <https://www.frontiersin.org/articles/10.3389/fbioe.2023.1143248> (cit. on pp. 3, 4, 7, 15, 22, 27, 41, 88, 94).
- [7] Teddy Caderby, Eric Yiou, Nicolas Peyrot, Mickaël Begon, and Georges Dalleau. «Influence of gait speed on the control of mediolateral dynamic stability during gait initiation». In: *Journal of Biomechanics* 47.2 (2014), pp. 417–423. ISSN: 0021-9290. DOI: <https://doi.org/10.1016/j.jbiomech.2013.11.011>. URL: <https://www.sciencedirect.com/science/article/pii/S0021929013005630> (cit. on p. 3).

- [8] Roxanne Larsen and Daniel Schmitt. «Maintaining Stability on Uneven Terrain: Gait Analysis During Outdoor Running». In: *Medicine Science in Sports Exercise* 46 (June 2014), p. 816. DOI: 10.1249/01.mss.0000495946.34736.50 (cit. on p. 3).
- [9] Rachel Horenstein, Cara Lewis, Sherry Yan, Anne Halverstadt, and Sandra Shefelbine. «Validation of Magneto-Inertial Measuring Units for Measuring Hip Joint Angles». In: *Journal of Biomechanics* 91 (May 2019). DOI: 10.1016/j.jbiomech.2019.05.029 (cit. on pp. 3, 16).
- [10] Paul M. Riek, Aaron N. Best, and Amy R. Wu. «Validation of Inertial Sensors to Evaluate Gait Stability». In: *Sensors* 23.3 (2023). ISSN: 1424-8220. URL: <https://www.mdpi.com/1424-8220/23/3/1547> (cit. on p. 3).
- [11] Alvaro Muro-De-La-Herran, Begonya Garcia-Zapirain, and Amaia Mendez-Zorrilla. «Gait analysis methods: An overview of wearable and non-wearable systems, highlighting clinical applications». In: *Sensors* 14.2 (2014), pp. 3362–3394 (cit. on p. 3).
- [12] Fabio Suim Chagas, Luis David Peregrino de Farias, Matheus Bozza, and Paulo Fernando Ferreira Rosa. «A tenacity learning algorithm for humanoid robot locomotion based on the human gait cycle». In: *2020 IEEE 29th International Symposium on Industrial Electronics (ISIE)*. 2020, pp. 519–524. DOI: 10.1109/ISIE45063.2020.9152516 (cit. on pp. 5, 6).
- [13] Md Akhtaruzzaman, A.A. Shafie, and Md Raisuddin Khan. «GAIT ANALYSIS: SYSTEMS, TECHNOLOGIES, AND IMPORTANCE». In: *Journal of Mechanics in Medicine and Biology* 16 (Mar. 2016), p. 1630003. DOI: 10.1142/S0219519416300039 (cit. on p. 5).
- [14] Richard Baker, Alberto Esquenazi, Maria G Benedetti, and Kaat Desloovere. «Gait analysis: clinical facts». In: *European journal of physical and rehabilitation medicine* 52.4 (Aug. 2016), pp. 560–574. ISSN: 1973-9087. URL: <http://europepmc.org/abstract/MED/27618499> (cit. on p. 5).
- [15] Anselmo Frizzera, Arlindo Elias, Antonio J. del-Ama, Ramon Ceres, and Teodiano Freire Bastos. «Characterization of spatio-temporal parameters of human gait assisted by a robotic walker». In: *2012 4th IEEE RAS EMBS International Conference on Biomedical Robotics and Biomechatronics (BioRob)*. 2012, pp. 1087–1091. DOI: 10.1109/BioRob.2012.6290264 (cit. on p. 6).
- [16] Hylton B. Menz, Stephen R. Lord, and Richard C. Fitzpatrick. «Acceleration patterns of the head and pelvis when walking on level and irregular surfaces». In: *Gait Posture* 18.1 (2003), pp. 35–46. ISSN: 0966-6362. DOI: [https://doi.org/10.1016/S0966-6362\(02\)00159-5](https://doi.org/10.1016/S0966-6362(02)00159-5). URL: <https://www.sciencedirect.com/science/article/pii/S0966636202001595> (cit. on p. 6).

- [17] Stephanie Blair, Mark J. Lake, Rui Ding, and Thorsten Sterzing. «Magnitude and variability of gait characteristics when walking on an irregular surface at different speeds». In: *Human Movement Science* 59 (2018), pp. 112–120. ISSN: 0167-9457. DOI: <https://doi.org/10.1016/j.humov.2018.04.003>. URL: <https://www.sciencedirect.com/science/article/pii/S0167945717305407> (cit. on p. 7).
- [18] Alexandra S. Voloshina, Arthur D. Kuo, Monica A. Daley, and Daniel P. Ferris. «Biomechanics and energetics of walking on uneven terrain». In: *Journal of Experimental Biology* 216.21 (Nov. 2013), pp. 3963–3970. ISSN: 0022-0949. DOI: 10.1242/jeb.081711. eprint: <https://journals.biologists.com/jeb/article-pdf/216/21/3963/1879354/3963.pdf>. URL: <https://doi.org/10.1242/jeb.081711> (cit. on p. 7).
- [19] Andrew Merryweather, Byungju Yoo, and Donald Bloswick. «Gait Characteristics Associated with Trip-Induced Falls on Level and Sloped Irregular Surfaces». In: *Minerals* 1.1 (2011), pp. 109–121. ISSN: 2075-163X. URL: <https://www.mdpi.com/2075-163X/1/1/109> (cit. on p. 7).
- [20] Harald Böhm, Matthias Hösl, Hermann Schwameder, and Leonhard Döderlein. «Stiff-knee gait in cerebral palsy: How do patients adapt to uneven ground?» In: *Gait Posture* 39.4 (2014), pp. 1028–1033. ISSN: 0966-6362. DOI: <https://doi.org/10.1016/j.gaitpost.2014.01.001>. URL: <https://www.sciencedirect.com/science/article/pii/S0966636214000034> (cit. on p. 7).
- [21] Nils Eckardt and Noah J. Rosenblatt. «Healthy aging does not impair lower extremity motor flexibility while walking across an uneven surface». In: *Human Movement Science* 62 (2018), pp. 67–80. ISSN: 0167-9457. DOI: <https://doi.org/10.1016/j.humov.2018.09.008>. URL: <https://www.sciencedirect.com/science/article/pii/S0167945718302161> (cit. on p. 7).
- [22] Hylton B. Menz, Stephen R. Lord, and Richard C. Fitzpatrick. «Acceleration patterns of the head and pelvis when walking on level and irregular surfaces». In: *Gait Posture* 18.1 (2003), pp. 35–46. ISSN: 0966-6362. DOI: [https://doi.org/10.1016/S0966-6362\(02\)00159-5](https://doi.org/10.1016/S0966-6362(02)00159-5). URL: <https://www.sciencedirect.com/science/article/pii/S0966636202001595> (cit. on p. 7).
- [23] Alberto Ferrari, Pieter Ginis, Michael Hardegger, Filippo Casamassima, Laura Rocchi, and Lorenzo Chiari. «A Mobile Kalman-Filter Based Solution for the Real-Time Estimation of Spatio-Temporal Gait Parameters». In: *IEEE Transactions on Neural Systems and Rehabilitation Engineering* 24.7 (2016), pp. 764–773. DOI: 10.1109/TNSRE.2015.2457511 (cit. on p. 7).

- [24] Rosa M.S. Visscher, Sailee Sansgiri, Marie Freslier, Jaap Harlaar, Reinald Brunner, William R. Taylor, and Navrag B. Singh. «Towards validation and standardization of automatic gait event identification algorithms for use in paediatric pathological populations». In: *Gait Posture* 86 (2021), pp. 64–69. ISSN: 0966-6362. DOI: <https://doi.org/10.1016/j.gaitpost.2021.02.031>. URL: <https://www.sciencedirect.com/science/article/pii/S0966636221000813> (cit. on p. 7).
- [25] Hongyin Lau and Kaiyu Tong. «The reliability of using accelerometer and gyroscope for gait event identification on persons with dropped foot». In: *Gait Posture* 27.2 (2008), pp. 248–257. ISSN: 0966-6362. DOI: <https://doi.org/10.1016/j.gaitpost.2007.03.018>. URL: <https://www.sciencedirect.com/science/article/pii/S0966636207001142> (cit. on p. 7).
- [26] G. Cappellini, Y. P. Ivanenko, R. E. Poppele, and F. Lacquaniti. «Motor Patterns in Human Walking and Running». In: *Journal of Neurophysiology* 95.6 (2006). PMID: 16554517, pp. 3426–3437. DOI: 10.1152/jn.00081.2006. eprint: <https://doi.org/10.1152/jn.00081.2006> (cit. on p. 8).
- [27] M. Nordin and V.H. Frankel. *Basic Biomechanics of the Musculoskeletal System*. Lippincott Williams & Wilkins, 2001. ISBN: 9780683302479. URL: <https://books.google.es/books?id=UCxsf7mMBE0C> (cit. on pp. 8–11).
- [28] Marco Knafitz, Andrea Cereatti, Dott Ing Marco Caruso, and Rachele Rossanigo. «Analysis of spatial parameters during gait with magneto-inertial sensors and infrared proximity sensors». In: (2019) (cit. on pp. 11, 12).
- [29] Abhinandan Aggarwal, Rohit Gupta, and Ravinder Agarwal. «Design and Development of Integrated Insole System for Gait Analysis». In: Aug. 2018, pp. 1–5. DOI: 10.1109/IC3.2018.8530543 (cit. on p. 12).
- [30] Claudiane Arakaki Fukuchi, Reginaldo Kisho Fukuchi, and Marcos Duarte. «Effects of walking speed on gait biomechanics in healthy participants: a systematic review and meta-analysis». In: *Systematic Reviews* 8.1 (June 2019), p. 153 (cit. on p. 12).
- [31] Gutemberg Guerra Filho. «Optical Motion Capture: Theory and Implementation.» In: *RITA* 12 (Jan. 2005), pp. 61–90 (cit. on pp. 13, 14).
- [32] Pedro Alves Nogueira. «Motion Capture Fundamentals A Critical and Comparative Analysis on Real-World Applications». In: (2012) (cit. on p. 14).
- [33] Yonatan Hutabarat, Dai Owaki, and Mitsuhiro Hayashibe. «Recent Advances in Quantitative Gait Analysis Using Wearable Sensors: A Review». In: *IEEE Sensors Journal* 21.23 (2021), pp. 26470–26487. DOI: 10.1109/JSEN.2021.3119658 (cit. on p. 16).

- [34] Matilde Bertoli et al. «Estimation of spatio-temporal parameters of gait from magneto-inertial measurement units: Multicenter validation among Parkinson, mildly cognitively impaired and healthy older adults». In: *BioMedical Engineering OnLine* 17 (May 2018). DOI: 10.1186/s12938-018-0488-2 (cit. on p. 16).
- [35] Kang Rao, Wei Xiaoli, Shaolin Zhang, Mengqi Zhang, Chenyuan Hu, Huafeng Liu, and Liang-Cheng Tu. «micromachines A MEMS Micro-g Capacitive Accelerometer Based on Through-Silicon-Wafer-Etching Process». In: *Micro-machines* 10 (June 2019), p. 380. DOI: 10.3390/mi10060380 (cit. on pp. 17, 18).
- [36] Waqas Amin Gill, Ian Howard, Ilyas Mazhar, and Kristoffer McKee. «A Review of MEMS Vibrating Gyroscopes and Their Reliability Issues in Harsh Environments». In: *Sensors* 22.19 (2022). ISSN: 1424-8220. DOI: 10.3390/s22197405. URL: <https://www.mdpi.com/1424-8220/22/19/7405> (cit. on pp. 18–20).
- [37] X. Tian, J. Li, Y. Fan, J. Liu, and W. Chen. «A calibration-compensation method for micro inertial measurement unit». In: *Chinese Journal of Sensors and Actuators* 25 (Jan. 2012), pp. 1411–1415. DOI: 10.3969/j.issn.1004-1699.2012.010.017 (cit. on p. 20).
- [38] Elena Martini, Tommaso Fiumalbi, Filippo Dell’Agnello, Zoran Ivanić, Marko Munih, Nicola Vitiello, and Simona Crea. «Pressure-Sensitive Insoles for Real-Time Gait-Related Applications». In: *Sensors* 20 (Mar. 2020), p. 1448. DOI: 10.3390/s20051448 (cit. on p. 21).
- [39] Simona Crea, Marco Donati, Stefano Marco Maria De Rossi, Calogero Maria Oddo, and Nicola Vitiello. «A Wireless Flexible Sensorized Insole for Gait Analysis». In: *Sensors* 14.1 (2014), pp. 1073–1093. ISSN: 1424-8220. DOI: 10.3390/s140101073. URL: <https://www.mdpi.com/1424-8220/14/1/1073> (cit. on p. 21).
- [40] Simona Crea, Christian Cipriani, Marco Donati, Maria Chiara Carrozza, and Nicola Vitiello. «Providing Time-Discrete Gait Information by Wearable Feedback Apparatus for Lower-Limb Amputees: Usability and Functional Validation». In: *IEEE Transactions on Neural Systems and Rehabilitation Engineering* 23.2 (2015), pp. 250–257. DOI: 10.1109/TNSRE.2014.2365548 (cit. on p. 21).
- [41] Abdul Razak, Aladin Zayegh, Rezaul Begg, and Yufridin Wahab. «Foot Plantar Pressure Measurement System: A Review». In: *Sensors (Basel, Switzerland)* 12 (Dec. 2012), pp. 9884–912. DOI: 10.3390/s120709884 (cit. on p. 21).

- [42] Fahni Haris, Ben-Yi Liao, Yih-Kuen Jan, Veit Babak Hamun Akbari, Yanuar Primanda, Kuan-Han Lin, and Chi-Wen Lung. «A Review of the Plantar Pressure Distribution Effects from Insole Materials and at Different Walking Speeds». In: *Applied Sciences* 11.24 (2021). ISSN: 2076-3417. DOI: 10.3390/app112411851. URL: <https://www.mdpi.com/2076-3417/11/24/11851> (cit. on p. 21).
- [43] F. Salis, S. Bertuletti, T. Bonci, U. Della Croce, C. Mazzà, and A. Cereatti. «A method for gait events detection based on low spatial resolution pressure insoles data». In: *Journal of Biomechanics* 127 (2021), p. 110687. ISSN: 0021-9290. DOI: <https://doi.org/10.1016/j.jbiomech.2021.110687>. URL: <https://www.sciencedirect.com/science/article/pii/S0021929021004565> (cit. on p. 21).
- [44] A.M. Kassim, Hazriq Izzuan Jaafar, Mohd Asyadi Azam, Nabil Abas, and T. Yasuno. «Performances study of distance measurement sensor with different object materials and properties». In: Aug. 2013, pp. 281–284. ISBN: 978-1-4799-1028-1. DOI: 10.1109/ICSEngT.2013.6650185 (cit. on pp. 22, 23).
- [45] Nathaniel Goldfarb, Alek Lewis, Alex Tacescu, and Gregory S. Fischer. «Open source Vicon Toolkit for motion capture and Gait Analysis». In: *Computer Methods and Programs in Biomedicine* 212 (2021), p. 106414. ISSN: 0169-2607. DOI: <https://doi.org/10.1016/j.cmpb.2021.106414>. URL: <https://www.sciencedirect.com/science/article/pii/S0169260721004880> (cit. on p. 24).
- [46] VICON. «ACTIVE WAND USER GUIDE». In: (2011-2021), pp. 1–10 (cit. on p. 24).
- [47] Anthony Remazeilles et al. «Making Bipedal Robot Experiments Reproducible and Comparable: The Eurobench Software Approach». In: *Frontiers in Robotics and AI* 9 (2022). ISSN: 2296-9144. DOI: 10.3389/frobt.2022.951663. URL: <https://www.frontiersin.org/articles/10.3389/frobt.2022.951663> (cit. on p. 38).
- [48] Zhaoqin Peng, Chun Cao, Jiaoying Huang, and Wentao Pan. «Human Moving Pattern Recognition toward Channel Number Reduction Based on Multi-pressure Sensor Network». In: *International Journal of Distributed Sensor Networks* 2013 (Nov. 2013), pp. 1–10. DOI: 10.1155/2013/510917 (cit. on p. 48).
- [49] Matthew Sadiku, Sarhan Musa, Sudarshan Nelatury, and Roy Perry. «Correlation: A Brief Introduction». In: *International Journal of Electrical Engineering Education* 51 (Apr. 2014), p. 33. DOI: 10.7227/IJEEE.51.2.1 (cit. on p. 50).

- [50] Yi Hu, Philipos C. Loizou, Ning Li, and Kalyan Kasturi. «Use of a sigmoidal-shaped function for noise attenuation in cochlear implants». In: *The Journal of the Acoustical Society of America* 122.4 (Sept. 2007), EL128–EL134. ISSN: 0001-4966. DOI: 10.1121/1.2772401. eprint: https://pubs.aip.org/asa/jasa/article-pdf/122/4/EL128/15283658/e1128\1_online.pdf. URL: <https://doi.org/10.1121/1.2772401> (cit. on p. 50).
- [51] Shinichi Tamura and Alexander H. Waibel. «Noise reduction using connectionist models». In: *ICASSP-88., International Conference on Acoustics, Speech, and Signal Processing* (1988), 553–556 vol.1 (cit. on p. 50).
- [52] Grzegorz Szwoch. «Suppression of distortions in signals received from Doppler sensor for vehicle speed measurement». In: *2018 Signal Processing: Algorithms, Architectures, Arrangements, and Applications (SPA)*. 2018, pp. 16–21. DOI: 10.23919/SPA.2018.8563403 (cit. on p. 51).